Fall 12-17-2016

An Ionization Chamber for High Resolution Fission Product Spectroscopy

James Cole

James Cole
Candidate

Nuclear Engineering
Department

This thesis is approved, and it is acceptable in quality and form for publication:

Approved by the Thesis Committee:

Adam Hecht, Chairperson

Gary Cooper

Cassiano Ricardo Endres de Oliveira

An Ionization Chamber for High Resolution Fission Product Spectroscopy

By

James Cole

Bachelor of Science – Nuclear Engineering 2014

University of New Mexico

THESIS

Submitted in Partial Fulfillment of the Requirements for the Degree of

Master of Science

Nuclear Engineering

The University of New Mexico

Albuquerque, New Mexico

December 2016

Acknowledgements

I would first like to thank my family and friends for their continual support in all areas of my life. I could not have made it through without their love and determination to help me succeed. In addition, I would like to thank my graduate advisor Dr. Adam Hecht for the opportunity to work on this project and the guidance given throughout my studies. I would also like to thank my committee members Dr. Cassiano Ricardo Endres de Oliveira and Dr. Gary Cooper, both who have taught me valuable information over my academic career.

Individually, I want to give my deepest thanks to my research partner Rick Blakeley. Rick not only taught me volumes of information about this project but is also a dear friend who helped to create a great work and educational environment. I value his input on both the research work we did together and other life lessons learned along the way. In addition, I would like to thank Ken Carpenter for his help in detector and electronic troubleshooting. Many issues encountered would not have been overcome without his help. I would also like to thank my lab partners Lena Heffern, Shelby Fellows, and Phoenix Baldez for their contributions made to the project. Finally, I would like to thank all the members of the SPIDER group at the LANCSE facility at Los Alamos National Labs for their help and guidance in this research.

An Ionization Chamber for High Resolution Fission Product Spectroscopy

By

James Cole

B.S., Nuclear Engineering, University of New Mexico, 2014

M.S., Nuclear Engineering, University of New Mexico, 2016

Abstract

The fission process has played a vital role in the world's search for effective sources of alternative energy. With almost 80 years of work with fissionable material there is still much that is unknown about the process. Fission fragment mass and atomic number distributions are still lacking in completeness and critical detail. Knowledge of this information is highly sought after in the effort to improve various fields of nuclear physics and engineering such as reactor design, predictive models, waste disposal methods, and an overall understanding of the fission process.

In an effort to better understand this process, we have developed and tested a fission fragment spectrometer in collaboration with the Spectrometer for Ion Detection in Fission Research project (SPIDER) at Los Alamos National Laboratory. The fission fragment spectrometer uses a time-of-flight (TOF) technique to measure the particle's velocity and an ionization chamber to measure the particle's kinetic energy. From these two values the particle's mass can be determined. The UNM spectrometer has implemented an ionization chamber with an active cathode configuration that allows the ionization chamber to act as a time projection chamber. This full set-up allows for coincident measurements of the particle's velocity and energy to obtain mass, and range to obtain atomic charge information. Several other techniques and experiments have been developed to measure fission fragment mass and atomic charge distributions, however they exhibit varying resolution and efficiency limitations. The goal of this project is to develop a high efficiency, low-resolution spectrometer to obtain an overall mass resolution of less than

one atomic mass unit (amu) and to show that the atomic charge of the particle can be determined.

Table of Contents

List of Figures

List of Tables

1 Introduction/Purpose of Study

1.1 Introduction

The nuclear fission process was discovered by Hahn and Strassmann in December of 1938 [Wagemans 1991]. With almost 80 years of research and successful implementation of fission applications there are still many questions surrounding the details of fission. More recent modeling methods have provided a good foundation for predicting mass yields but these models are guided by past data causing a need for improved experimental data. This data would lead to a better overall understanding of the physical process of fission in addition to improved simulation calculations, reactor theory, safety, design, and waste management procedures.

Nuclear fission is understood to mean a process where a heavy nucleus decays into two large fragments [Wagemans 1991]. Thermal neutron-induced fission is when a neutron of energies ranging from 0.025 eV to 1 eV, causes asymmetric fission of heavy nuclei. During this process two fragments of a range of mass and number of neutrons are emitted. Taking ^{235}U, for example, this process results in one fragment having a mass near 90 amu and the other near 140 amu. This difference in splitting is a function of incident neutron energy and preformation conditions within the nucleus. Figure 1 is a good representation of asymmetric fission.

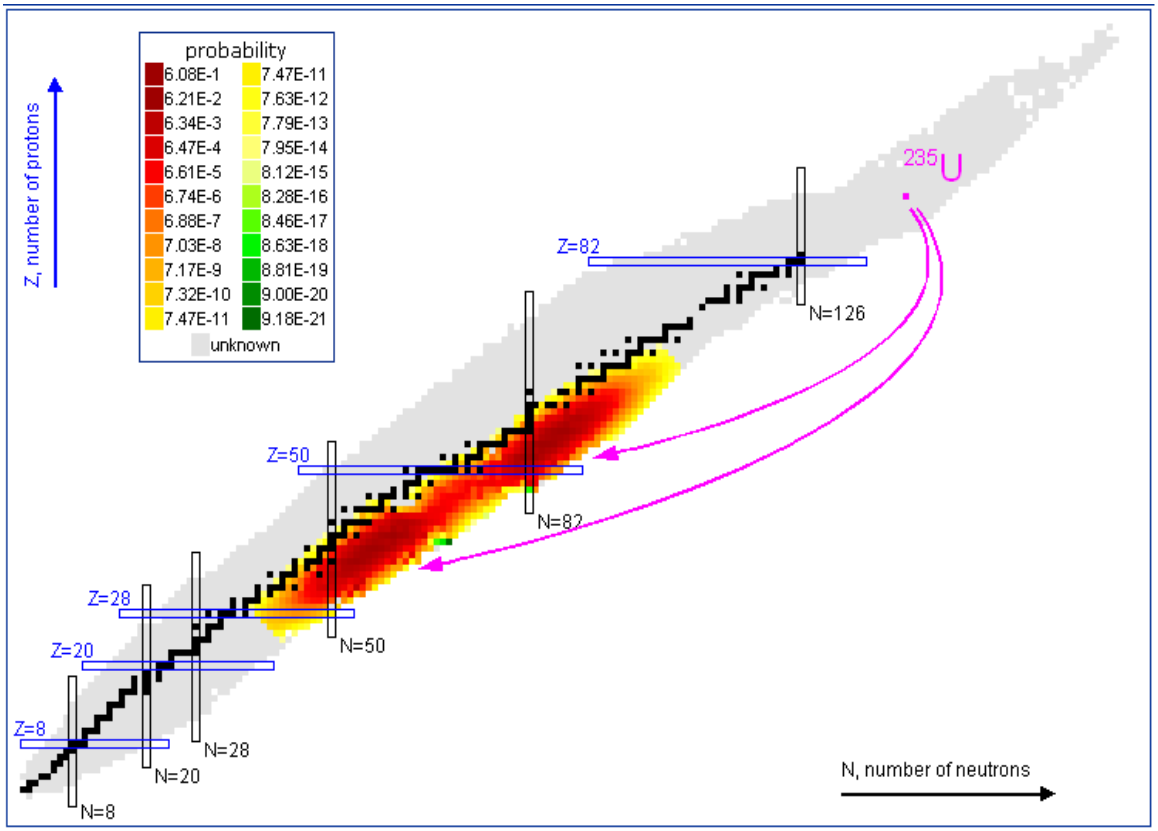

Figure 1– Asymmetric fission of ^{235}U [Magee 2011]

This figure shows the probability of isotope production that results from the thermal fission of ^{235}U. There appears to be a group of nuclides that dominate this fission process. Another important detail in the detection of fission products is the pre- and post-neutron emission masses. As heavy nuclei fission the products promptly emit neutrons and gammas, along with subsequent gammas from the immediate beta decay. This prompt time scale is much faster than what we are capable of measuring and, therefore, we are concerned with the post neutron emission values that can be obtained on a microsecond scale. An example in the difference between pre- and post-neutron emission masses can be found in Table 1.

Table 1 – ^{252}Cf pre- and post-neutron emission average energy and mass for both heavy (h) and light (l) fragments [Schmitt 1965]

^{252}Cf spontaneous fission		
Quantity	Pre-neutron	Post-neutron
E_l (MeV)	106.2	103.77
E_h (MeV)	80.3	79.37
m_l (amu)	108.55	106
m_h (amu)	143.45	141.9

These values are obtained for the average light and heavy fragment released during the spontaneous fission of ^{252}Cf; where E_l is the light fragment energy, E_h is the heavy fragment energy, m_l is the light fragment mass, and m_h is the heavy fragment mass.

In order to contribute to this industry-wide need for improved fission fragment data, a fission fragment mass spectrometer has been developed at the University of New Mexico (UNM) with the overall goal of producing a high-efficiency, high-resolution detector capable of obtaining a mass resolution of < 1 amu and atomic charge (Z) information. This apparatus is an event-by-event detector that is capable of measuring both the fragment's time-of-flight (TOF) and energy deposition yielding the mass of the fragment. This type of measurement is based on a velocity-energy (v-E) design [Boucheneb, 1989] that will be discussed more in Section 1.3 on previous work. In addition, an ionization chamber designed with an active cathode allows for range and thus atomic number determination of the particle. A simple schematic of the v-E spectrometer is presented in Figure 2.

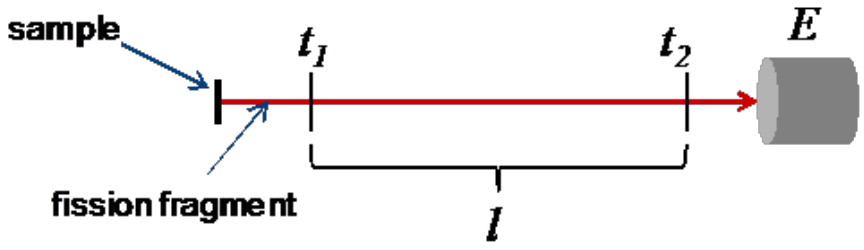

Figure 2 – 1V-1E Mass Spectrometer with TOF and E detector regions.

The incident radiation can be either a spontaneous fission source or a fissionable target exposed to a neutron beam. For either case, the fission products emitted may travel down the chamber encountering conversion foils. The products pass through and eject electrons from the foils, which have very little effect on the trajectory of the fission products. Then these freed electrons are directed to the timing detectors via electrostatic mirrors. The time of flight is measured by the difference in the pulses induced on the timing detectors by the ejected electrons from each conversion foil. Typically, the timing detectors are multichannel plates (MCP) due to their high timing resolution. By knowing the distance between these detectors, the velocity can be obtained from the TOF by the equation

$$v = \frac{l}{\Delta t}$$

After the particle has passed both of the timing detectors, it enters the energy detector where a pulse height measurement is taken. It is then possible to calculate the mass of the incident particle by classical physics using

$$M = 2\frac{E}{v^2} = 2\frac{E}{\left[\frac{l}{\Delta t}\right]^2}$$

This spectrometer has been successfully tested at the Los Alamos Neutron Science Center (LANSCE) at the Lujan Center at Los Alamos National Laboratory (LANL). In collaboration with the SPIDER (Spectrometer for Ion DEtermination in Fission Research) group at LANL, mass measurements have been made for the thermal fission of ^{235}U. At the University of New Mexico, ^{252}Cf data has been taken.

1.2 Previous Work on Mass Spectrometers

Many previous experiments have been done to measure fission fragment energy, masses, and atomic charge using a variety of different methods by different groups. The bulk of the current nuclear data comes from yields obtained using chemical separation methods. These methods are reliable yet do not give a real time account of the fragments at the time of fission. This method does have a high efficiency but there are large uncertainties associated with the measurements. This uncertainty and a desire for real time measurements led to other methods being explored.

One method uses the Lohengrin mass spectrometer which employs electric and magnetic deflection fields to separate fission products of varying mass (A), kinetic energy (E), and charge (Q) [Rochman 2002]. Particles are separated by the ratio of (A/Q) by magnetic fields and (p/Q) by electric fields, which then determine E/Q, with field strengths tuned to examine to the nuclides of interest. This method results in an energy resolution of 0.2% [Rochman 2002]. Figure 3 shows the multiple atomic charges that make up a single mass and energy selection.

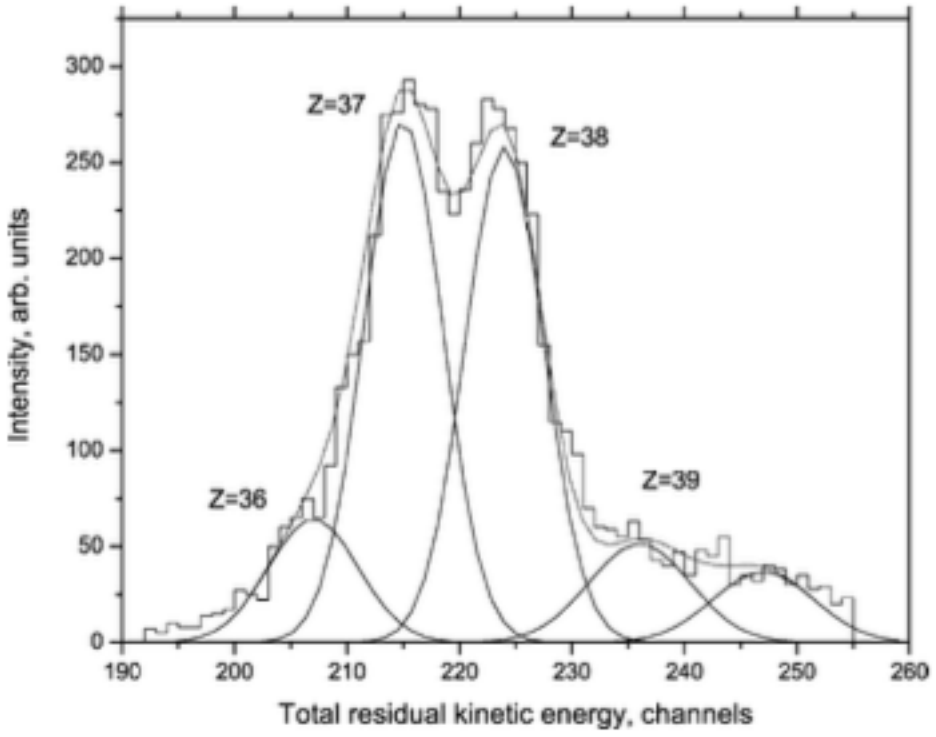

Figure 3 – Kinetic energy distribution for A= 93 and E = 102 MeV from Lohengren where the residual kinetic energy is defined as (ΔE-E) of the fission fragment. E is the incident fragment energy and ΔE is the amount of energy measured in an solid energy absorber [Rochman 2002]

Figure 3 shows that there is a distinguishable contribution from multiple elements that contribute to the overall kinetic energy spectrum. A high-resolution detector, such as the Lohengrin spectrometer, is necessary to see this type of detail for a given distribution. If energy resolution becomes too broad, the Gaussians that make up each atomic charge distribution will begin to overlap and the data cannot be properly interpreted. Despite the extremely high resolution obtained by this method, it requires a large magnet to produce the desired field and has a low efficiency due to its ability to obtain only one mass depending on the conditions set for the fields.

A different method explored by Oed *et al.* utilizes start and stop timing multichannel plates (MCP) for a time-of-flight (TOF) measurement - from which velocity is extracted - and an ionization chamber for energy. The combination of these two coincident measurements is known as the velocity-energy (v-E) method. In this experiment the High Flux Reactor at the Langevin Institute was used to irradiate a ^{235}U target that was 100 $\mu g/cm^2$ thick and 10 mm in diameter [Oed 1983]. A spectrum of ^{235}U data from that work is shown in Figure 4.

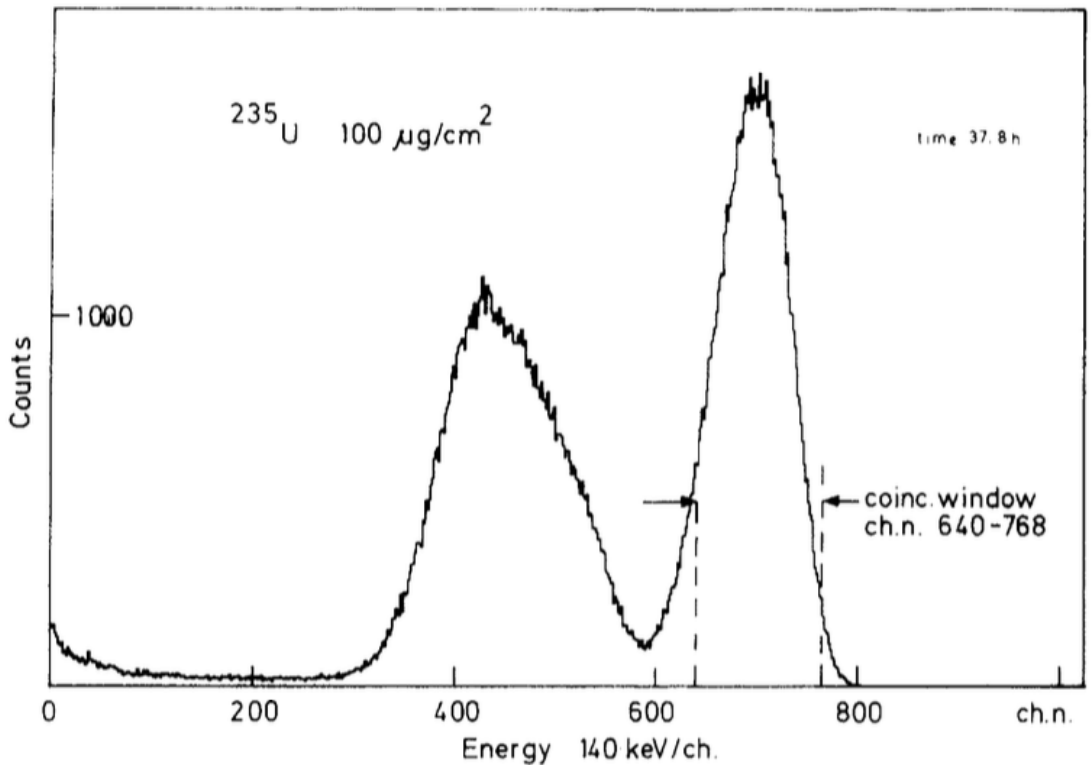

Figure 4 – ^{235}U Energy Spectrum using Langevin High Flux Reactor [Oed 1983]

Figure 4 shows an average light and heavy peak corresponding to approximately 98 MeV and 59.5 MeV respectively. It should be noted that the heavy peak is much wider than the light peak. This is a common attribute of the energy spectrum caused by straggling of the heavy charged particles which is more significant than that of the light particles. This effect will be discussed in more detail in the theory section.

Boucheneb *et al.* also implemented the v-E method with the Cosi Fan Tutte spectrometer. This work was performed using a 106.7 µg/cm^2 $^{229}ThO_2$ in a TOF-ionization chamber set up installed at the Grenoble high flux reactor [Boucheneb 1989]. Again using the measured time-of-flight from the start and stop detectors and energy reading from the

ionization chamber the mass can be calculated. Figure 5 shows a high-resolution mass distribution obtained from this work.

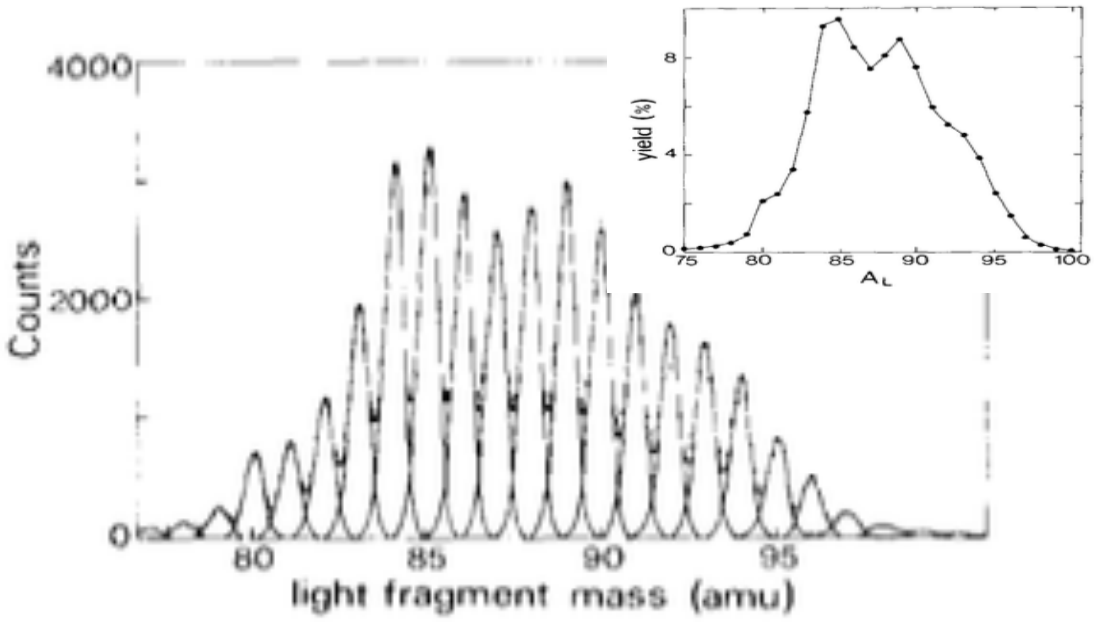

Figure 5 – High-resolution mass distribution with Gaussian fits of 0.64amu resolution from experimental data (top right) [Boucheneb 1989]

The v-E method is limited by the efficiency of particles entering the ionization chamber. This limitation is affected by the source strength, distance from source, the window material, and window thickness. However, it is believed that this method provides the greatest balance between resolution and efficiency and has, therefore, it is the method we have adopted for the work presented in this paper.

Schmitt *et al.* also focused on using the v-E method, to obtain mass spectra for both ^{235}U and ^{252}Cf. ^{252}Cf is a spontaneous fission source, and the material used had an activity of $3x10^5$ fissions per minute [Schmitt 1965]. The ^{235}U was deposited onto a carbon foil by the vacuum evaporation process of $^{235}UF_4$. The neutron beam at Oak Ridge Research

Reactor was used to induce fission on the ^{235}U target. *n*-type silicon surface barrier detectors were used to obtain energy readings of the incoming particles. Figure 6 gives mass spectra of ^{235}U and ^{252}Cf obtained from this work.

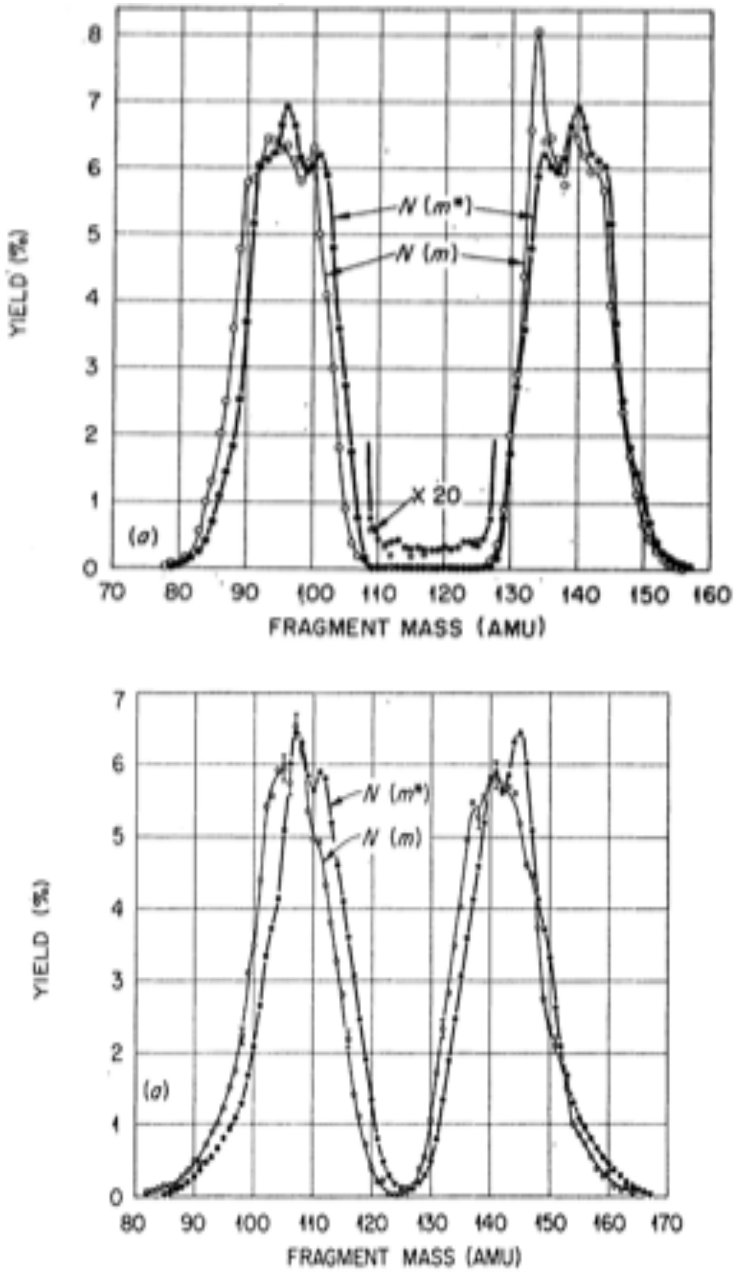

Figure 6 – Mass Spectra of ^{235}U (top) and ^{252}Cf (bottom) [Schmitt 1965]

It was determined that the average light and heavy fragments masses were 106 and 141.9 amu for ^{235}U and 96.57 and 139.43 amu for ^{252}Cf. These values are used as calibration parameters that will be discussed in the methodology section of this paper.

1.3 Previous work on Z Determination

In addition to the measurement of fission fragment energy and mass, atomic charge measurements have also been made. Sanami *et al*. created a detector they describe as a Bragg curve counter (BCC) [Sanami 2006]. A Bragg curve counter is a gas filled detector that measures the Bragg peak height and full Bragg curve in the gas caused by the incident radiation. The Bragg peak height is fairly constant for different energies of the same nuclides, compared with the full Bragg curve area that is due to nuclide energy. Figure 7 shows SRIM simulated Bragg curves for alpha particles having three different energies, demonstrating this phenomenon.

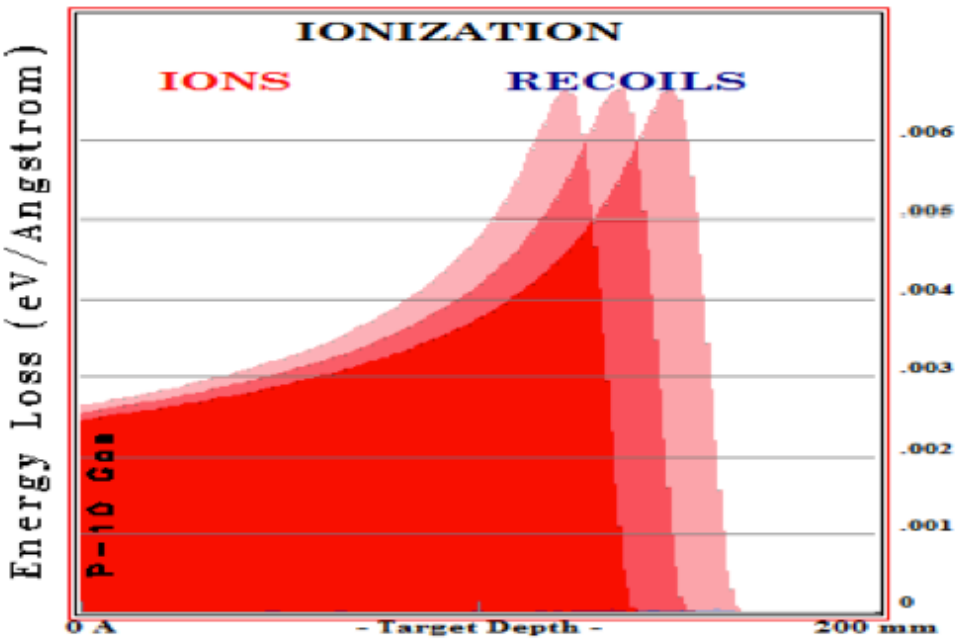

Figure 7 – Bragg curve for alpha particle with different energies

Bragg curve spectroscopy is comprised of two different measurements: the amount of ionization caused by the incident particle which gives the kinetic energy and the amplitude of the peak which gives atomic charge information. These two readings are obtained by splitting the output signal into two amplification electronics setups with different integration times [Vega 2005]. Bragg curve spectroscopy will be discussed more in the theory section. The Sanami BCC is a cylindrical ionization chamber with the cathode and anode at either end. The construction of the ionization chamber consists of a doughnut shaped cathode with an entrance window into the chamber from the TOF region, field shaping rings to maintain a uniform electric field, a Frisch grid, and an anode. The uniform electric field allows for the electrons created by the ionizing radiation to travel at

a constant velocity. By using the timing stamps from the electrode signals the shape of the ionization in the gas can be reconstructed.

That BCC was tested using a 70 MeV proton beam incident on a polypropylene sample at the AVF Cyclotron facility of National Institute of Radiological Science at Tohoku University, Japan [Sanami 2006]. Figure 8 shows the separation in the Bragg curve pulse height for the ions emitted from the carbon sample.

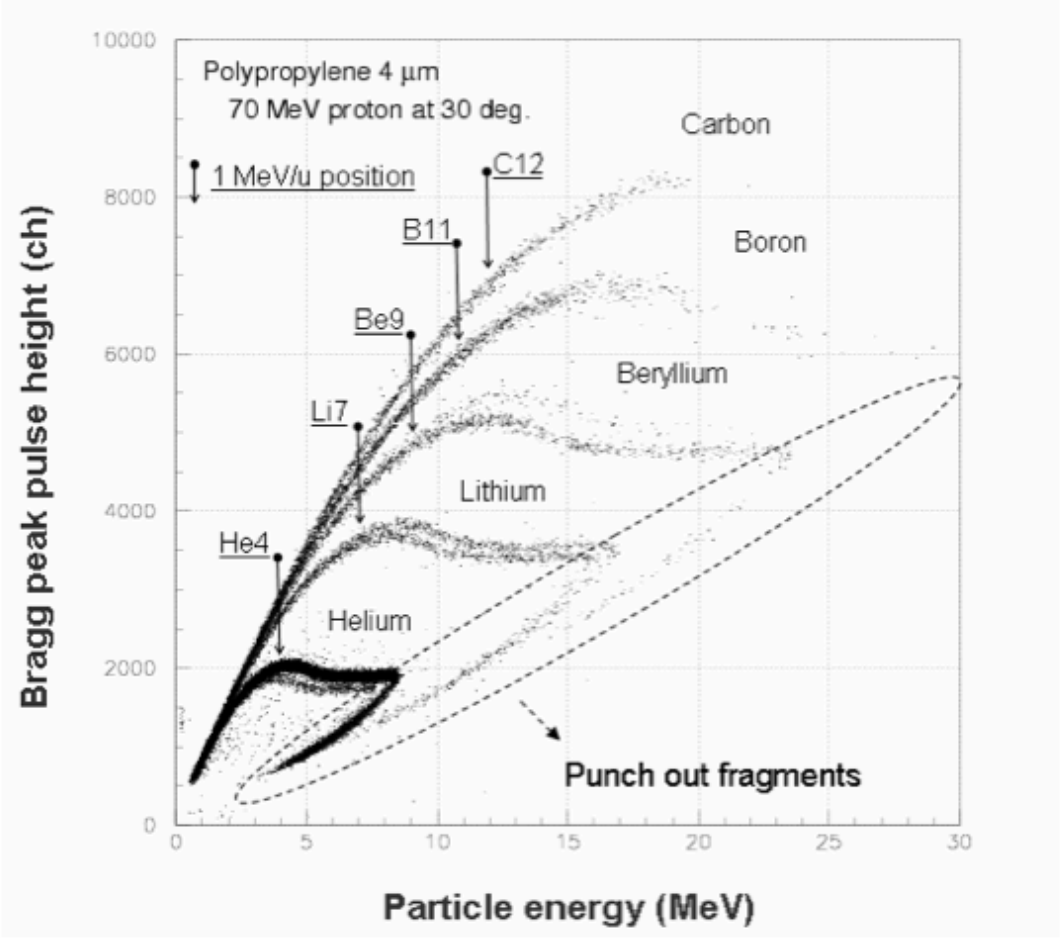

Figure 8 – Bragg peak pulse height for polypropylene sample [Sanami 2006]

This figure shows that the Bragg peak occurs at different energies for each individual element. This response is due to the charge interaction specific to each isotope. A common issue with Bragg curve spectroscopy is that it is only valid for heavy ions with energies of >1 MeV/amu, which is not the case for fission products [Tyukavkin 2008]. This limitation of Bragg curve spectroscopy motivated a need for a method more fitting for the detection of fission products.

Tyukavkin *et al*. developed a method utilizing range measurements of the fission products to extract Z information [Tyukavkin 2008]. To obtain the range that the particles travel into the ionization chamber, the drift time of the electrons from where they were liberated by the particle to the anode is considered. The range is equal to the physical length of the chamber from the cathode to the Frisch grid, minus the drift distance of the electrons from where they're created to the Frisch grid, extracted from the drift time of the electrons times the drift velocity of the electrons. This equation and methodology will be described more in the theory section. It is important to note that the key to this method is the measurement of the time in which it takes a product to deposit energy within the chamber. Figure 9 shows for example a simulated dependence of the mass specific drift velocity vs. the drift time of the electrons in the Tyukavkin experimental setup.

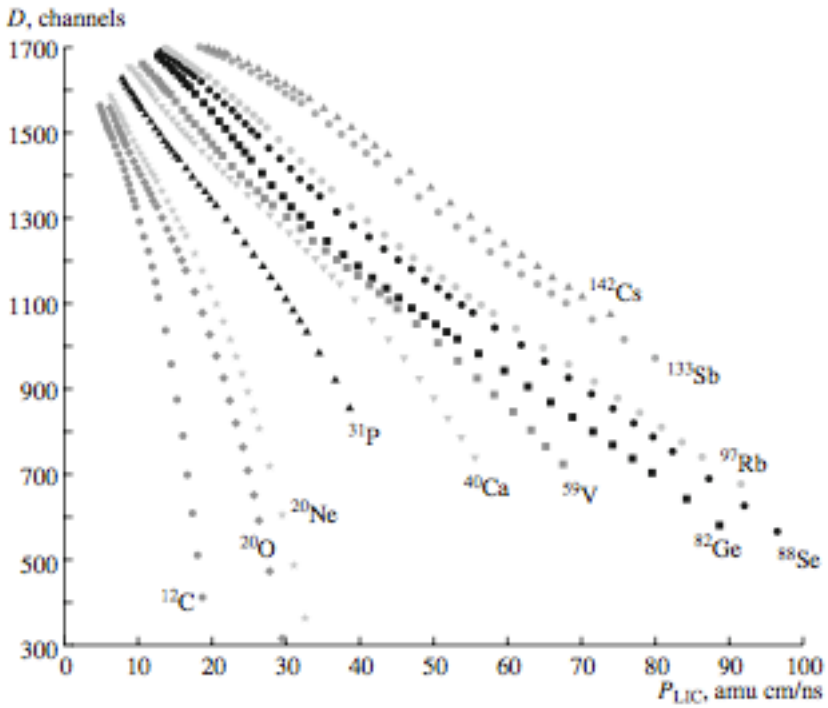

Figure 9 – Simulated mass dependent drift time (y-axis) and momentum (x-axis) [Tyukavkin 2008]

Figure 9 shows that there is a distinguishable difference in the time it takes a pulse to be induced on the cathode before it passes the Frisch grid for each element. This difference is what leads to the ability to determine the element being detected.

2 Ionization Chamber Theory and Applications

2.1 General Detector Configuration

A property shared by all gas detectors is the need to use an electric potential. These electrodes are used to create an electric field to collect the electrons created by the incoming radiation to register a signal. This collection of charge induces a current in the circuitry that can be converted into the signal that serves as the basis of our ionization chamber. The two main electrodes consist of a cathode, that acts to repel the electrons, and an anode, that acts as the collection surface. For our configuration of a parallel plate chamber the electric field is uniform and follows the equation

$$E = \frac{V_0}{d}$$

where V_0 is the voltage applied to the cathode and d is the distance between the two electrodes [Tsoulfanidis 2015]. Figure 10 gives a simple schematic of a parallel plate configuration.

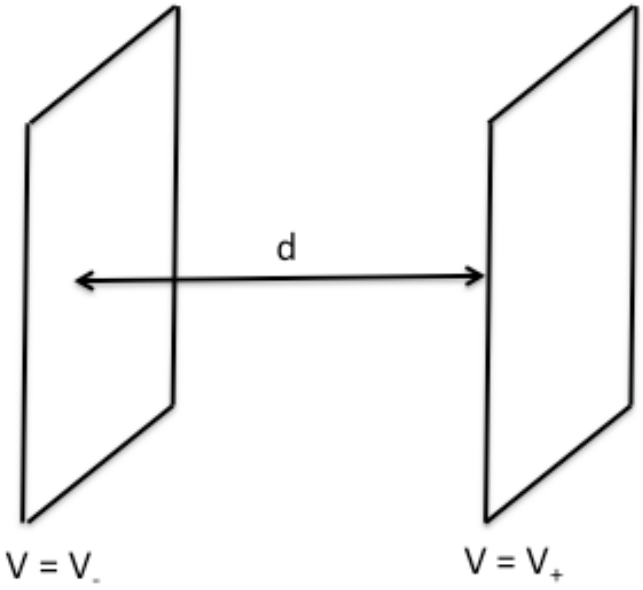

Figure 10 -- Parallel plate ionization chamber schematic.

The field created between these two electrodes is extremely important in the ability of the detector to be able to produce a signal. Electrons created close to the cathode have a longer distance to travel before the signal is created on the anode. This longer time of travel before the collection of electrons allows time for recombination to occur. Therefore, it is important to have a field strength great enough to move the electrons to the anode as rapidly as possible without creating a charge avalanche. This is prevented by a combination of the distance between the electrodes and the voltages applied to them.

2.2 Electron-Ion Pairs

The principle of ionization chambers is the simplest of all gas detectors based off the normal operation of collecting all charges created during the interaction of ionization

radiation with the gas within the chamber [Knoll 2010]. In typical practices ionization chambers detect ion pairs. Ion pairs are created when a neutral molecule is ionized resulting in a positive ion and a free electron. The motion of charges induces the observed pulse on the electrode. As the drift speed of gas ions is much, much slower than that of electrons, the free electrons create the electrical signal and serves as the means of detecting incident radiation. The number of ion pairs created is different based upon the type of fill gas used within the chamber and the incident energy of the incoming particle. Table 2 gives some *W*-values, or the average energy lost by the incident particle per ion pair formed [Knoll 2010], for some common fill gases. *W*-values are assumed to be constant for a given gas, which leads to a constant proportionality of the energy deposited by incident radiation and the number of e^--ion pairs created. This principle is key to the operation of an ionization chamber.

Table 2 – *W*-Values for common detector gases [Knoll 2010]

Gas	First Ionization Potential (eV)	*W*-Value (eV/ion pair)	
		Fast Electrons	Alpha Particles
Ar	15.7	26.4	26.3
He	24.5	41.3	42.7
H_2	15.6	36.5	36.4
N_2	15.5	34.8	36.4
Air		33.8	35.1
O_2	12.5	30.8	32.2
CH_4	14.5	27.3	29.1

2.3 Applied Voltage Operating Regions

Another factor that affects the proportionality of the pulses received by the detector is the voltage applied to the electrodes of the detector. Figure 11 shows the different operating regions for gas detectors.

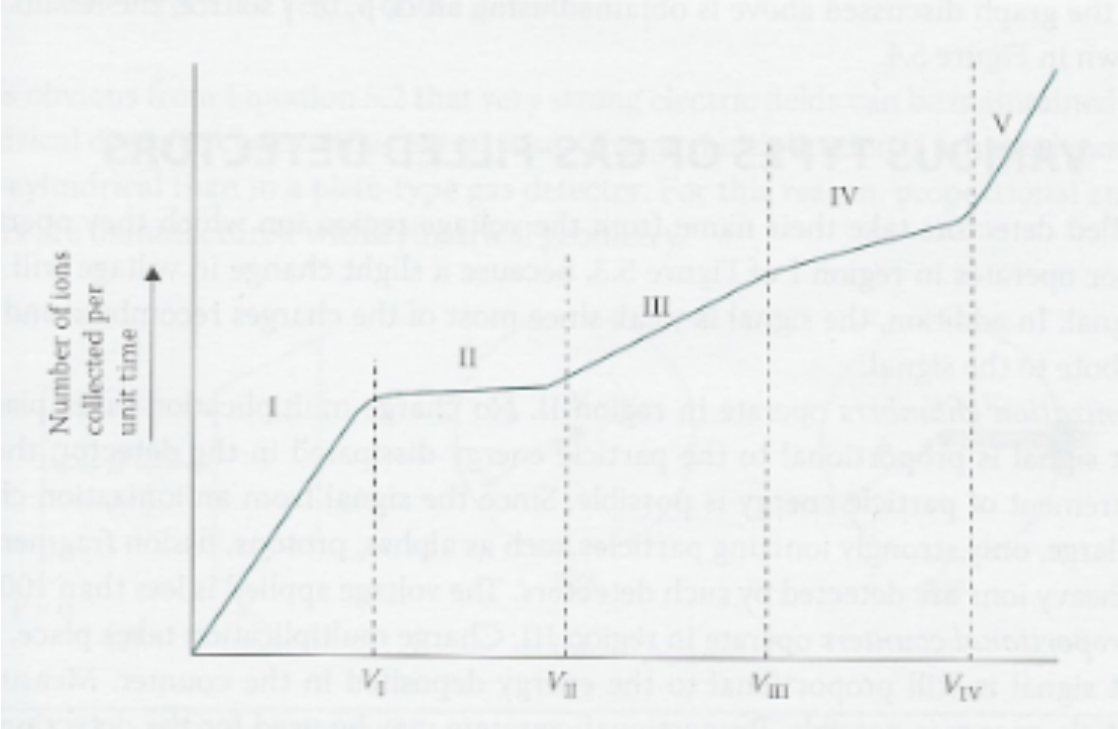

Figure 11 – Gas detector operation regions for applied voltage (x-axis) and number of ions collected per unit time (y-axis) [Tsoulfanidis 2015]

Ionization chambers operate in region II from Figure 11. This is known as the ionization region. In this range of electric field, the charge collected stays constant even if there is a small variation in applied voltage, no new charge is produced, and recombination is minimized [Tsoulfanidis 2015]. These properties are critical to the proper operation of an ionization chamber ensuring that the output signal is directly proportional to the energy deposited by the incident radiation.

2.4 Drift Velocity

Drift is the process of motion of charge carriers under the influence of an electric field [Aprile 2006]. As in the case of ionization chambers, electrons produced within the chamber are under the influence of an electric field, pushing them away from the cathode and towards the anode. Under these conditions the drift velocity, v_d, follows the equation below

$$\overrightarrow{v_d} = \frac{\mu\epsilon}{P}$$

where ε is the electric field strength, μ is the charge mobility, and P is the gas pressure [Knoll 2015]. Due to the difference in mobility the drift velocity obtained by a positive ion is negligible compared with the velocity obtained by electrons. The mobility μ remains constant for e^- over a wide range of voltages and pressures [Knoll 2015], so ion motion is ignored. The value ε/P is known as the reduced electric field and plays an important role in the drift velocity of electrons in gas. Figure 12 shows drift velocity curves for different gases as a function of ε/P. Figure 12 shows that different gasses affect the drift velocity significantly, which affects the pulses produced by the detector.

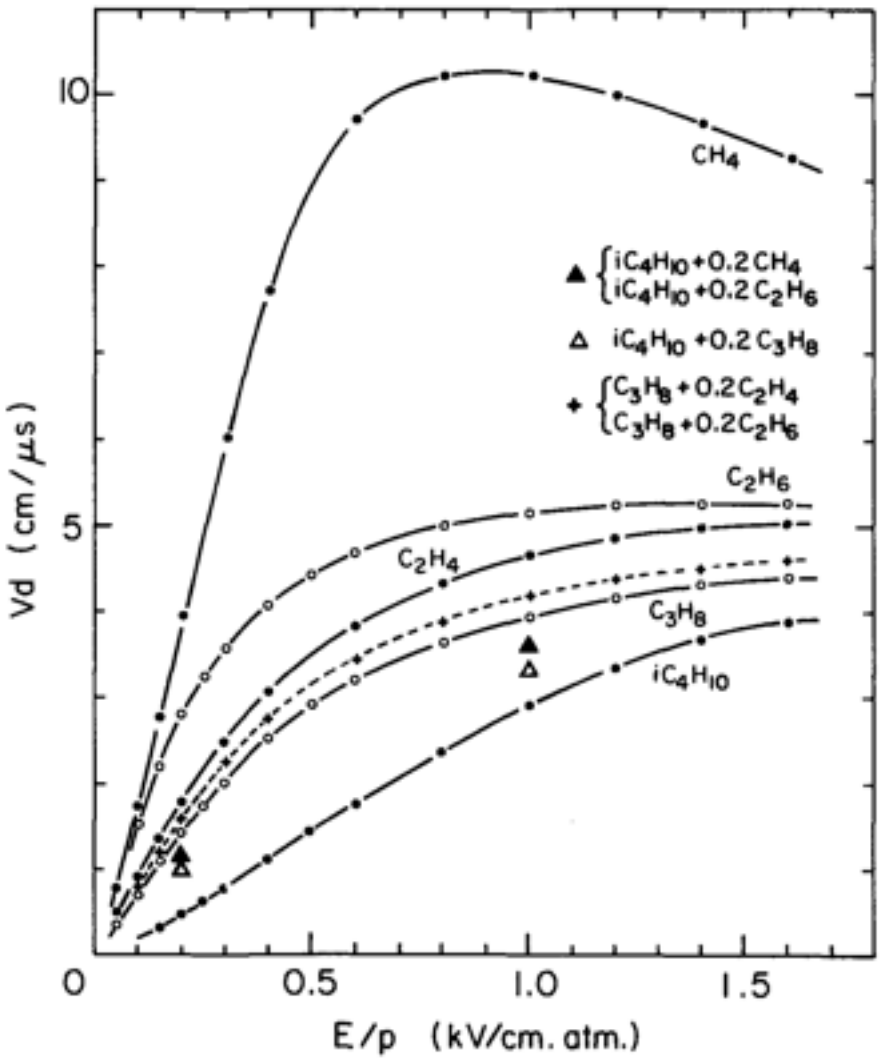

Figure 12 – Drift velocity for different gas mixtures of carbon and hydrogen [Peisert 1984]

2.5 Pulse Shape Derivation

The pulse shape produced from the drift of charged particles is well defined by the *Shockley-Ramo theorem* [Knoll 2010]. The theorem states that the pulse is not an instantaneous one, but is built up as the particles traverse the chamber. This leads to a smooth rise in the pulse until all the energy has been deposited, which then leads to a decay.

For the purpose of this experiment a parallel plate ion chamber is used and therefore the derivation of the pulse shape will be discussed only for this geometry.

A parallel plate ionization chamber can be thought of as a capacitor and a resistor, making it an RC circuit [Tsoulfanidis 2015]. A constant voltage is applied to each electrode, creating a constant electric field intensity over the length of the chamber. Under these conditions when an incoming charge particle enters the electric field it begins to gain energy and, by conservation of energy, therefore removes some energy from the capacitor. The conservation of energy equation is found below

$$eE(dx^+ + dx^-) = d\left(\frac{Q^2}{2C}\right) = \frac{Q}{C}dQ \approx V_0(dQ^- + dQ^+)$$

where E is the electric field intensity, Q is the charge on the chamber electrodes, and dQ represents the charge of the positive or negative ion. Again assuming that the applied voltage, V_0, stays constant despite the moving charges and that the drift velocity of the electrons and ions stays constant, the conservation of energy equation becomes

$$V(t) = \frac{e}{Cd}\int_0^t (w^+ + w^-)\, dt = -\frac{e}{Cd}(w^- t + w^+ t)$$

where C is the capacitance, d is the distance between plates, e is the charge of an electron, t is the time it takes a particle to reach its respective electrode, and w is the drift velocity of the ion or electron. Since electrons move a few thousand times faster than ions [Tsoulfanidis 2015], it can be said that when t is less than the time it takes the electrons to reach the anode (T^-) the voltage change is linear. When time t is greater than T^- the pulse remains constant and finally at t equal to the time for the positive ions to reach the cathode the signal reaches its maximum value. Figure 13 shows this theoretical pulse shape.

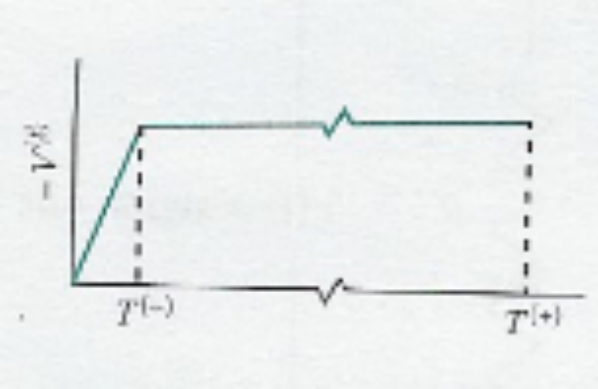

Figure 13 – Theoretical pulse shape for parallel plate ionization chamber [Tsoulfanidis 2015]

However, since the duration of this full pulse is too long for acceptable measurements to be made, a common practice is to terminate the pulse after the electron induced signal. This allows the system to be ready to detect incoming radiation at a much faster rate. This pulse is then fed into an RC circuit that produces the normal pulse shape seen from incident radiation in ionization chambers, which is shown in Figure 14. Effects

of the *Shockley-Ramo theorem* can be seen as the pulse approaches T^- in addition to the fast decay time after the electrons have been collected.

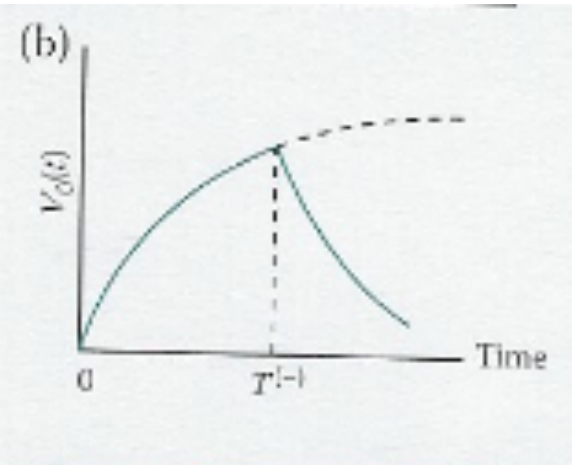

Figure 14 – Pulse shape for parallel plate ionization chamber [Tsoulfanidis 2015]

One way to shorten the pulse length is to introduce a Frisch grid [Knoll 2010]. This grid acts as a Faraday shield that separates the chamber into essentially two electrically isolated regions. Ions liberated within the region from the cathode to the Frisch grid stay within this region, traveling towards the cathode, as electrons travel towards the Frisch grid then on the anode. This creates the condition that a pulse will not be induced on the anode until the electrons have passed the Frisch grid. Once the electrons pass the Frisch grid, they experience a different field that leads to a voltage drop across this FG-Anode RC circuit. In the context of the theory for producing the pulse shape this leads to a shorter decay tail in the anode signal.

2.6 Energy Resolution

Energy resolution is a detector's ability to correctly characterize the incoming particle's energy [Aprile 2006]. A common practice for assessing energy resolution is to use the full width at half maximum (FWHM) of an energy distribution divided by the peak centroid [Knoll 2010]. Figure 15 shows a typical energy distribution with a Gaussian fit to illustrate where the FWHM is evaluated.

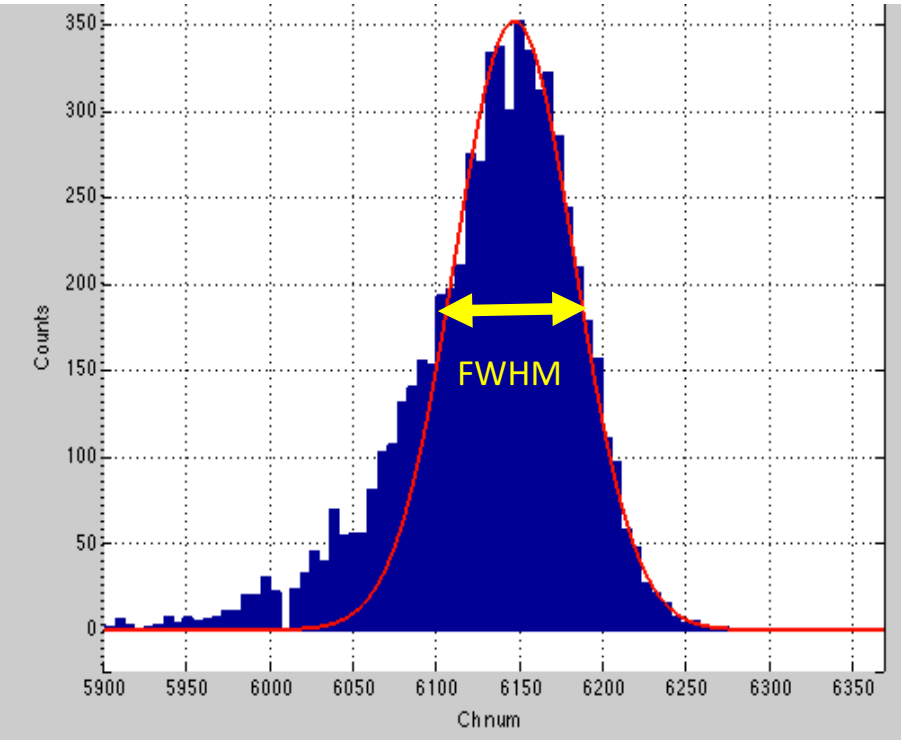

Figure 15 – ^{252}Cf alpha energy spectrum FWHM

By taking the resolution measurement at the FWHM we are assuming that any background or continuum on which the peak may be superimposed is negligible or has been subtracted away [Knoll 2010]. A narrower FWHM is desired for any energy

spectrum. This indicates that there are few fluctuations in the signals that are contributing to broadening of the peak. Some of the most common effects that can disturb the signal are electronic and vibrational noise.

2.7 Bragg curve spectroscopy

The Bragg curve is a plot of the specific energy loss along the track of a charged particle [Knoll 2010]. As a charged particle travels through matter it begins to lose energy through Coulomb interactions with the material, including ionization of the material. This mostly dominates the particle slowing process until the particle has lost a significant amount of energy and reaches a very low velocity. This interaction is well described by the Bethe formula.

$$-\frac{dE}{dx} = \frac{4\pi k_0^2 z^2 e^4 n}{mc^2\beta^2}\left[ln\frac{2mc^2\beta^2}{I(1-\beta^2)} - \beta^2 \right]$$

The variables in this equation are as follows:

$k_0 = 8.99 \times 10^9$ [N m^2 C^{-2}]

z = atomic number of the heavy particle

e = magnitude of the electron charge

n = number of electrons per unit volume in the medium

m = electron rest mass

c = speed of light in vacuum

$\beta = v/c$ = speed of the particle relative to c

I = mean excitation energy of the medium

This equation states that as the velocity, or β, decreases the stopping power (-dE/dx), and thus ionizations in the material, increases. This effect can be seen through the Bragg peak in the plot of ionization vs. distance in Figure 16. As the particle passes through the material, in our case the detector gas, it begins to lose more and more energy per unit length until ionization no longer dominates and atomic collisions take over, creating this Bragg peak occurring at the end of the particle's path.

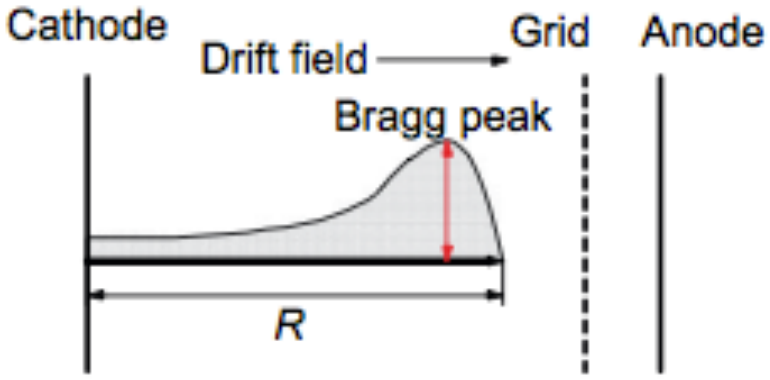

Figure 16 – Model of a Bragg curve within a gridded ionization chamber [Sanami 2009]

This peak does not depend on the initial energy that is seen in the full integral of the ionization in the material, but is dependent on the particle's charge following the Bethe equation. By examining the peak size, the information on Z may be extracted.

For gas detectors Bragg curve spectroscopy is based on the spatial distribution of the liberated electrons caused by the particle interactions in the gas [Knoll 2010]. The gas detector is wired to have parallel E field lines, so electron drift timing is not affected by field distortions. The electrons drift past the Frisch grid, with the front of electrons passing first and so on, and so the time characteristics of the induced anode pulse gives information where in the detector the electrons were liberated. The shape of the rise of the output pulse can then give information of the particle's energy loss as it traverses the chamber [Knoll 2010]. In the case of ionization chambers, where high-resolution energy readings can be made, an analysis of the difference in pulse height can yield information on the charge of the ion. Figure 17 shows the relation between the Bragg peak height and the incident particle energy. It clearly shows the difference that charge has on the height of the Bragg peak, given that the particle has enough energy to create a distinguishable Bragg peak. At lower incident particle energies, it is harder to distinguish between ions, but above about 1 MeV/amu a clear separation is noticed. Particles below about 1 MeV/amu cannot be distinguished using Bragg curve spectroscopy leading to a need for other methods for fission fragments.

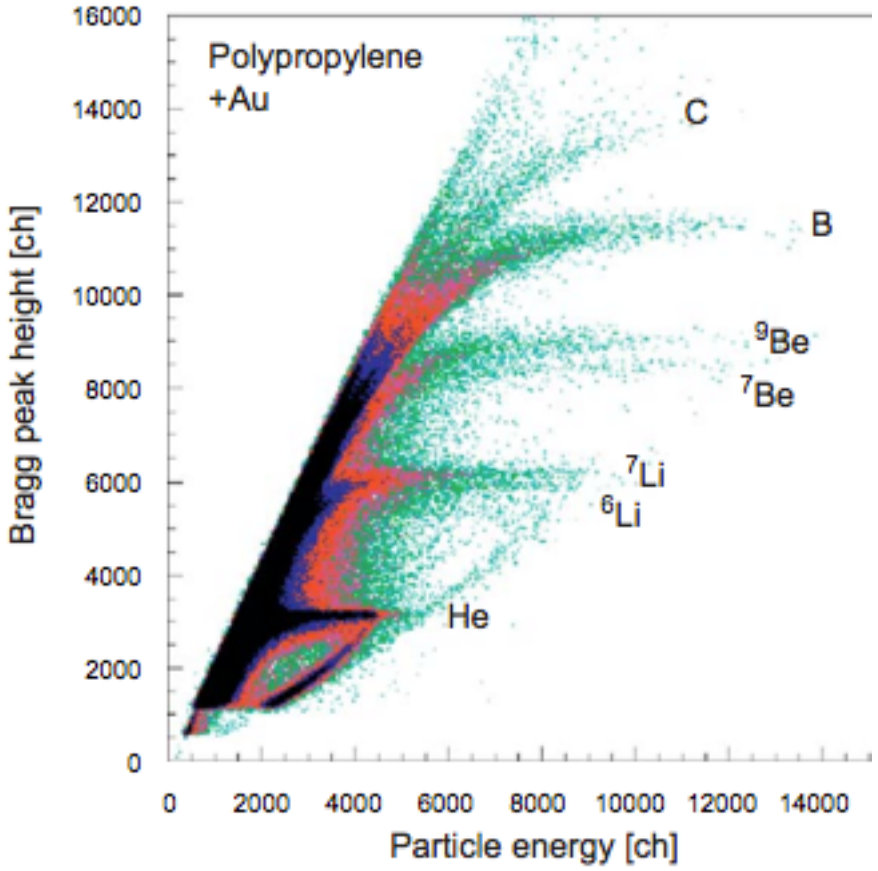

Figure 17 – Bragg curve pulse heights for different energy ions [Sanami 2009]

2.8 Range Calculations for Z Determination

A method to determine the atomic charge of fission fragments was implemented by Tyukavkin *et al*. [Tyukavkin 2008]. This method relates the drift velocity of the electrons and the time difference (D) between induced pulses on the electrodes of the ionization chamber to get the range that the particle penetrates into the chamber following the equation:

$$R = L - Dv_{dr}$$

This simple relationship states that the range of a particle is equal to the physical length of the chamber minus the drift time of the electrons (D) times the drift velocity of the electrons. The chamber is wired to have parallel E field lines, so the drift time is only a function of distance from the electrode plates. This relationship, in essence, is what allows the ionization chamber to function as a time projection chamber (TPC). As a particle enters an ionization chamber through the entrance window and begins to deposit its energy, the electrons created induce a pulse on the cathode as they begin to move towards the Frisch grid. Once this electron group begins to pass the Frisch grid a pulse is induced on the anode. The time difference between these two pulses can be measured as the time it took the electrons to travel from where the incident particle stopped to the Frisch grid. Figure 18 shows the time difference measured between the induced pulses on the cathode and anode in the UNM ionization chamber.

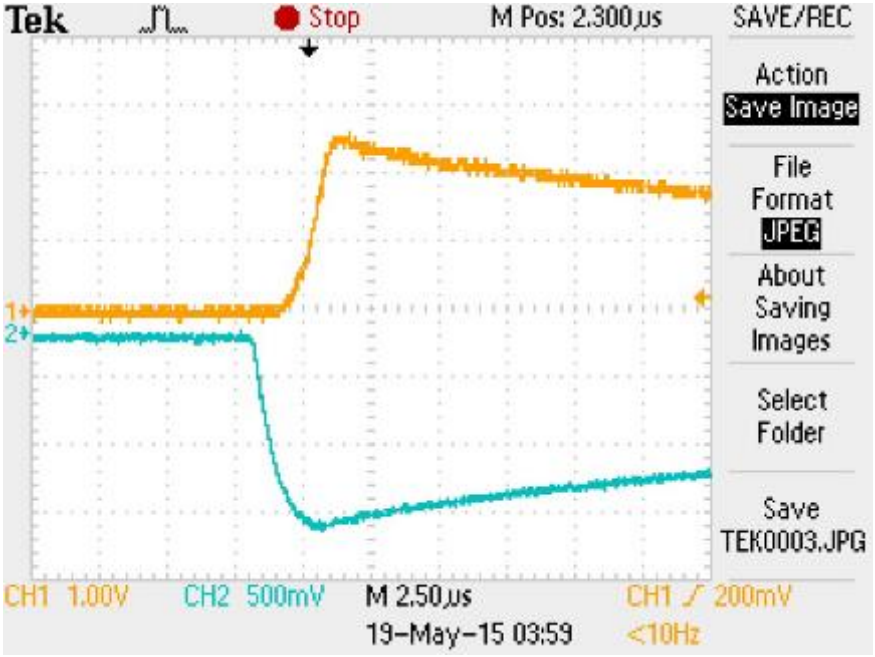

Figure 18 – Time difference between induced pulses on cathode (blue) and anode (orange)

The orange curve shows the anode pulse and the blue curve shows the cathode pulse. The difference between when these two pulses start is the value used for this method. This means that for particles being stopped near the Frisch grid a short D will be measured and a longer D will be measured for particles that stop near the cathode.

Once the range has been determined the atomic number can be extracted. Tyukavkin *et al*. use the relationship:

$$R = \beta\sqrt{EM}Z^{-2/3}$$

that relates the range of the particle to its energy (E), mass (M), and atomic number (Z). Figure 19 shows data for Rb and Se vs. fit lines based on this method.

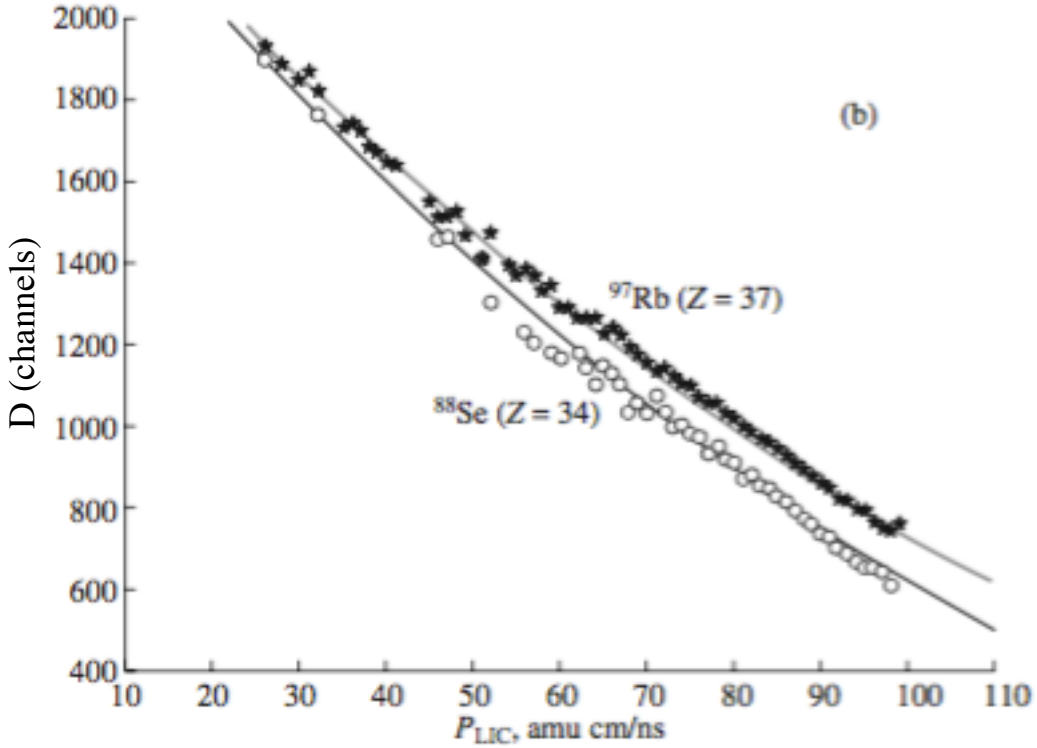

Figure 19 – Atomic charge based on Tyukavkin method for theoretical model and experimental data for ^{97}Rb and ^{88}Se [Tyukavkin 2008]

Figure 19 shows that for a given drift time (y-axis) there are multiple momenta (x-axis), or velocity and energy measurements, that are obtained which comes from the difference in the atomic charge. This method allows for charges of < 1 MeV/amu to be detected making it more suitable for fission fragments.

3 Methodology

A cylindrical ionization chamber with electrodes on each end was chosen and designed to yield the most reliable energy data over a wide spectrum of particle energies. Ion chambers are robust, durable, easily scaled, and easy to operate making them well suited for this project. They do not accumulate damage like solid-state detectors do, and have higher energy resolution than Si surface barrier detectors for heavy ions. In addition to their easy design the general principle under which ion chambers operate is ideal to obtain the desired data. The linear relationship between the pulse height and the energy deposited allows for a detailed map of the fission product spectrum to be measured. This chamber also has the ability to measure a drift time of the liberated electrons due to the active cathode set-up making it possible to investigate particle range and thus Z.

3.1 Ionization Chamber Design

The ionization chamber, shown in Figure 20, is a cylinder with two copper electrodes, the anode and the cathode, on the ends. The Frisch grid, 7mm from the anode, is a copper ring that was electroplated gold and has a thin gold wire mesh grid. The active region for measurement is considered the region between the cathode and the Frisch grid. Surrounding the active region is a series of 15 copper guard rings (GR) that serve to keep the electric field lines parallel. Each guard ring is equipped with a 100 MΩ resistor to ensure a reduction in voltage between each ring and create a gradual reduction in field. This has the effect of mimicking an infinite parallel plate construction and keeps the field lines parallel within the ionization chamber. The cathode is an annulus with a central hole

to accommodate the aluminum window holder with its silicon nitride window that serves to separate the ionization chamber from the TOF system. The window holder is wired to the cathode annulus and acts as part of the cathode. All of the components are mounted on Teflon insulating rods. Teflon was chosen for its low conductivity and low out-gassing properties.

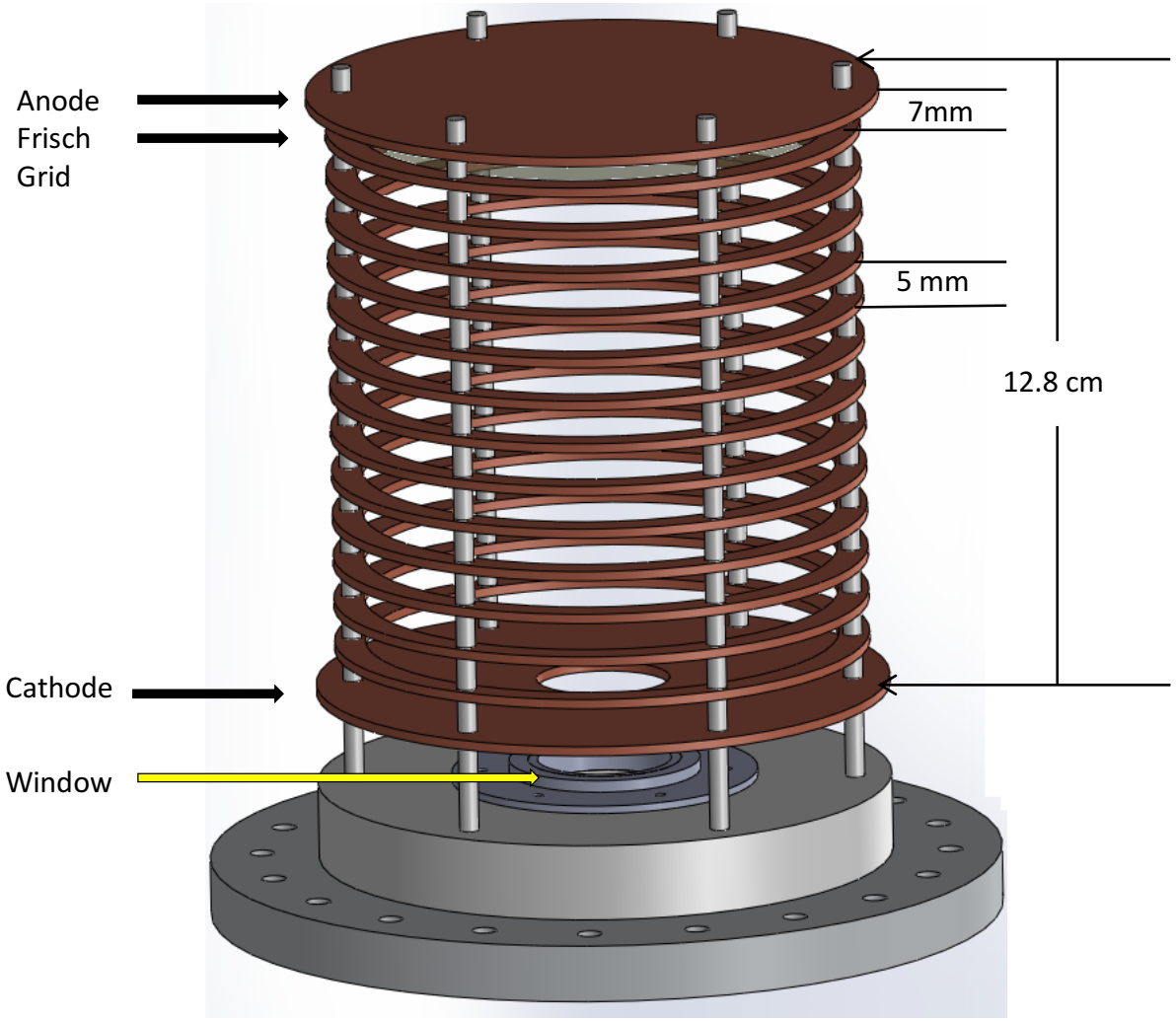

Figure 20 – Model drawing of ionization chamber (Heffern 2015)

The active length of the chamber, the distance from the cathode to the Frisch grid, is 11.8 cm. Each guard ring is approximately 5 mm apart. Figure 21 shows the ionization chamber in its current arrangement. Figure 22 shows a simplified schematic of the electrical circuit of the ionization chamber.

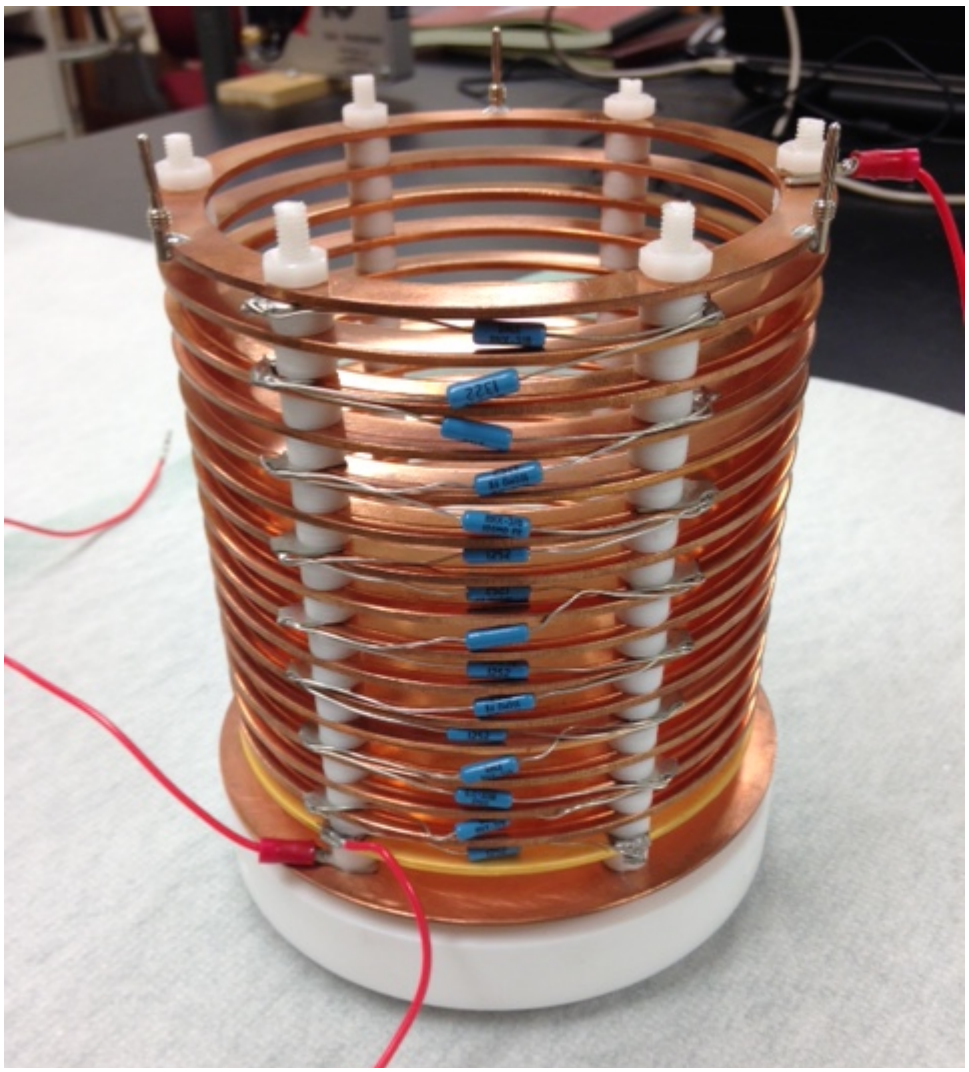

Figure 21 – Ionization chamber

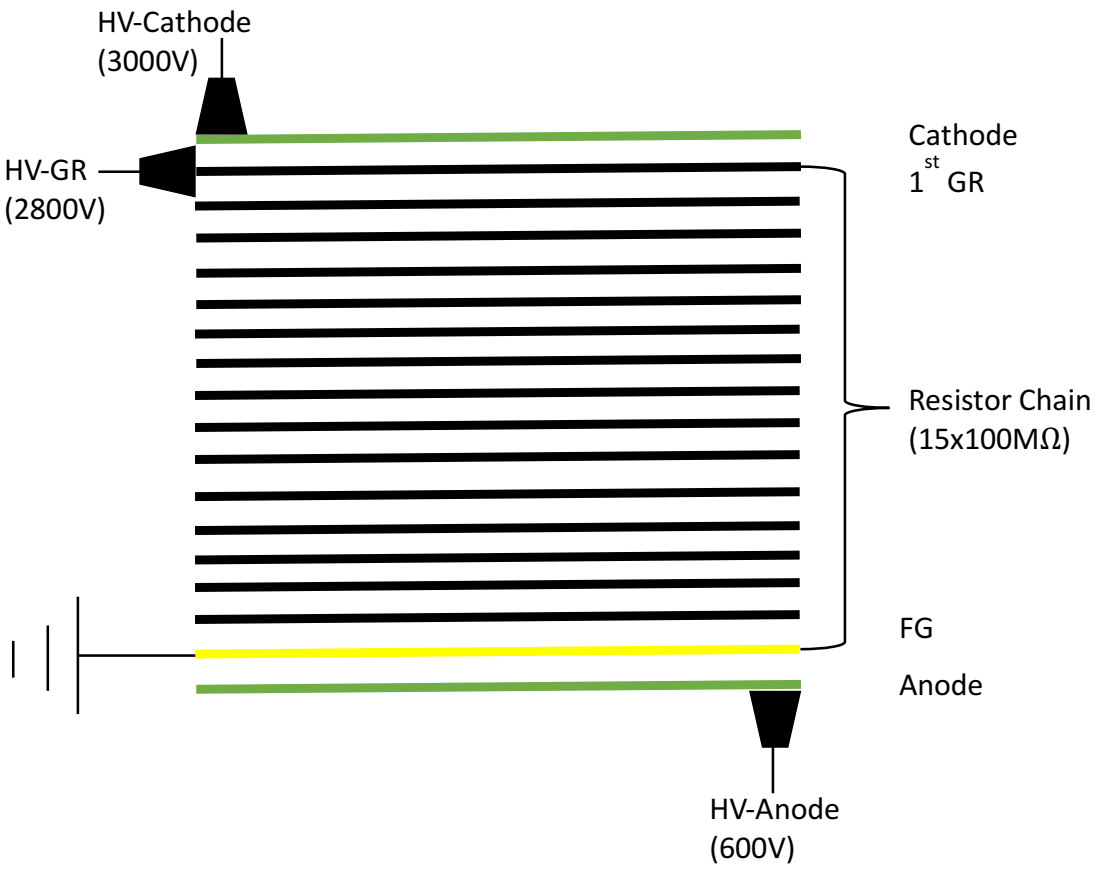

Figure 22 – Ionization chamber electrical circuit schematic

The schematic in Figure 22 gives the values of the cathode, guard ring, and anode voltages used for fission fragment operating conditions. The cathode and first guard ring (GR) are powered separately to reduce cross talk to the cathode. Then the voltage is equally stepped down by each subsequent GR through the resistor chain until it reaches the Frisch grid (FG) that is tied to ground. The anode is powered by its own HV supply with a difference in voltage between it and the FG but no direct electrical contact, again to prevent cross talk.

3.2 Operating Parameters

3.2.1 Electronics

The ionization chamber has a simple electronic set-up. An Ortec 142PC preamplifier powered by an Ortec 659 high voltage supply receives the incoming pulse for the cathode and anode individually. The output from the preamp is sent to two different systems. One output is sent directly to a CAEN DT7524 + DPP-PHA Firmware desktop digitizer. The second output is sent to a Model 715 PS Timing discriminator. The output from the discriminator is fed into an Ortec 467 time to pulse height converter (TPHC) with a 1μs range. The output from the TPH is then sent to the CAEN desktop digitizer. Figure 23 shows a block diagram of the electronics used for this experiment. The guard rings are powered separately from the cathode by an Ortec 659 high voltage supply.

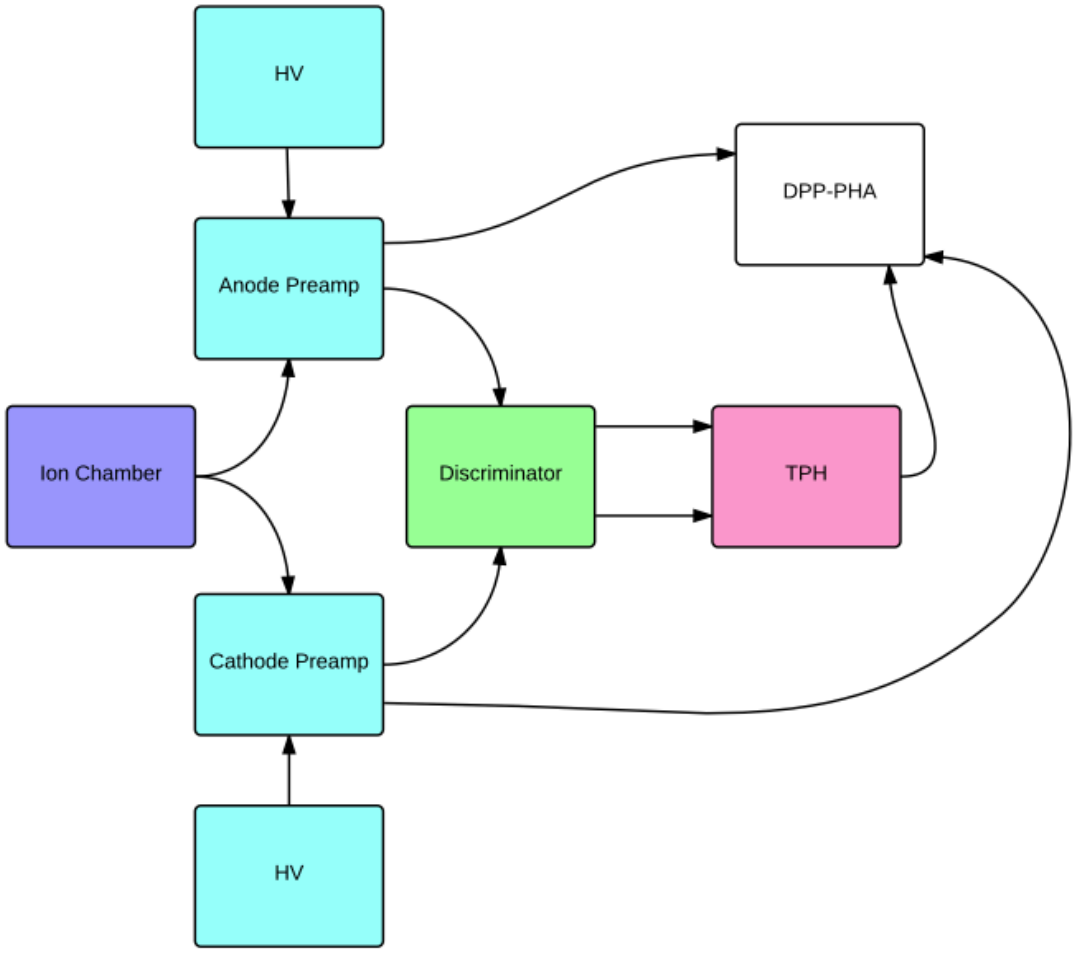

Figure 23 – Electronics block diagram for the ionization chamber signal treatment and voltages.

3.2.2 Gas Handling System

P-10, or more recently isobutane, is used as the ionization gas. To keep the signal response consistent within the gas, in case of degradations due to air contamination from leaks, outgassing of materials in the detector, or damage due to radiation, the gas is refreshed by a continuous flow through the chamber during operations. The gas flow into the chamber is regulated by a MKS 250 pressure system. The outflow of the chamber is

regulated by a MKS 246 flow rate system. The MKS 246 is set to refill the entire volume of the chamber every 2 hours due to degradation in the quality of the gas. The outflow controls are set based on the specific type of gas being used. Appendix A gives the settings used for isobutane.

3.2.3 Window

The material chosen as the entrance window separating the TOF chamber and the gas filled ionization chamber is extremely important. This material must be able to hold a differential pressure of vacuum on one side and approximately 1/3 atmosphere pressure of ionization gas on the other, with low enough porosity to maintain high vacuum on the vacuum side. In addition to having this structural stability the window must be thin enough to minimize the energy loss and consequently energy broadening (straggling) of the particles as they pass through the window into the ionization chamber. Mylar has commonly been used to fulfill these requirements, and a 1.5 μm thick Mylar window was used for some of this work. A 0.9 μm Mylar window was attempted but the fill gas seeped through too rapidly. As a measure towards minimizing energy loss and straggling, a thin silicon nitride (SiN) window has replaced Mylar. SiN exhibits less stretch than Mylar, but a very thin, small area window is able to maintain the required pressure difference and has a low porosity for the ionization gas. A 1 cm x 1 cm x 200 nm thick SiN window is currently being used for this experiment. Figure 24 shows the window installed in the aluminum frame.

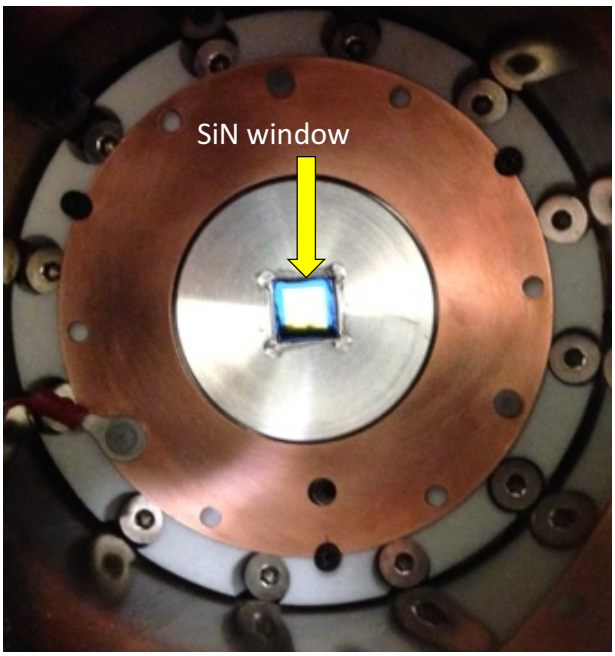

Figure 24 – SiN window

The window is glued to the frame by NuSil silicone adhesive, which has similar physical properties to the SiN window, which reduces the stress felt on the window while still holding a seal. This combination of glue and window thickness has been successfully tested to withstand a pressure differential of 130 Torr without failure. This pressure is important because it is an operating condition to evaluate alpha particles, which was used to characterize many aspects of the ionization chamber.

3.2.4 Detector Gas

As stated in the theory section, the choice of detector gas is critical to the overall operation of the detector, most importantly in determining the energy resolution that can be achieved. A gas with a high stopping power is required for use when a thin widow has

been implemented. This allows for a lower operating pressure, putting less stress on the window, while still enabling full energy deposition of incident radiation. To obtain these conditions isobutane was chosen as the fill gas for the ionization chamber.

3.2.4.1 Density and Stopping Power

Isobutane recently has been put into use for the detector gas. P-10, which is a mix of 90% argon and 10% methane, is commonly used for gas-filled detectors and was the gas used prior to installation of the SiN window. As a comparison of these two gasses the most relevant physical properties are given in Table 3.

Table 3 – Isobutane and P-10 physical properties at STP

Isobutane and P-10 Physical Properties		
	P-10	Isobutane
Density [kg/m^3]	1.45	2.51
Molecular weight [g/mol]	37.6	58.1
R [J/kgK]	237.9	147.9
Chemical composition	CH_4(10%)-Ar(90%)	C_4H_{10}

Following the Bethe equation, stopping power goes as the electron density of the material, so for higher density materials, less material may be used. For gasses, the ideal gas law states

$$P = \rho RT$$

(where R is the specific gas constant, ρ is the density of the gas, and T is the temperature). For gasses with different densities at the same temperature, the denser gas can be used at a lower pressure and have the same stopping power as the less dense gas at a higher pressure. It can be seen from the values given in Table 3 and the Ideal Gas Law that for the same temperature, isobutane allows for much lower operating pressures for the same stopping power due to its higher density. Figure 25 shows the stopping power versus velocity, or different kinetic energy, for cobalt ions at different pressures of isobutane.

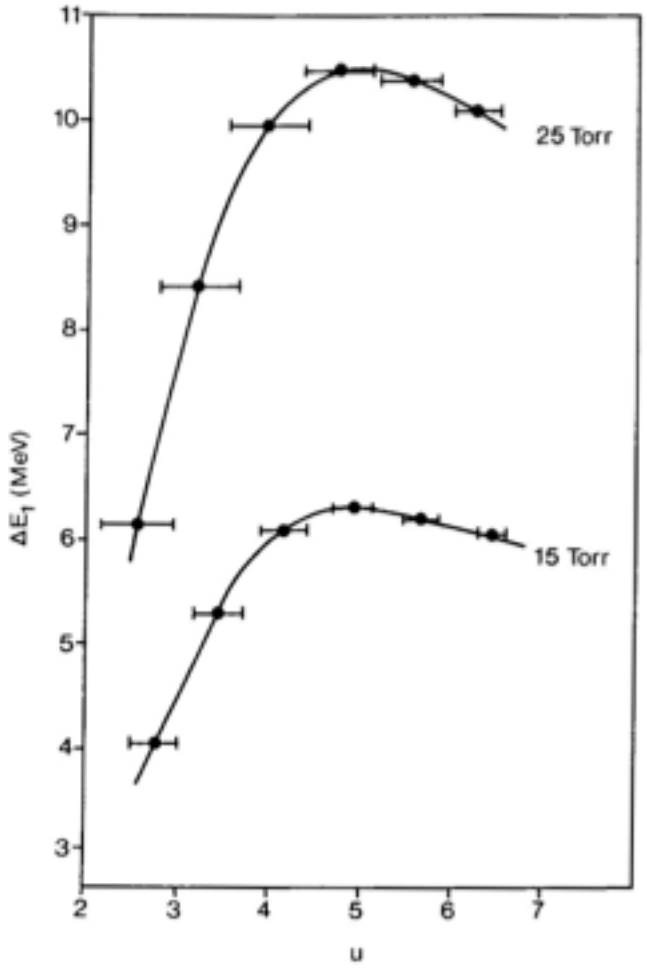

Figure 25 – Stopping power for isobutane vs. velocity at different pressures. The x-axis is the velocity and the y-axis is the energy loss measured. [James 1982]

Figure 25 shows that as the pressure increases the stopping power also increases. In the case of fission fragments with incident initial kinetic energies up to 100s of MeV entering an 11.8 cm active region of the ionization chamber, a gas capable of reducing the incoming energy by 10 MeV per cm is needed.

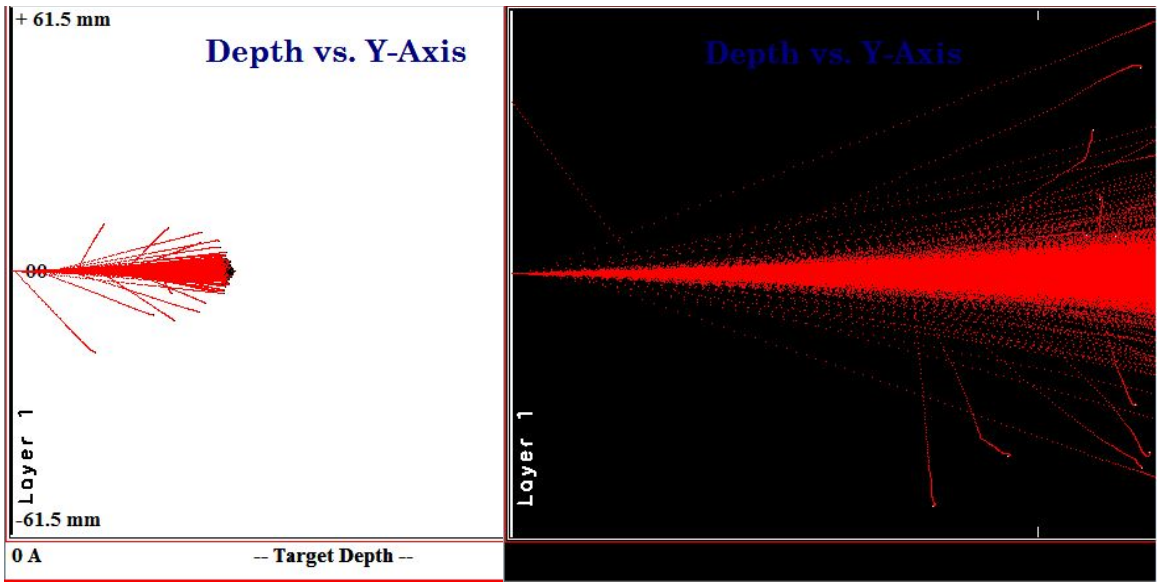

Figure 26 – SRIM ^{252}Cf alpha interaction calculations for 300 Torr of isobutane (left) and P-10 (right) [SRIM 2008] with the same horizontal scale, to show stopping power differences.

Figure 26 shows a SRIM [Ziegler 2008] simulation of a particle of the same mass and energy traveling into isobutane and P-10 at the same pressure. This simulation was performed using a ^{252}Cf alpha with energy of 6118 keV going through a 0.347 μm carbon foil, a 200nm SiN window, and 300 Torr of either isobutane or P-10. Although the SiN window would never be used with P-10 it is used here to illustrate the effects of only the gas on the range of the particle. Figure 26 shows that for 300 Torr of isobutane the alpha only goes approximately 61.5 mm into the gas, whereas for the P-10 gas most of the alphas are punching through the entire length of the chamber. This simulation is consistent with isobutane having a much higher stopping power than that of P-10.

3.2.4.2 Drift Velocity

Another important property that is considered for the detector gas is the electron drift velocity, as discussed in Section 2.5. Figures 27 and 28 show drift velocity curves for P-10 and isobutane, respectively. Both of these graphs give the drift velocity as a function of the reduced electric field or E/P. It shows that for slight changes in either the electric field or pressure there can be dramatic effects on the drift velocity of the electrons, which is believed to be constant in a uniform electric field. To reduce the variation of these effects, nominal operation points are chosen where the slope is a minimum. In the case of P-10, the slope is minimized at the rollover of the curve. This gives a very small range for which fluctuations have little effect on the drift velocity. Isobutane, however, has a more gradual curve and appears to only stabilize towards the end of the available data. This drove us to operate as close to the maximum value of E/P given by this curve in order to maintain a stable drift velocity.

Obtaining a constant drift velocity is important in getting consistent timing data within the ionization chamber. As stated in the range theory section, our method of calculating the range is dependent on two factors; the drift velocity of the electrons and the timing difference between the cathode and anode pulses. Therefore, minimizing the variation in the drift velocity over time allows for a more consistent collection of electrons created within the chamber. A constant drift velocity also minimizes the uncertainty in calculating the range of the particle.

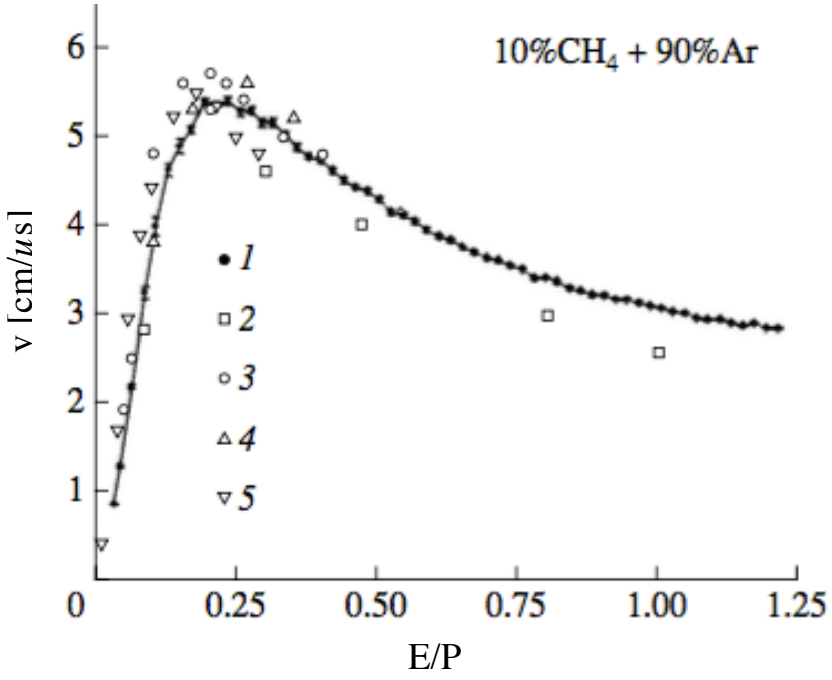

Figure 27 – Electron drift velocity curve for P-10 gas with E/P [V/cm*Torr] values (x-axis) and drift velocity (y-axis) [Khryachkov 2003]

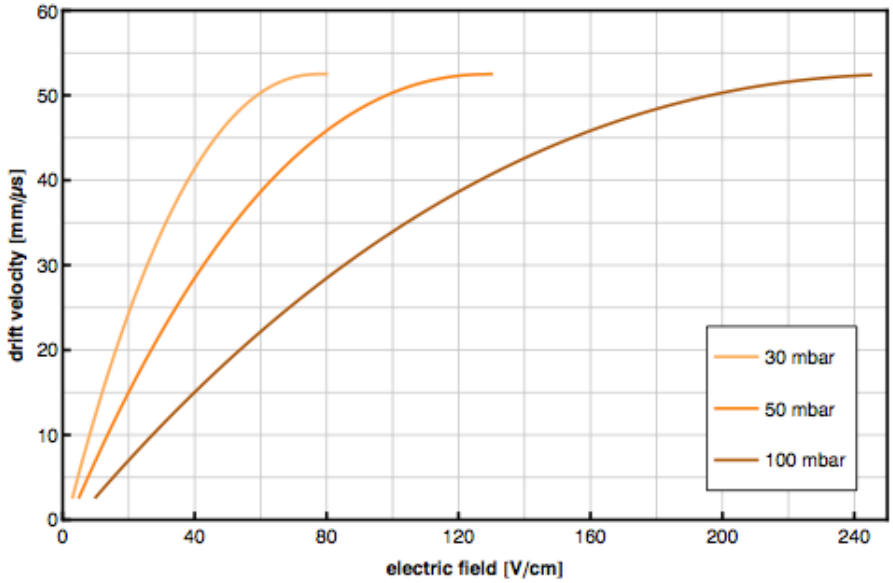

Figure 28 – Electron drift velocity curve for isobutane gas [Buchriegler 2013]

3.3 Post Processing Code Development

3.3.1 Energy Calibration

When data is obtained it is recorded as a channel number and a pulse height. Due to the properties of the ionization chamber this pulse height is proportional to the energy deposited by the incident radiation. There are slight corrections, different depending on the E and A of the nuclide, which will be discussed as part of the general energy addback work. This allows for a simple calibration to convert the pulse height to an energy reading. The fission product distribution is a very wide distribution due to a variation in the masses and energies emitted. However, there is a group of products for both the heavy and light peak that make up the majority of the yield as seen in Figure 29.

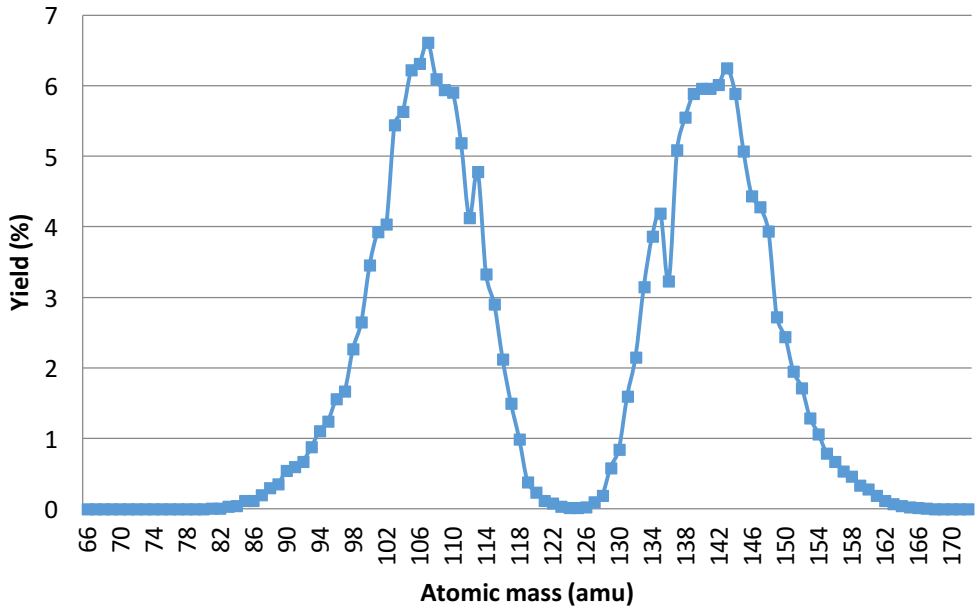

Figure 29 – Isotope mass yield for spontaneous fission of ^{252}Cf fission fragments

The elements that make up the light and heavy peak are Y to Ag and Sn to Pr respectively. Therefore, an average mass and energy is taken that represents the elements that comprise each peak. Table 4 gives the averages used as the calibration points for ^{252}Cf. The value for each energy peak is then assigned to a channel number representative of the average of each peak and a linear fit calibrates the remaining data. The mass can then be calculated as stated in the theory section. The mass values from Table 4 are used as a verification of the energy calibration. Appendix B gives the MATLAB program used for this analysis. Figures 30 and 31 show an un-calibrated and calibrated energy spectrum respectively. Figure 30 shows the bin center is 9980 that corresponds to the channel number and in Figure 31 that channel number now reads in energy as 78.600 MeV.

Table 4 – Calibration values for ^{252}Cf [Schmitt 1965]

Calibration Values for ^{252}Cf	
Variable	Value
E_l [MeV]	103.77
E_h [MeV]	79.37
m_l [amu]	106
m_h [amu]	141.9

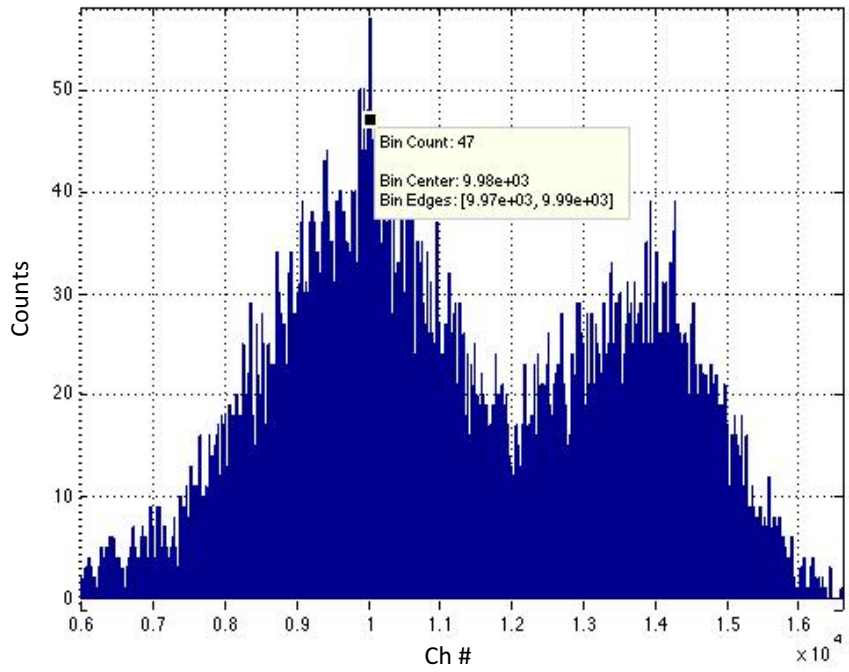

Figure 30 – Un-calibrated ^{252}Cf fission product spectrum (Ch num vs. counts)

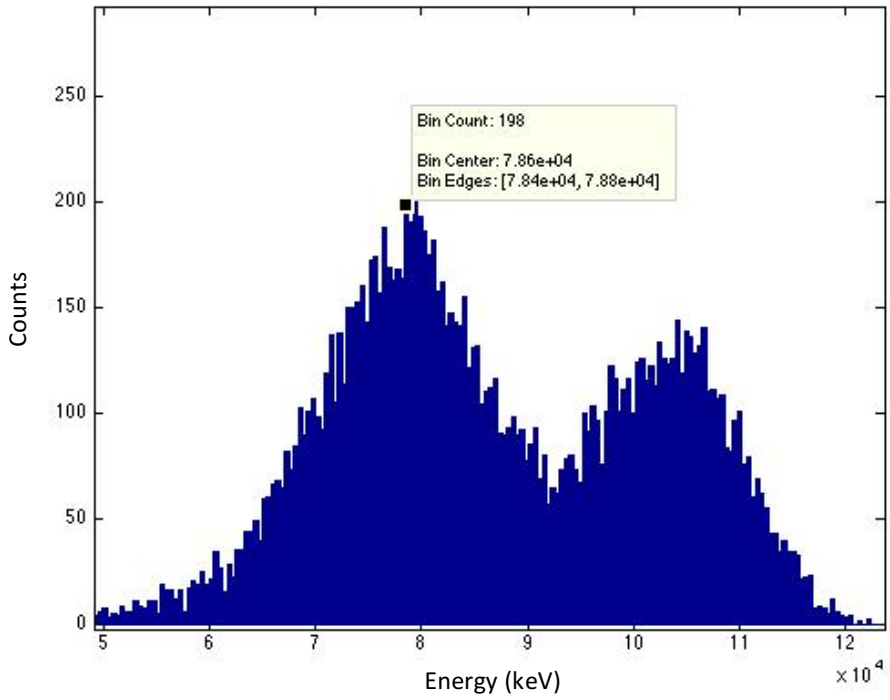

Figure 31 – Calibrated ^{252}Cf fission product spectrum (Energy vs. counts)

3.3.2 Energy Add Back

The particle loses energy each time it passes through a foil or into the IC through the IC gas window. The mass of the particle is calculated from TOF and E, and so it is important to know the energy in the TOF region. This means that energy that has been lost to the first carbon conversion foil must be accounted for and restored to the IC measured E value for the mass calculations. Figure 32 gives a schematic of the kinetic energy divisions as seen by the detector.

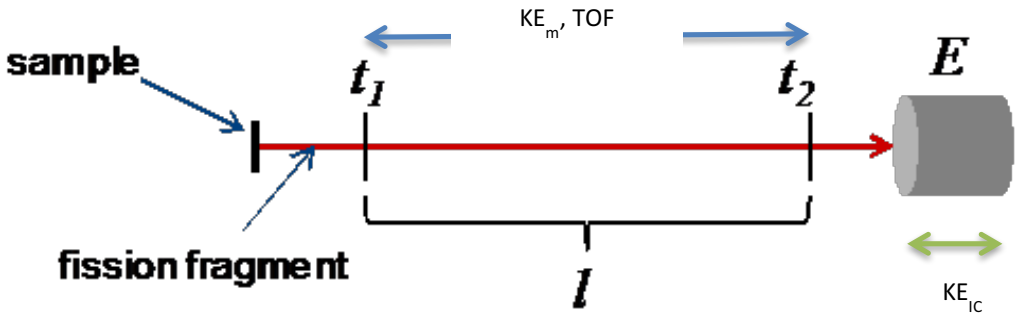

Figure 32 – Kinetic energy divisions

In this figure KE_{IC} is the energy deposited in the ionization chamber and KE_m is the kinetic energy we wish to obtain to make mass calculations. The difference, the add-back energy, is the energy that is lost to the 2nd carbon foil and the SiN window. Using the Stopping and Range of Ions in Matter (SRIM) [Ziegler 2008] code and work done by Madland we obtain a theoretical model to address the add-back. The first step was to use momentum balance for the total energy given to fission products to find the initial kinetic energy for each fragment. The equation below gives the energy to the fragment for post-prompt neutron emission for ^{235}U [Madland 2006]

$$KE_{tot} = 169.1 - 0.2660E_n\ [MeV]$$

where *En* is the neutron energy. In the case of thermal fission which is what we are interested in, *En* is 0.025 eV. This energy is then used in the following equation to obtain the initial kinetic energy for each isotope,

$$KE_i = \left[\left(\frac{m_r}{m_{tot}}\right) * KE_{tot}\right] - E_n$$

where m_r is the total mass minus the mass of the nuclide and m_{tot} is the total mass. Using SRIM the energy loss through the first carbon foil gives KE_m and its respective TOF. Again, SRIM KE_m is used as the energy sent through the second carbon foil and the window giving us KE_{IC}. Table 5 gives an example of the values used and the amount of energy loss through the carbon foils and window. The values given as an example in Table 5 are for ^{235}U isotopes passing through a carbon foil and 2.5 μm Mylar.

Table 5 – Energy add back values

Element	Z	A	E initial [MeV]	E through foil 1 [MeV]	TOF [s]	E Add Back [MeV]
Br	35	88	106.646	102.765	3.333E-08	22.848
Kr	36	90	105.185	101.222	3.396E-08	23.705
Rb	37	92	103.724	99.844	3.457E-08	22.751
Sr	38	95	101.533	97.445	3.556E-08	23.955
Y	39	97	100.072	96.022	3.620E-08	23.634
Zr	40	100	97.881	94.024	3.714E-08	22.379
Nb	41	101	97.15	93.077	3.751E-08	23.853
Mo	42	104	94.959	90.702	3.856E-08	24.656
Tc	43	104	94.959	90.637	3.858E-08	24.961
Cd	48	130	75.967	72.008	4.839E-08	22.245
In	49	129	76.698	72.682	4.798E-08	22.547
Sn	50	130	75.967	71.954	4.841E-08	22.5298
Sb	51	133	73.776	69.807	4.971E-08	22.217
Te	52	134	73.045	69.078	5.016E-08	22.214
I	53	135	72.315	67.972	5.076E-08	23.670
Xe	54	138	70.124	65.45	5.230E-08	25.042
Cs	55	141	67.932	64.07	5.343E-08	21.254
Ba	56	143	66.471	62.662	5.441E-08	21.001
La	57	145	65.01	61.227	5.542E-08	20.724

200 nm silicon nitride has a much smaller effect than 1.5 micron Mylar on the amount of energy loss per particle as it passes into the ionization chamber. Figure 33 gives a comparison of the amount of energy loss for SiN and Mylar windows.

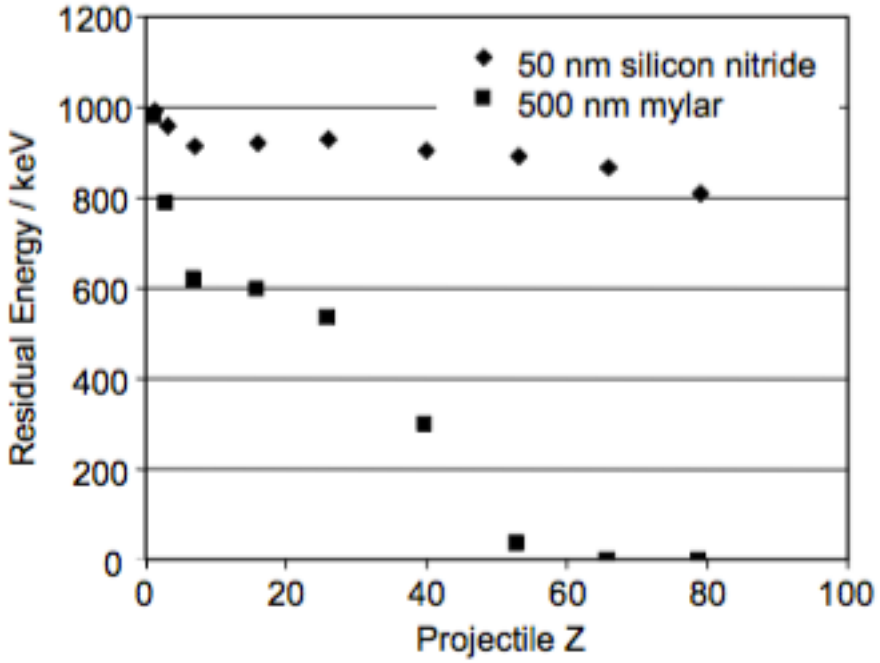

Figure 33 – Energy loss for 1 MeV ions [Dobeli 2004]

Figure 33 shows that there is a much more significant loss in energy through Mylar than that for SiN as the particle's charge increases. This property of SiN is highly desirable and will lead to more consistent energy readings for higher Z products and minimizes the effect of "add-back" corrections to yield proper mass data. Additionally, energy-broadening increases with greater energy loss, so thinner windows are necessary for lower proportional uncertainty.

4 Results

With the implementation of the SiN window and isobutane, little was known about the overall behavior of the detector. Many tests were done to understand the two main aspects of the ionization chamber: the energy resolution and the time difference, or Δt, under this configuration. The results presented for alpha energy resolution are obtained primarily for a 200 nm SiN window and isobutane set-up. Heffern has reported previous alpha energy resolution results for a Mylar and P-10 combination. The timing data reported is a combination of both P-10 and isobutane ionization chamber configurations.

4.1 ^{252}Cf Alpha Energy Resolution

The most important parameter of the ionization chamber is the ability of the detector to resolve the incident radiation energy. To assess this, many test were done to determine the effects on the overall resolution. These tests were performed using alpha particles due to their single energies and high-count rates. Since a real resolution for fission fragments cannot be obtained due to the wide spread in energies that can be observed for any given fragment species, an alpha resolution is presented.

The first test was performed to determine if a specific pressure gave the best resolution. Figure 34 gives the alpha energy resolution versus different pressures for a reduced electric field of 1.2.

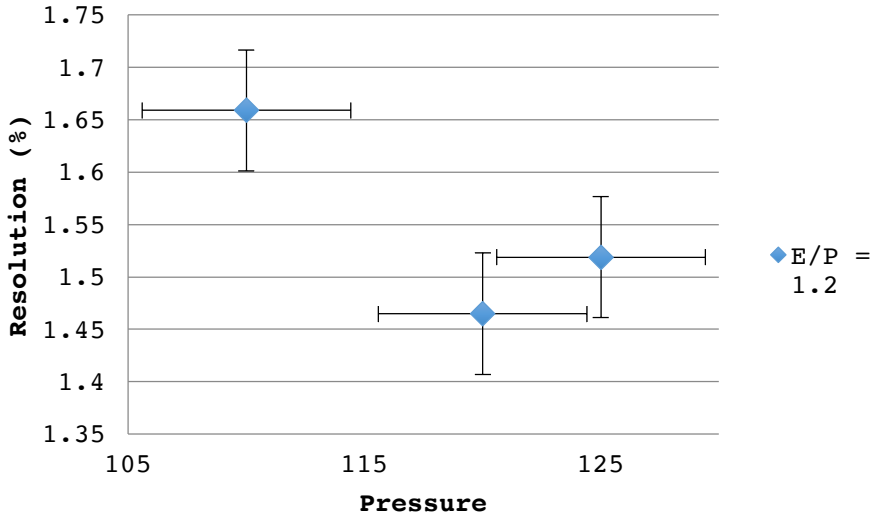

Figure 34 – ^{252}Cf alpha energy resolution for constant E/P of 1.2 with varying pressure in Torr

This shows that the lowest energy resolution was obtained for 120 Torr. Many factors are of concern for these results. First, the optimum E/P ratio for isobutane is approximately 3.25 as given in Figure 28. This means that the electrons are not moving at their maximum velocity in the data in Figure 34. This increases the probability of a competing reaction occurring that could reduce the collection of the electrons that affects the pulses obtained. Another important note is that small changes in pressure greatly affect the stopping power of isobutane. It is believed that for a pressure of 110 Torr the stopping power is not great enough to fully stop the alphas, which leads to a broadening of the spectrum and therefore increases the resolution obtained. In addition, a pressure of 125 Torr can be too great and would therefore cause the alphas to stop too far from the Frisch grid, where electrons created might not be detected due to competing events. Another major issue that was observed across all the results presented was the effects of electric

breakdown and shorting due to the high voltages being applied to obtain the desired reduced electric field. More information about breakdown and its effects on the system are discussed in Appendix C.

Another test was done to determine the effect that varying the reduced electric field at a constant pressure would have on the resolution obtained. Figure 35 shows the resolution obtained from varying the reduced electric field for three different pressures of isobutane.

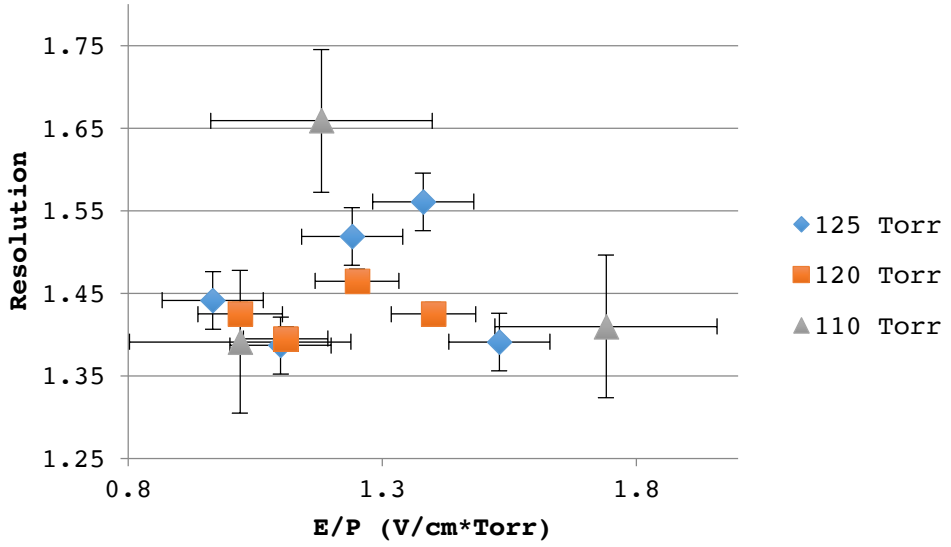

Figure 35 – ^{252}Cf alpha energy resolution vs. E/P for SiN window and isobutane gas at various pressures

Figure 35 shows that for a pressure of 120 Torr the resolution remained the most consistent at approximately 1.4%.

In addition to varying the reduced electric field, the ratio between the cathode to Frisch grid (C-FG) region and the Frisch grid to anode (FG-A) region electric fields was

explored to see the effect on the alpha resolution. Figure 36 shows the alpha resolution measured for varying field ratios with a constant reduced electric field of 1.4 V/cm*Torr.

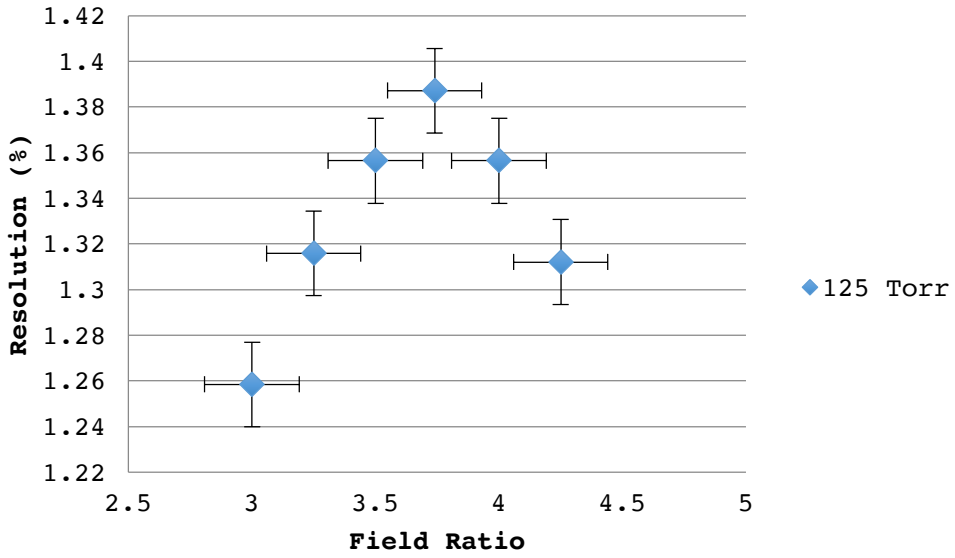

Figure 36 – ^{252}Cf alpha energy resolution vs. field ratios at a constant pressure of 125 Torr isobutane gas

This figure shows that a lower C-FG/FG-A field ratio resulted in the best resolution obtained. The downturn at higher field ratio values is an interesting result and it is still unclear as to why this would occur.

Overall there was a small improvement in the alpha particle energy resolution obtained from the use of SiN window and isobutane gas, 1.25%, as compared to the Mylar and P-10 gas, 1.33%. Figures 37 and 38 show the best-obtained alpha resolution for these two combinations of entrance window and stopping gas. Electrical breakdown issues, to be addressed, prevented more data acquisition for resolution characterization.

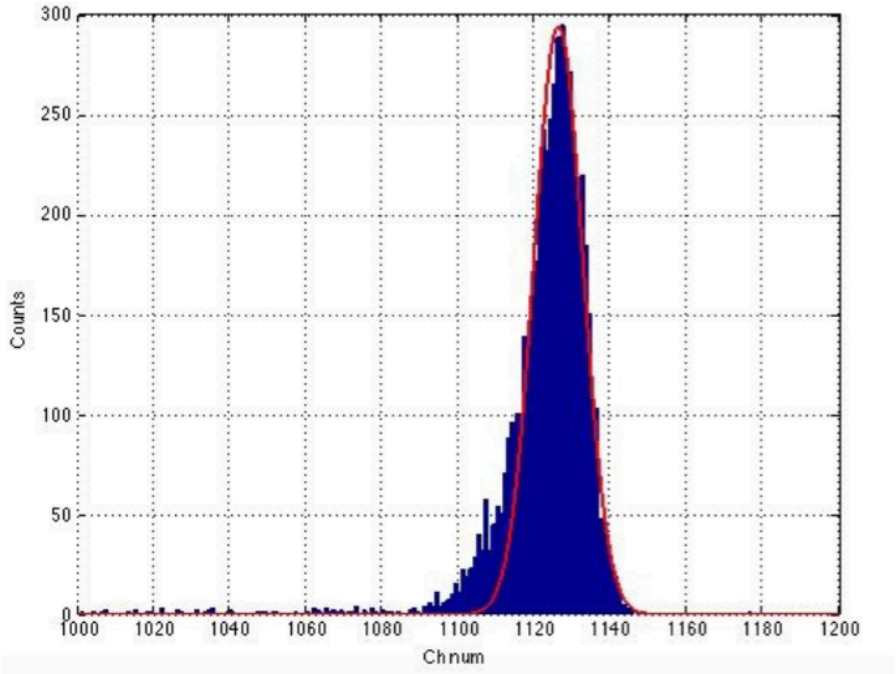

Figure 37 – ^{252}Cf alpha spectrum with Gaussian fit for P-10 gas and 1.5 µm Mylar

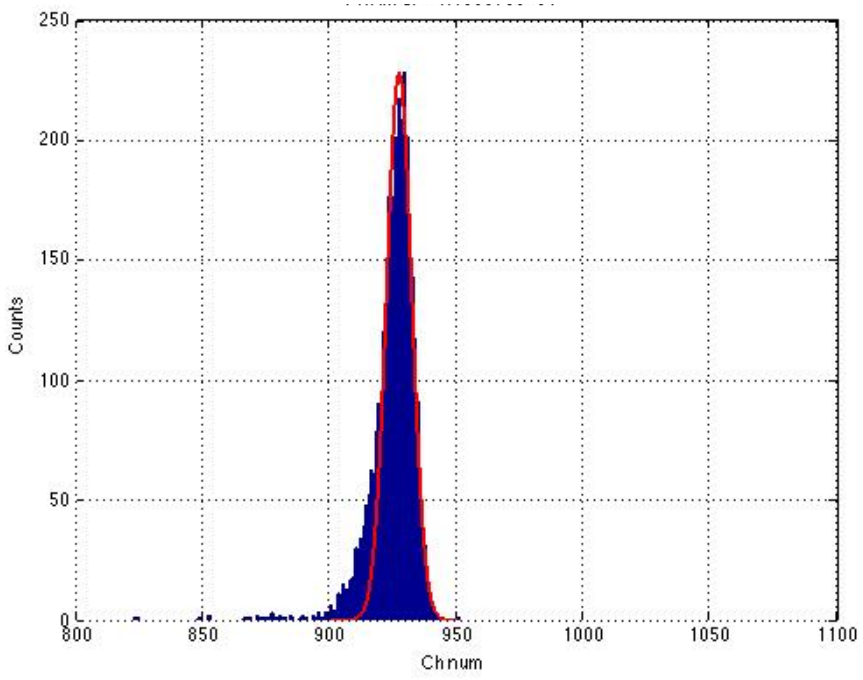

Figure 38 – ^{252}Cf alpha spectrum with Gaussian fit for isobutane and 200 nm SiN window

After a thorough investigation into the cause of the electrical breakdown was conducted and resolved, a more reliable measure of the detector energy resolution was performed. This was done using a tri-nuclide source consisting of ^{239}Pu, ^{241}Am, and ^{244}Cm, the measured alpha particle spectrum is presented in Figure 39.

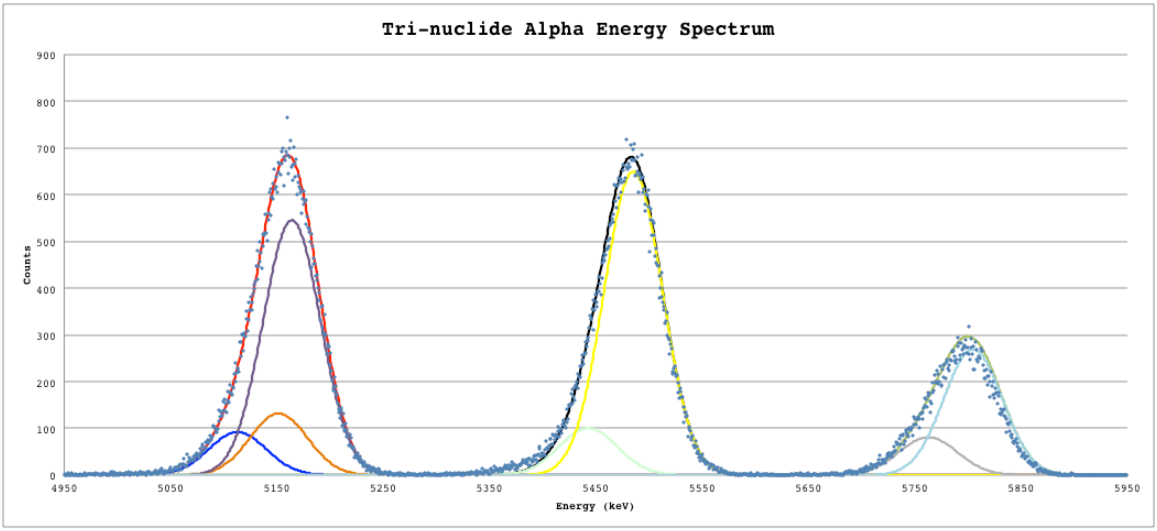

Figure 39 – Tri-nuclide alpha energy resolution spectrum

The fit lines labeled for each isotope give the overall fit that incorporates the contribution of different energy alphas that make up the overall distribution. This resolution was obtained from using a sum of the Gaussians for the main energy alphas that comprise each peak. Table 6 shows the alpha energies and their intensity that were used for this calculation. A single Gaussian width was used in the fits for the alphas from each nuclide. Next, a weighted average over all nuclides was used to obtain an overall energy resolution for the alpha particles.

Table 6 – Tri-nuclide alpha energies and intensity

Isotope	Energy (keV)	Intensity (%)
Pu-239	5156.59	70.77
	5144.3	17.11
	5105.5	11.94
Am-241	5485.56	84.8
	5442.8	13.1
Cm-244	5804.77	76.9
	5762.64	23.1

Each peak had a FWHM of 27 keV which yielded a resolution of 1.25%, 1.18%, and 1.11% for the Pu-239, Am-241, and Cm-244 peaks, respectively. The value obtained from the weighted average of the resolutions gave an overall alpha resolution of 1.18%.

This slight improvement in energy resolution is important in achieving the goal of this project, which is to obtain a mass resolution of <1 amu. The uncertainty of the mass can be found by:

$$\frac{\sigma_m}{m} = \sqrt{\left(\frac{\sigma_E}{E}\right)^2 + 2\left(\frac{\sigma_l}{l}\right)^2 + 2\left(\frac{\sigma_t}{t}\right)^2}$$

where m, E, l, and t correspond to the mass, energy, length of TOF path, and TOF measurement respectively. There is very little uncertainty associated with the length of the chamber and the time measured by the MCP detectors, which indicates that the majority of the uncertainty comes from the energy measurement obtained in the ionization chamber. Achieving an energy resolution of 1.18% for alpha particles leads us to believe that a resolution for the fission fragments should be on the order of 0.3%. This result is based on the statistical limit of energy resolution:

$$R = 2.35\frac{\sqrt{FW}}{\sqrt{E}}$$

where F is the Fano-factor, W is the average number of ion pairs produced from the deposition of the incident particle energy, and E is the energy deposited [Knoll 2010]. Fission fragments have on the order of 10 to 20 times the amount of energy as alpha particles. By taking a ratio of the square root of the energies a resolution of approximately 4 times smaller should be expected for fission fragments.

4.2 Ionization Chamber Δt

An extensive study was done on the ionization chamber Δt, which is the time difference between the induced pulse on the cathode and the induced pulse on the anode. Two methods were used to pick off the signal and evaluate the data. The first was to feed the cathode and anode signal directly to the CAEN desktop digitizer. The second was to feed both signals into a Model 715 PS Timing Discriminator then into an Ortec 467 Time to Pulse Height Converter (TPHC) that was then sent to the CAEN desktop digitizer. Details and timing results for both set-ups will be presented.

4.2.1 Electronics setup 1 for Δt

The electrode pulses may be fed into the CAEN digitizer. When a pulse is induced on either of the electrodes the data are stored in list mode format from the CAEN digitizer, a time stamp and the corresponding pulse height. A short timing condition can then be set to look at electrode pulses from what we hope are the same event, which gives the time of flight within the ionization chamber. This method was used when the system utilized a Mylar entrance window and P-10 detector gas. The following results are specific to these detector conditions. Measurements of alpha particles and fission fragments were made to investigate the Δt. Figure 40 shows a timing distribution obtained for ^{252}Cf.

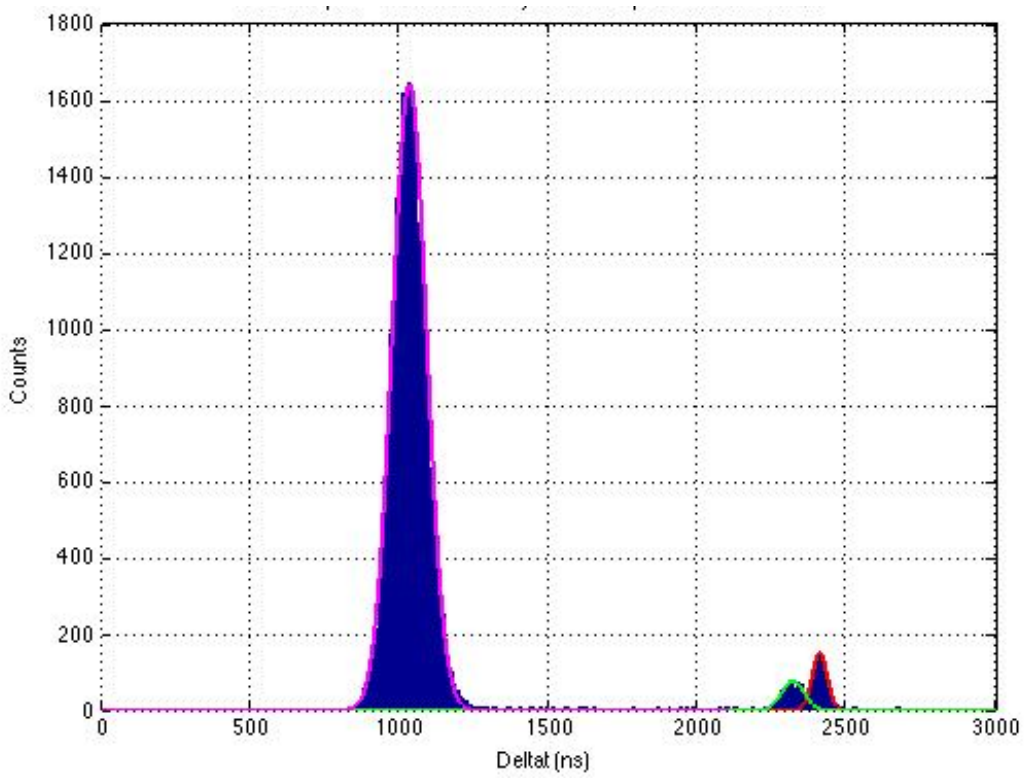

Figure 40 – ^{252}Cf alpha and fission fragment Δt timing distribution

Figure 40 shows that three peaks are obtained. The settings for this graph were optimized for alpha particles so little data is obtained for fission fragments; however, there is a clear difference in the timing measurement made for different energy particles. Figure 41 shows a timing distribution at settings more suitable for fission fragments. The narrower distribution for heavy fragments, which are stopping over a smaller range than the lighter fragments, is only about 50 ns wide. As the timing steps in the CAEN digitizer are 10 ns, a method to acquire Δt with smaller time steps was needed. This is discussed in the next section.

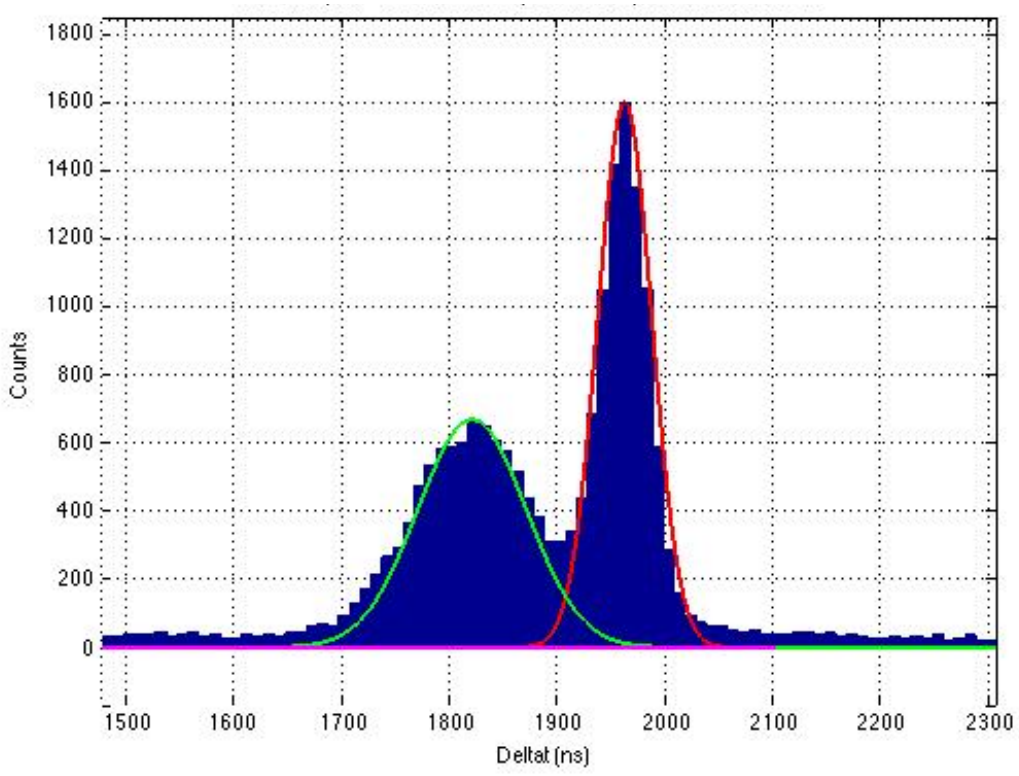

Figure 41 – ^{252}Cf fission fragment Δt timing distribution

A major component to the timing data is the pressure to which the chamber is filled. Figure 42 shows the timing difference measured at different pressures while keeping the reduced electric field constant.

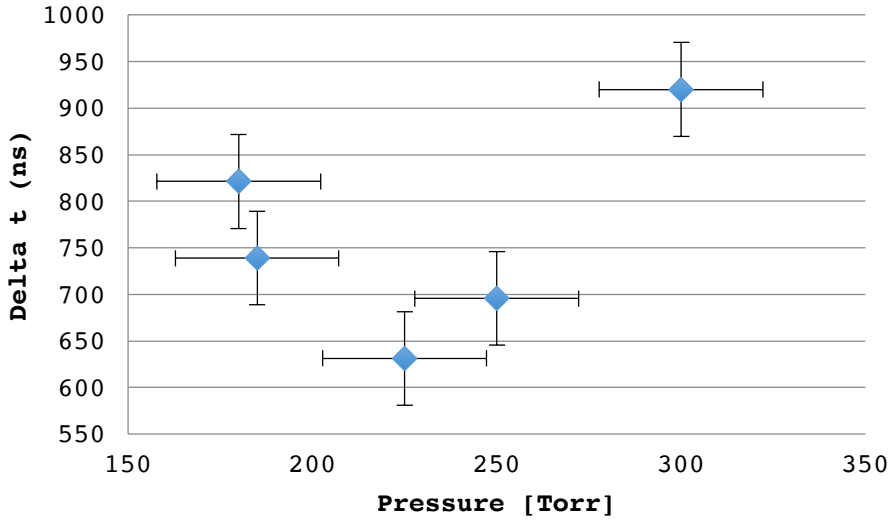

Figure 42 – ^{252}Cf alpha pressure vs. Δt for P-10 gas and 1.5 µm Mylar

This graph shows that a minimum Δt is obtained at 220 Torr, which is the pressure at which the alpha particles stop closest to the Frisch grid and therefore have the shortest time to reach the anode. For pressures higher than 220 Torr, the alpha particles are stopped further away from the Frisch grid which increases the Δt. For pressures lower than 220 Torr, the alpha particles begin to punch-through the detector. This means that there is not a high enough gas density to fully stop the particles and they pass through the active region chamber without fully depositing their energy, termed “punch-through," with the particle liberating electrons directly in the FG-A region. The larger Δt values for these presumed punch through points is not understood. A more in-depth look at punch-through will be presented in the next section.

4.2.2 Punch Through

During the investigation of the ionization chamber Δt, it was noticed that timing data, which in turn gives range, was not consistent with values obtained from SRIM using the difference in the raw cathode and anode signals. It appeared that there was an inherent system delay that needed to be accounted for. To understand and correct for this, punch-through of alpha particles was tested. Figure 43 shows the raw signals from the anode and cathode for the case when punch-through occurs and when the particle fully stops within the chamber. With punch-through, the particle liberates electrons directly in the FG-A region and so liberated electrons begin to drift at the same time in the C-FG and FG-A regions.

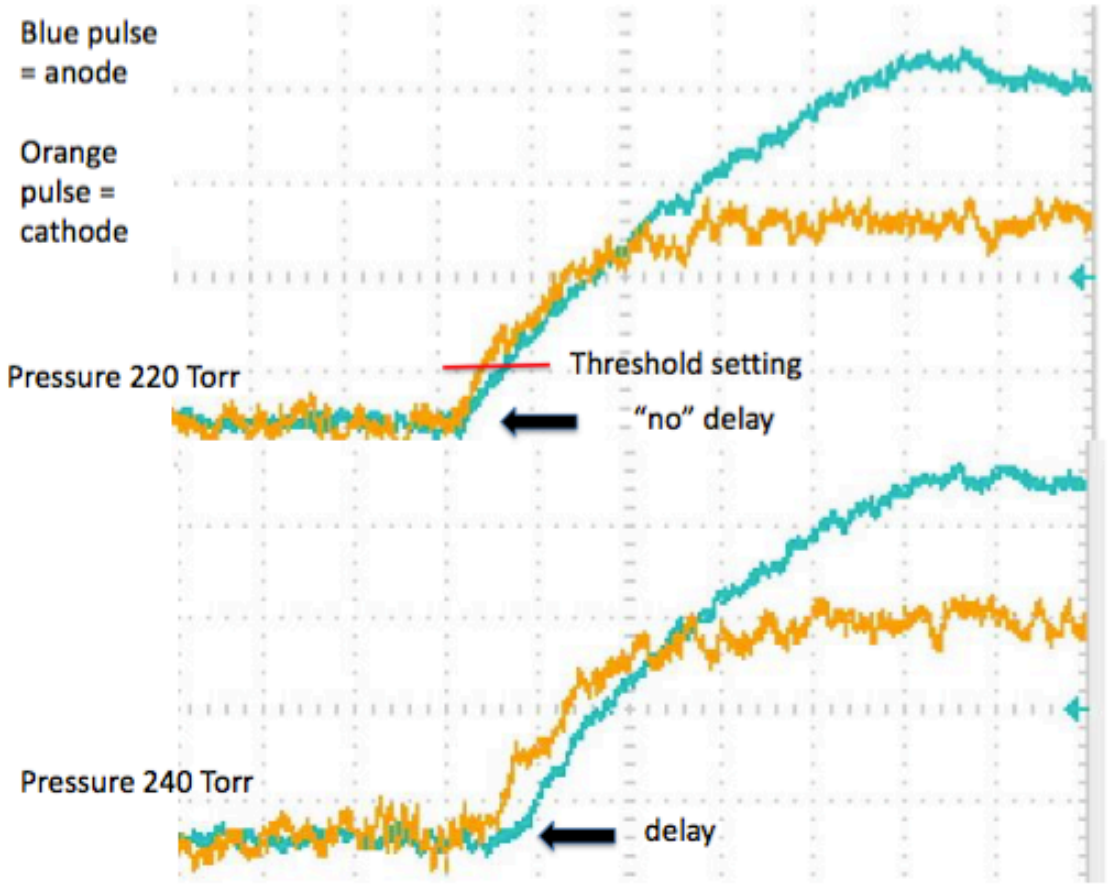

Figure 43 – Anode and cathode signals (top) with punch-through and (bottom) with the alpha particle stopping in the active region.

This shows that for a pressure of 220 Torr the cathode and anode signal appear to start at the same time, whereas for 240 Torr there is a clear delay between the two signals. This theoretically means that at punch-through there should be a zero time difference; however a time difference was still observed. This was due to the threshold settings used to pick off the two signals. From Figure 43 the red line shows the location where the signal was being read, which shows there is some inherent time difference due to the differences in the pulses. To correct for this, a minimum time difference needed to be found to adjust

for the inconsistent pick-off of the signals. Figure 44 gives the functional dependence used to find the minimum Δt.

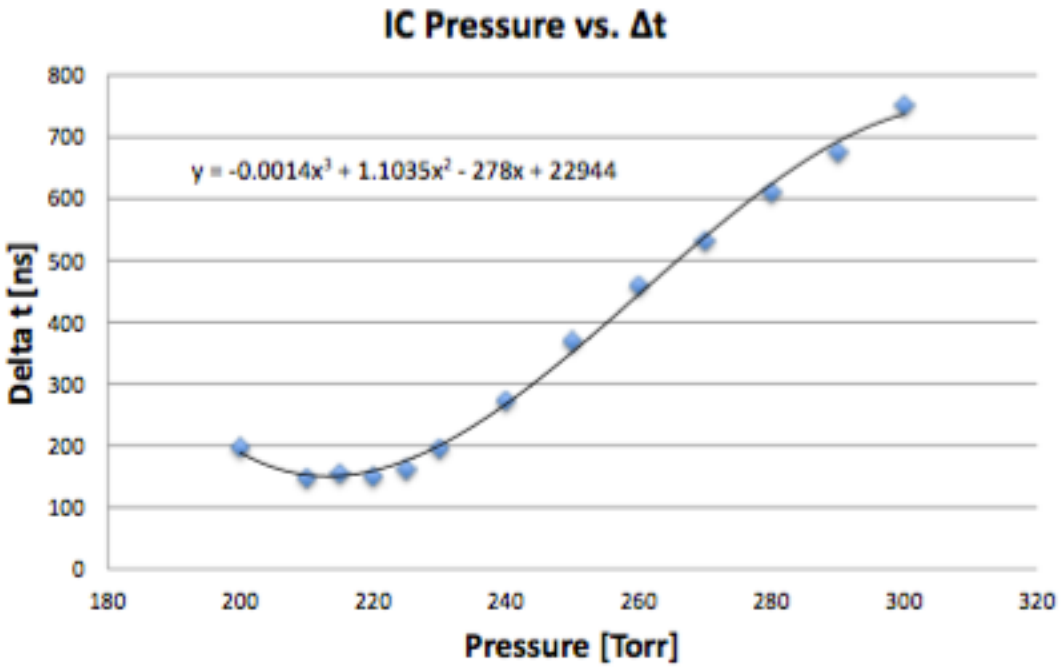

Figure 44 – "Zero" ionization chamber Δt

The derivative of this graph was taken and set equal to zero to return a minimum IC Δt of 154.2 ns, which then may be subtracted from Δt measurements for a corrected Δt value. The effects of this correction will be presented in the range portion of the results.

4.2.3 Electronics setup 2 for Δt

As stated previously a more precise measurement of the timing data was needed to obtain the desired information leading to atomic number determination. This led to the use of a timing discriminator and time to pulse height convertor (TPHC), along with isobutane

and a SiN window, to obtain the ionization chamber Δt. The analog timing pulses were fed into a discriminator, which produces square pulses. The square pulses are fed into the TPHC as start and stop signals and the TPHC outputs a pulse with height proportional to the timing difference. Since the CAEN digitizer is 14 bits for pulse heights, this allows for much better timing resolution than directly using the CAEN 10-ns clock. This allowed for a timing window of 0.25 ns/bin to be used to measure the time. Figure 45 shows the timing distribution obtained for ^{252}Cf fission fragments.

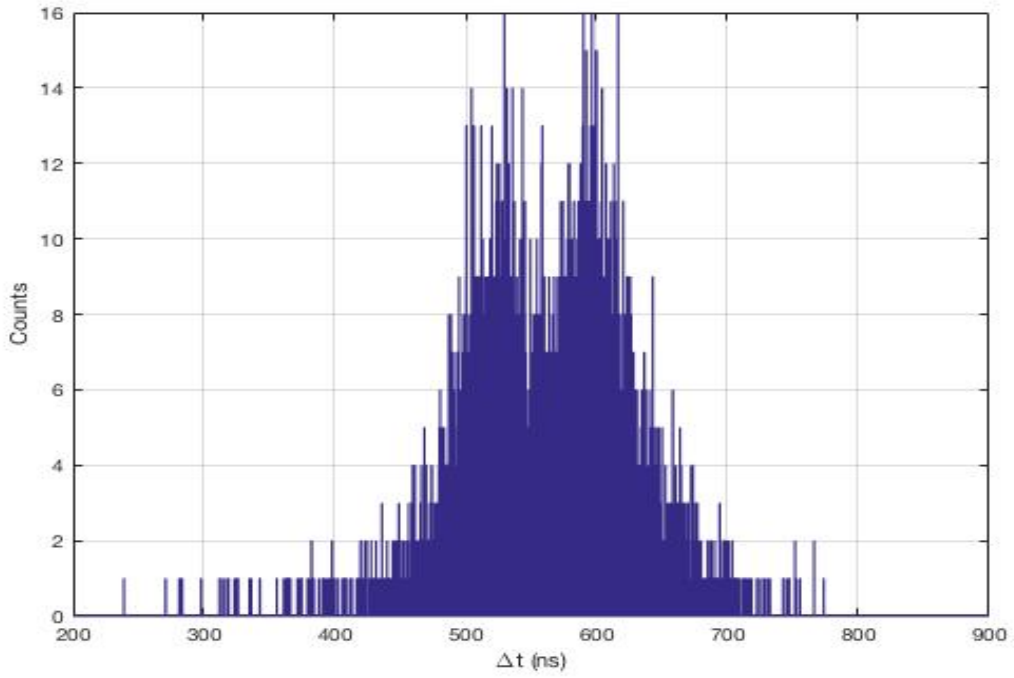

Figure 45 – ^{252}Cf fission fragment TPHC IC Δt

Several differences can be seen between Figures 45 and 41. First off is the symmetry between the fragment peaks in Figure 45, perhaps due to deeper penetration into the gas. The second is the narrower FWHM for both peaks, again possibly due to gas. In

addition, the entire spectrum has been shifted down. This is due to the stopping power of isobutane compared to P-10. Using the electronics timing setup 2 enabled the more precise binning seen.

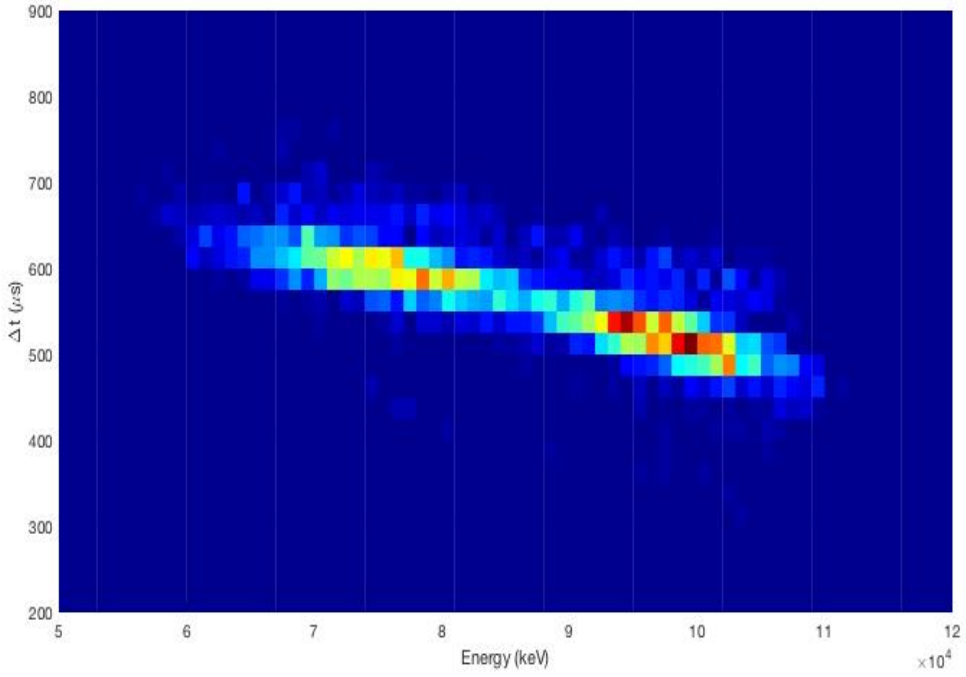

Figure 46– IC Δt vs. fission fragment energy for ^{252}Cf

The IC Δt data, along with the energy measurements, is critical to obtaining atomic number information. Figure 46 shows the relationship between particle energy and the Δt measured within the chamber. The two groupings demonstrate that higher energy, low mass particles penetrate the chamber deeper than lower energy, high mass particles. The figure also shows that there is a spread to each group. This indicates that for the same energy there are multiple Δt values. This is due to the fact that there is a wide spread in masses that can have the same kinetic energy and therefore similar Δt.

Again pressure and electric fields have a major impact on the Δt measured by the ionization chamber. Figure 47 shows the effect the pressure has on the Δt measured.

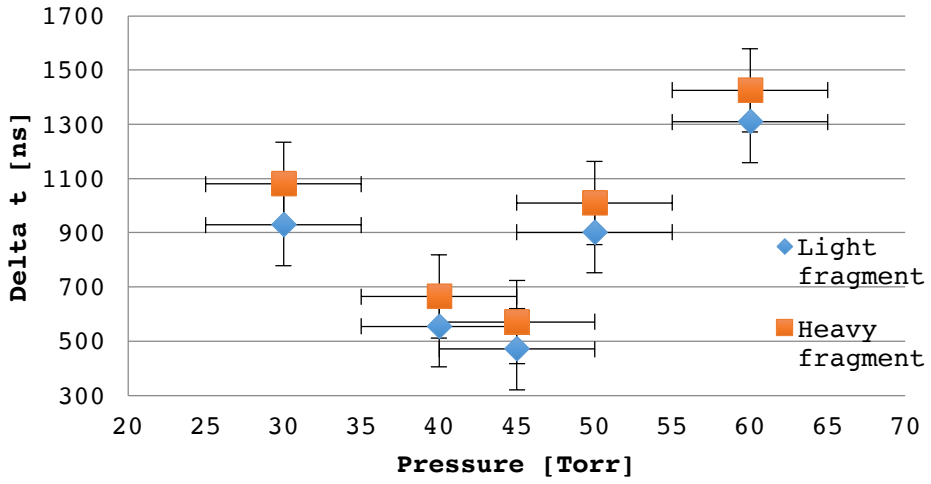

Figure 47 – IC Δt for ^{252}Cf fission fragments with constant field ratio

Figure 47 follows the same trend as Figure 42. For pressures below 40 Torr of isobutane a larger percentage of the fission products probably punch through the chamber, though the Δt values are larger. For pressures above 40 Torr the stopping power of the gas is increased and stops the products further from the Frisch gird, increasing the drift time of the electrons to the anode.

Figure 48 shows the effect the reduced electric field has on the IC Δt. Despite the lack of data points this figure clearly shows that the IC Δt is affected by the field strengths applied within the ionization chamber. This effect is due to the drift velocity of the electrons as they are accelerated by the electric fields. More information on the drift velocity of the electrons is presented in the section on range results.

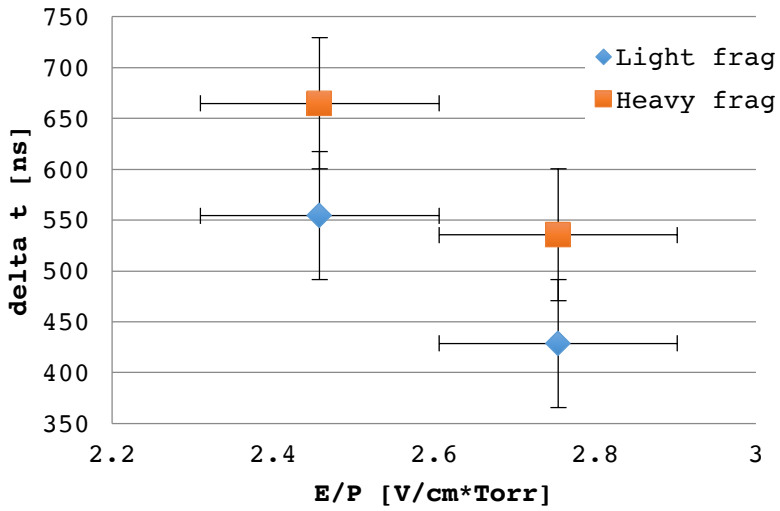

Figure 48 – ^{252}Cf fission fragment Δt vs. reduced electric field at 40 Torr isobutane

4.3. Range Calculation

4.3.1 Range Calculations using Mylar and P-10

The results presented for this section correspond to a chamber set-up consisting of a 1.5 μm Mylar entrance window and P-10 gas. For these calculations the drift velocity was held at a constant value due to the ability to maintain a reduced electric field that yielded the maximum drift velocity for the materials chosen. Range was extracted from ionization chamber timing data using the electron drift velocity and the equations already presented.

The drift velocity in gas mixtures is a function of the mixture, so a value was determined for the P-10 argon/methane mixture. In the case of P-10, the methane comprises 10% of the total mixture. From Figure 49 this concentration corresponds to a maximum

drift velocity of 5.2×10^6 cm/s. This value was used as the drift velocity for the following range calculations along with a constant reduced electric field value of 0.23 V/cm*Torr.

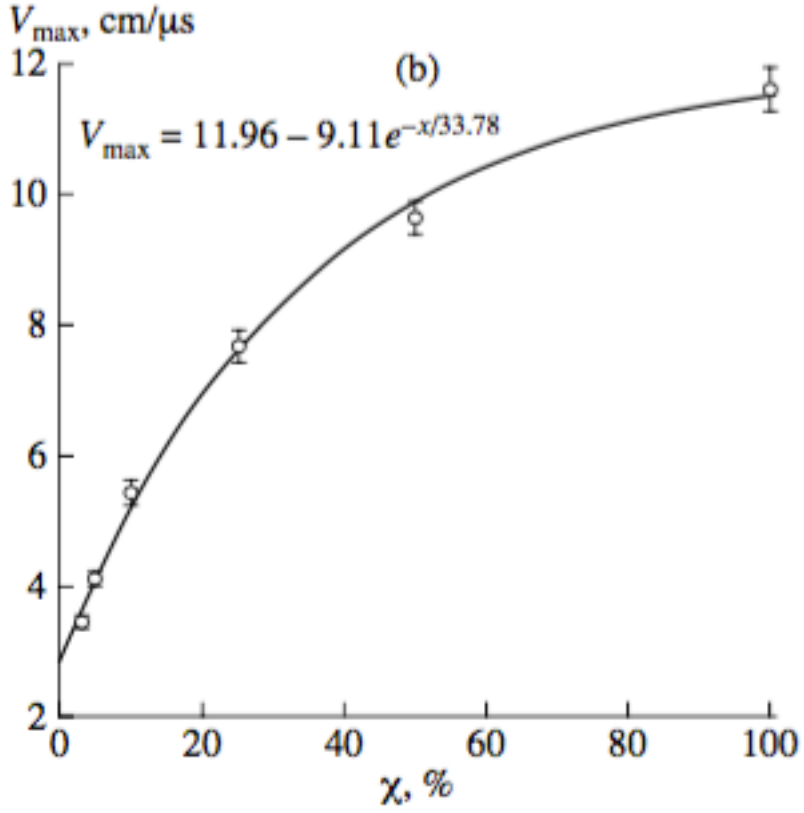

Figure 49 – Maximum electron drift velocity for percentage of methane/argon mixtures [Khryachkov 2003]

Range measurements were performed using the extracted drift velocity. Figure 50 shows the average range of the ^{252}Cf alpha into 400 Torr P-10 using the values previously stated. Table 7 gives the calculated range of the ^{252}Cf alpha at various pressures with a corrected range based off the minimum Δt discussed in the previous section and a comparison to SRIM calculations.

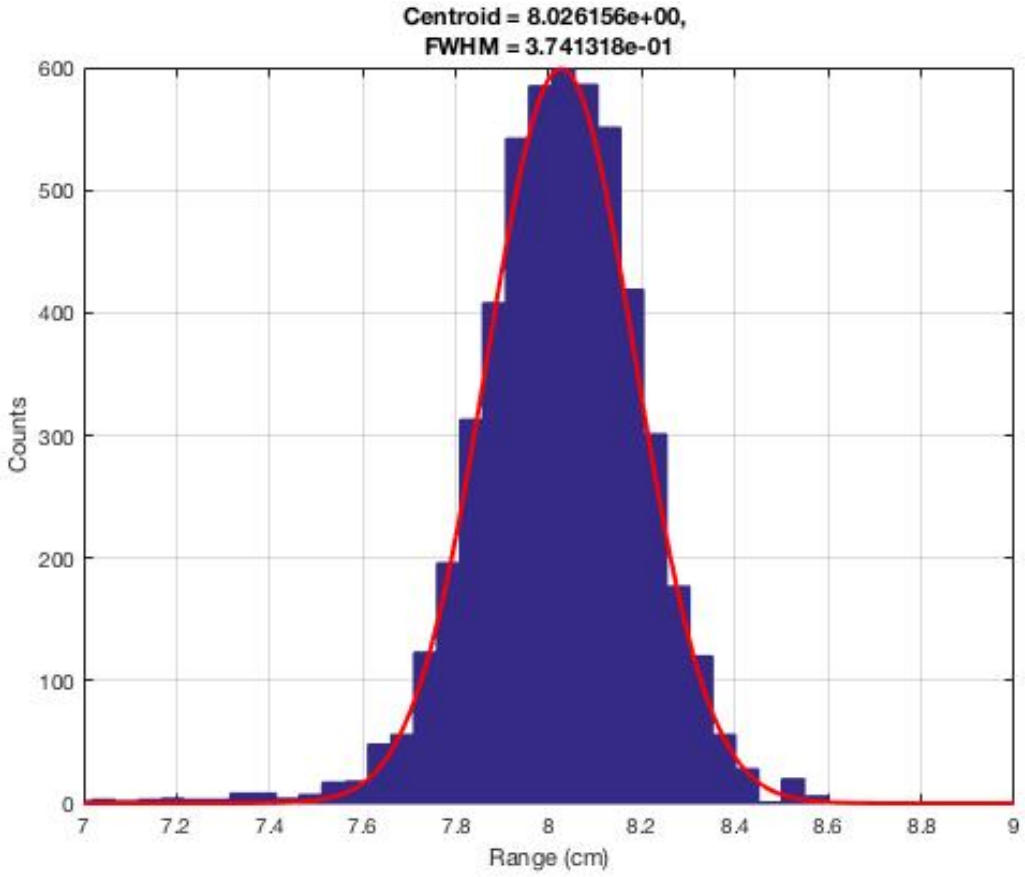

Figure 50 – ^{252}Cf alpha range in 400 Torr P-10 gas

Table 7 – ^{252}Cf alpha ranges for P-10 gas

Cf-252 alpha range			
Pressure	Calculated (cm)	FWHM	SRIM (cm)
260	9.77	0.66	15.0
340	9.14	0.46	11.6
400	8.03	0.37	9.75

Table 7 shows that the calculated range data is greatly underestimated from the values predicted by SRIM. This is thought to be due to an underestimation in the energy

straggling calculated by SRIM. It is believed that much more energy is lost as the particle passes through the Mylar window and that there is a discrepancy between how SRIM treats the charge states of particles that contributes to these differences.

4.3.2 Range Calculations – SiN and Isobutane

The improvements in the drift time of the electrons have been stated in previous sections of the results. The increased precision in the timing data obtained from the TPHC, SiN, and isobutane configuration yields range results much more consistent with values predicted from SRIM. Again, a major factor is the determination of the drift velocity. Little data is available for electron drift velocity in isobutane and data that is available only provides a small range of values. In order to obtain the most accurate drift velocity for range calculations for the pressure range used, a functional dependence of the reduced electric field versus drift velocity was needed. Figure 28 - drift velocity as a function of field for several pressures - was examined to extract drift velocity values as a function of E/P to produce functions to work with, are presented in Figures 51 and 52.

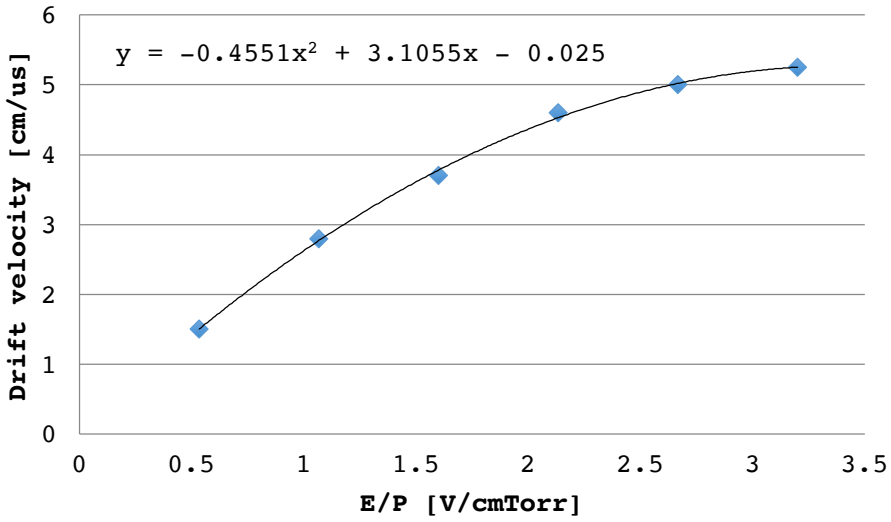

Figure 51 – Electron drift velocity function for isobutane at 37.5 Torr

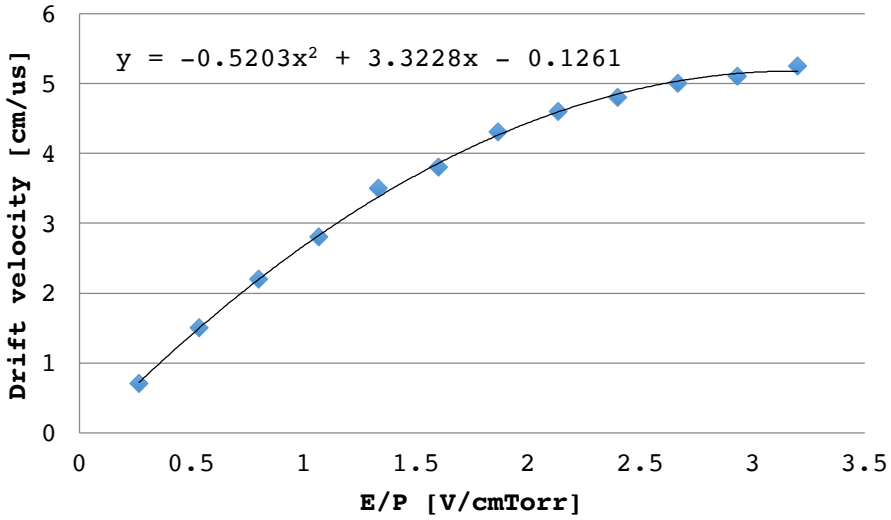

Figure 52 – Electron drift velocity function for isobutane at 75 Torr

These functions were implemented into the MATLAB code to ensure that a more realistic value for the drift velocity was obtained. A constant maximum value could not be

assumed due to the inability of the physical system to achieve the desired E/P values resulting from high-voltage breakdown and shorting issues, which were later resolved. Figure 53 shows the calculated range implementing the functions for drift velocity versus reduced electric field. The first spectrum gives the range corresponding to a drift velocity of 4.3956×10^6 cm/s and the second spectrum corresponding to a drift velocity of 4.3215×10^6 cm/s. Using the average distance of the high-energy peak (right peak) as a reference, the distances traveled are 10.8 cm and 10.9 cm respectively. This shows that there is approximately a 1 mm change in the range calculated by using the two functions to obtain the drift velocity. Since this difference is well within the error of the distribution itself the function from the 75 Torr graph was used for this analysis.

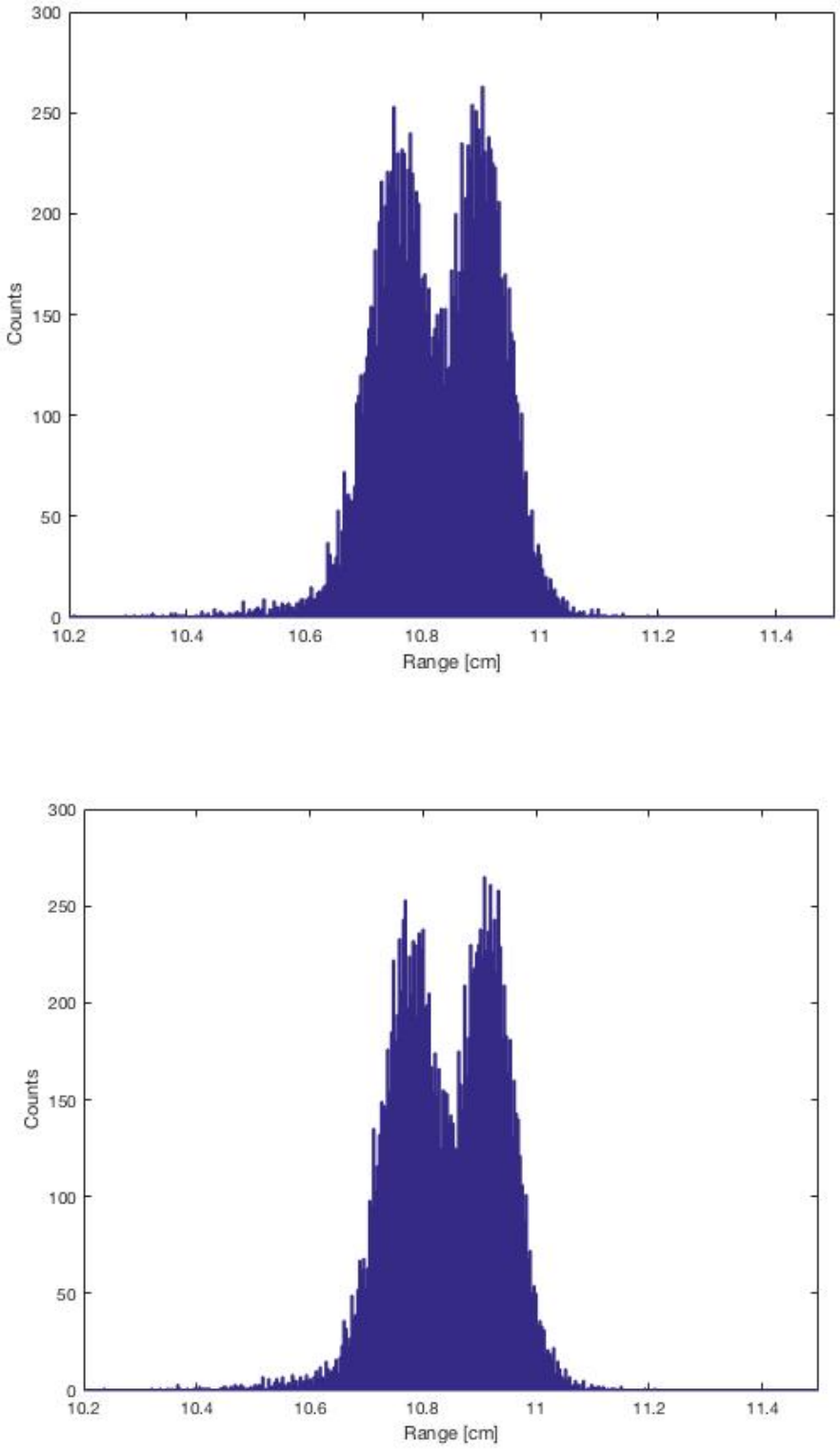

Figure 53 – ^{252}Cf fission fragment range distributions found with extracted drift velocities of 4.4x10^{6} cm/s (top) and 4.3x10^{6} cm/s (bottom)

Figure 54 shows the range of the ^{252}Cf light fission product as a function of the gas pressure of the chamber. This shows that at higher pressures there is a higher gas density and therefore more stopping power that shortens the range of the particles. The parabolic shape of this graph mirrors the opposite curvature parabolic shape of the timing plots. We expect punch through at lower pressures, though that would decrease the IC timing difference and translate to a longer range. The opposite effect observed at low pressure is not understood. Table 8 gives a comparison of the ranges calculated and those obtained from SRIM calculations.

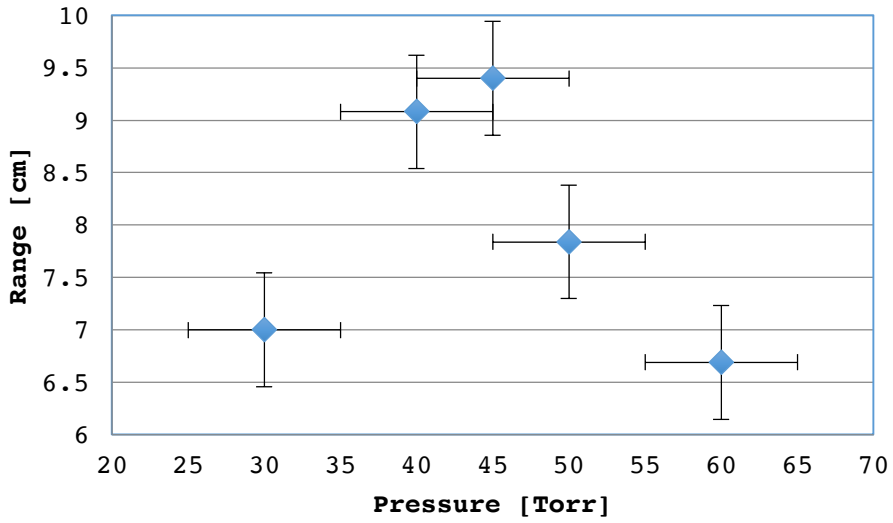

Figure 54 – ^{252}Cf light fission product range vs. IC pressure with constant field ratio

Table 8 – Range comparison for ^{252}Cf light fragments

^{252}Cf Light Fragment Range		
Pressure [Torr]	Calculated Range [cm]	SRIM Range [cm]
30	7.00	n/a
40	9.08	12.5
45	9.40	12.3
50	7.84	11.4
60	6.69	9.56

This table shows that there is still some discrepancy between the range calculated from the data obtained and those predicted by SRIM, even other than the unexplained results at lower pressures. One cause of these differences could be the properties SRIM uses for isobutane. The purity of the gas used for this experiment is 99.995% as opposed to the 100% purity in calculations, and it is unclear as to how this difference affects the physical properties used by SRIM though that would be expected to be minimal. Another cause could be the way in which SRIM handles the charge of the fission fragments. It is unclear as to what charge state the fission products are in when they enter the ionization chamber and the changing equilibrium states as they slow. This uncertainty can have major implications as to how the particle interacts within the gas and the electric fields. These variations can lead to events that cause the products to have shorter ranges than predicted

by SRIM. For example, at 30 Torr a range was measured within the active region of the IC, whereas SRIM predicts that all particles punch through.

An energy versus range plot for a pressure of 50 Torr is given in Figure 55. This figure is a mirror image of Figure 46 using the Δt to range conversion equation. It shows that higher-energy particles travel a further distance into the ionization chamber. This result is expected since these particles are of lighter mass and lower Z and start with a higher kinetic energy, and thus have a lower stopping power in the gas. The longer range is consistent with having a shorter Δt due to the particle depositing its energy closer to the Frisch grid, meaning the electrons they create are collected faster under the same field strength. It is also noted from this figure that there are again two distinguishable groups of fission products. The spread in the range for the same energy is attributed to multiple nuclides that can have that kinetic energy; it is therefore the mass or charge that yields different ranges at each energy. With greater statistics we intend to examine the spread of range for specific mass and E values to examine range differences due to Z.

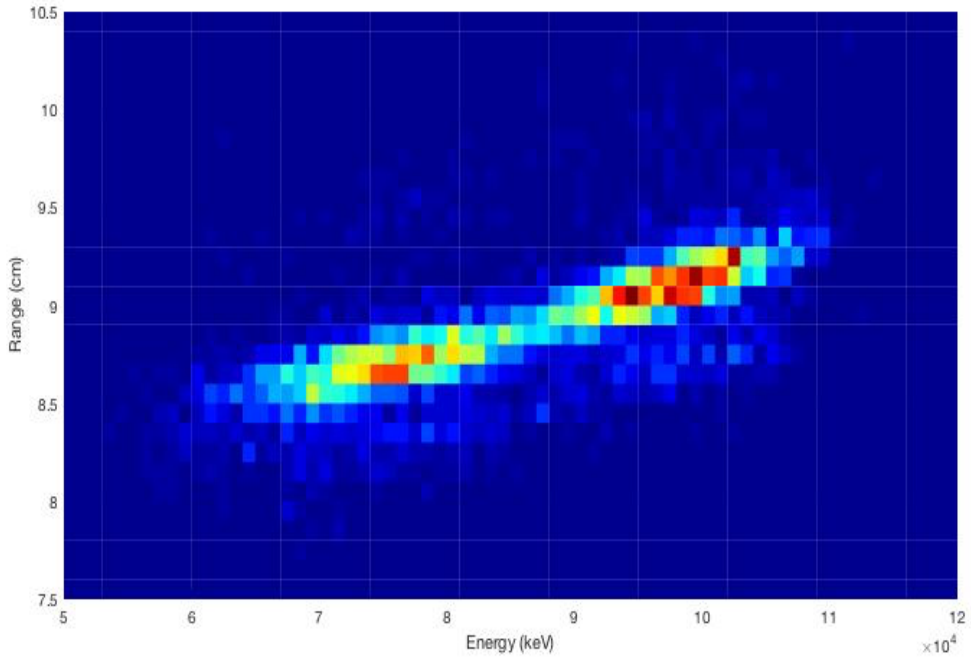

Figure 55 – ^{252}Cf fission product range vs. energy

5 Conclusions and Future Work

5.1 Conclusions

A successful implementation of the SiN window and isobutane gas produced more precise timing data that in turn yielded more favorable range calculations than those obtained from the Mylar and P-10 set-up. Alpha energy resolution was also shown to improve slightly from 1.33% with Mylar and P-10 to 1.18% with SiN and isobutane, with a much greater improvement expected for fission fragments. These improvements will play a major role in achieving a mass resolution of less than 1 amu and eventually Z determination for each incident particle.

The issue of electrical breakdown was a very limiting factor over the course of this work. It significantly contributed to the inability to achieve the desired reduced electric field that we hope gives the most consistent timing data. It also was a very timely issue causing a large period of time when no data was being taken. Though the breakdown issues were solved, this took several months and took time away from data acquisition. Many of the results presented would be more conclusive and interpretable if more points were taken without having this issue of breakdown.

5.2 Future Work

5.2.1 Window Redesign

The current design of the entrance window to the ionization chamber greatly restricts the count rate of data taken. The small size, 1 cm x 1 cm, significantly reduces the number of particles detected. To increase the statistics gathered for each measurement,

a new window design has been proposed. Figure 56 shows a schematic of the next iteration of the entrance window. This configuration will include five 1 cm x 1 cm SiN windows in a cross formation. This should greatly increase the acceptance angle of the ionization chamber leading to higher statistics.

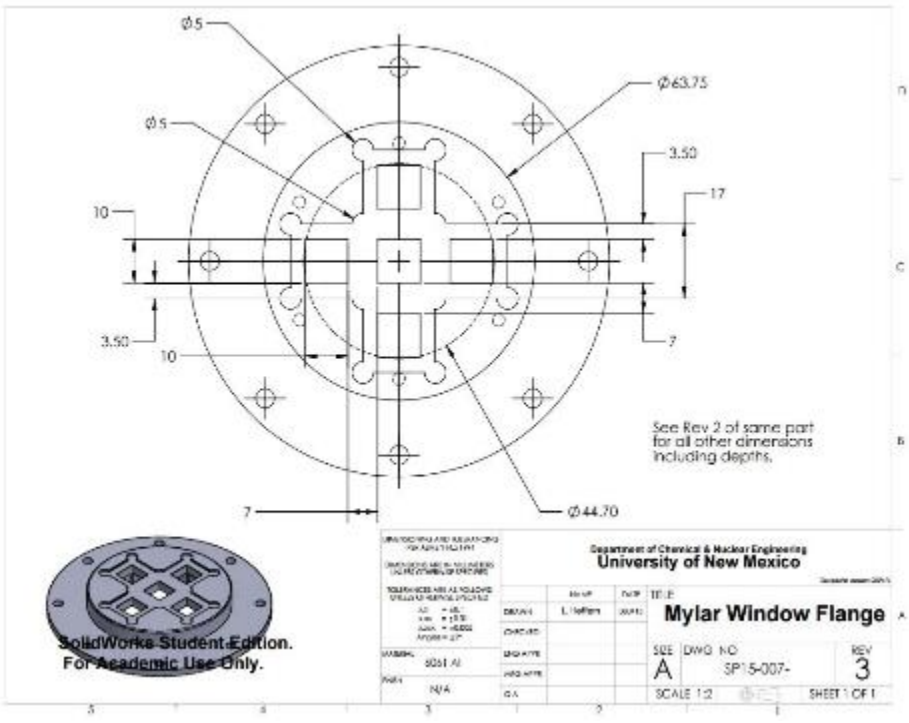

Figure 56 – New IC entrance window design

5.2.2 Atomic Charge (Z) Determination

A major goal of this detector is to produce an event-by-event measurement of the atomic charge of the fission products. This process will include a correlated measurement

of the products energy, mass, and range. Preliminary determination of Z will include the use of the Bethe-Bloch formula that is again stated below

$$-\frac{dE}{dx} = \frac{4\pi k_0^2 z^2 e^4 n}{mc^2\beta^2}\left[ln\frac{2mc^2\beta^2}{I(1-\beta^2)} - \beta^2 \right]$$

One issue that arises in applying this equation is that it is less straightforward with heavy particles [Fulbright 1979]. This is due to the fact that heavy particles exhibit complications due to variations in their effective atomic charge with the velocity of the particle due to charge exchange. As the Bethe equation deals with Coulomb interactions, it doesn't account for atomic scattering energy loss, which becomes increasingly important toward the end of the particles track [Fulbright 1979]. To avoid this issue, an empirical equation given by Tyukavkin will also be investigated. The equation below gives the relationship between range, mass, energy, and Z as determined by Tyukavkin

$$R = \beta\sqrt{EM}Z^{-2/3}$$

In this relationship the β term is a corrective factor that is found using an iterative process. This parameter, along with Z, have to be determined using experimental data and should be investigated.

Appendices

Appendix A

Gas Flow Controls for Isobutane

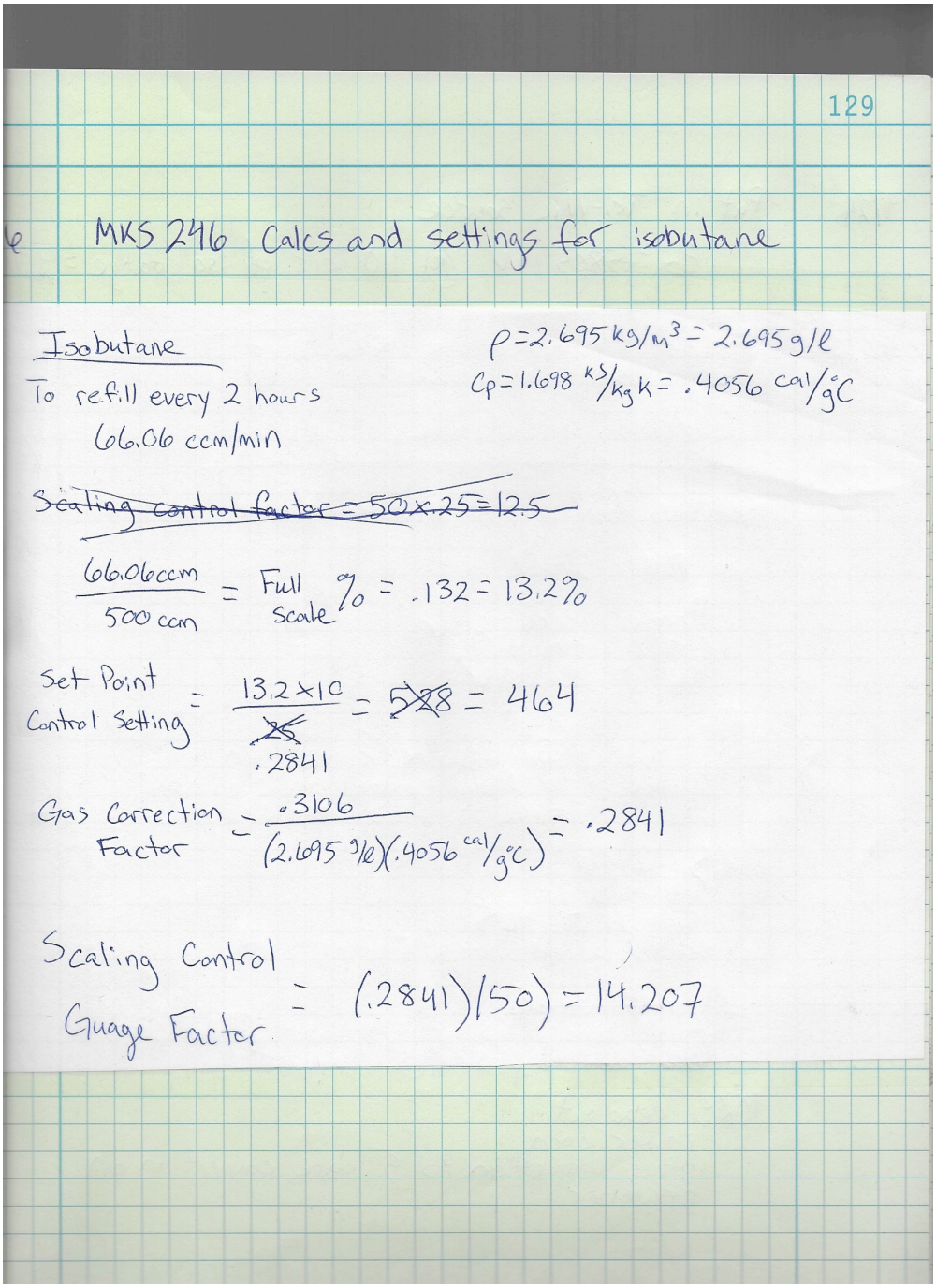

Figure 57 – Pressure control settings for isobutane

Appendix B

MATLAB Analysis Code

```
% Jimbos program for mass/timing/range/Z determination
clear;
clc;
ch1tmp = load('~/Desktop/IC Stuff/Active Cathode Cf and Pu
runs/Jun14_2016FF_fullmassrun_C2620_A525_iso_70torr_002_ls_1.dat');
ch1tmp;
ch2tmp = load('~/Desktop/IC Stuff/Active Cathode Cf and Pu
runs/Jun14_2016FF_fullmassrun_C2620_A525_iso_70torr_002_ls_2.dat');
ch2tmp;
ch0tmp = load('~/Desktop/IC Stuff/Active Cathode Cf and Pu
runs/Jun14_2016FF_fullmassrun_C2620_A525_iso_70torr_002_ls_3.dat');
ch0tmp;
ch_ar_tmp = load('~/Desktop/IC Stuff/Active Cathode Cf and Pu
runs/Jun14_2016FF_fullmassrun_C2620_A525_iso_70torr_002_ls_2.dat');
ch_ar_tmp;
%Next section - only load if using data that was taken when using CFD
%ch3tmp = load('~/Desktop/IC Stuff/Active Cathode Cf and Pu
runs/050715Cf252tests1_5ummylarGoodReswAC_009_ls_3.dat');
%ch3tmp;

[N,M] = size(ch1tmp);
[S,T] = size(ch2tmp);
[U,V] = size(ch0tmp);
[W,X] = size(ch_ar_tmp);

if (N>S)
    ch2 = load('~/Desktop/IC Stuff/Active Cathode Cf and Pu
runs/Jun14_2016FF_fullmassrun_C2620_A525_iso_70torr_002_ls_2.dat');
    ch2 = [ch1;zeros(N-S,T)];
    ch1 = ch1tmp;
else
    ch1 = load('~/Desktop/IC Stuff/Active Cathode Cf and Pu
runs/Jun14_2016FF_fullmassrun_C2620_A525_iso_70torr_002_ls_1.dat');
    ch1 = [ch1;zeros(S-N,T)];
    ch2 = ch2tmp;
end
if (U>W)
    ch_ar = load('~/Desktop/IC Stuff/Active Cathode Cf and Pu
runs/Jun14_2016FF_fullmassrun_C2620_A525_iso_70torr_002_ls_2.dat');
    ch_ar = [ch0;zeros(U-W,X)];
    ch0 = ch0tmp;
else
    ch0 = load('~/Desktop/IC Stuff/Active Cathode Cf and Pu
runs/Jun14_2016FF_fullmassrun_C2620_A525_iso_70torr_002_ls_3.dat');
    ch0 = [ch0;zeros(W-U,X)];
    ch_ar = ch_ar_tmp;
end

%%
%Assigns tof, anode pulse, and IC TPH pulse to matrix
m = length(ch1);
data_E_tof_delt = [ch1(1:m,1) ch1(1:m,2) ch2(1:m,1) ch2(1:m,2)
```

```
ch0(1:m,1) ch0(1:m,2)];
%%
fignum = 1;
%Looks at raw data of TOF and anode pulse to determine peaks for
%calibration and mass calculations
figure(fignum)
fignum - fignum+1;
subplot(1,2,1)
hist(ch1(:,2),1000)
title('Ion Chamber')
xlabel('Channel #')
ylabel('Counts')
grid()
subplot(1,2,2)
hist(ch2(:,2),5000)
title('TOF')
xlabel('Channel #')
ylabel('Counts')
grid()
%%
hist(ch0(:,2),1000)
%%
% Sorts through anode & TOF for correlated data points
tic
j = data_E_tof_delt(:,3);
d = data_E_tof_delt(:,1);
c = data_E_tof_delt(:,5);

k=0;
A=[];
n=1;
for i = (1:length(d));
    k=k+1;
    for h = (n:length(j));
        if(abs(j(h)-d(i))<300);
            A(i,:) =
[data_E_tof_delt(i,1),data_E_tof_delt(i,2),data_E_tof_delt(h,3),data_E_
tof_delt(h,4)];
            break
        end
    end
    if (k == 100)
        k = 0;
        (i/length(d))*100
    end
end
fprintf('Complete 1\n')

loc1 = find(A(:,1)==0);
A(loc1,:) = [];
toc
%%

heavy_frag_E = input('Centroid channel of heavy fragment energy
peak:');
light_frag_E = input('Centroid channel of light fragment energy
peak:');
```

```
light_frag_t = input('Centroid channel of light fragment timing
peak:');
heavy_frag_t = input('Centroid channel of heavy fragment timing
peak:');

%%
%Energy calibration parameters
x = [heavy_frag_E light_frag_E];
hf1eng = 67690; %Post neutron emission in keV
lf1eng = 90818; %Post neutron emission in keV
% Above values are E-loss corrected from SRIM calcs
y = [hf1eng lf1eng];
% Applying the fit
p = polyfit (x,y,1);
yfit = polyval(p,x);
energy = A;
energy(:,2) = p(1)*A(:,2) + p(2); %first order fit for FF only
countseng = length(data_E_tof_delt);
counts2eng = length(energy(:,2));

%Timing calibration parameters
x2 = [light_frag_t heavy_frag_t];
lf1time = 3.7386e-08; % seconds
hf1time = 4.95398e-08; % seconds
y2 = [lf1time hf1time];
% Applying the fit
p2 = polyfit(x2,y2,1);
y2fit = polyval(p2,x2);
timing = [A];
timing (:,4) = p2(1)*A(:,4) + p2(2); %first order fit for timing
countstime = length(data_E_tof_delt);
counts2time = length(timing(:,4));

% Applying energy equation to obtian mass distribution
% E = (1/2)mv^2 ----> 2E/(v^2) = m ---> 2E*(dT/dX)^2 = m

%corrected values
KE = energy(:,2); % keV
dT = timing(:,4); % seconds
dX = 0.5; % meters
v = dX./dT;

%% Timing calibration
x3 = [4255 15290];
y3 = [250 1000];

p3=polyfit(x3,y3,1);
y3fit = polyval(p3,x3);
time_ic_raw = [data_E_tof_delt(:,5), data_E_tof_delt(:,6)];
time_ic_raw(:,2) = p3(1).*time_ic_raw(:,2)+p3(2);

IC_time = [time_ic_raw];
%% Energy Add Back 3rd order fit from SRIM data (Full Frag Set Cf252)
C11 = 2.815876414010E+26;
C22 = 4.280773916360E+19;
C33 = 2.081971364596E+12;
```

```
C44 = 2.525396791487E+04;
KEadd = KE;
KEadd = KE + C11.*timing(:,4).^3-C22.*timing(:,4).^2 +
C33.*timing(:,4).^1 - C44;
KEadd_t = [A(:,3),KEadd];
%% Uncorrected mass
mass = 2.*KE./(v.^2); % in keVs^2/m^2
amu = 9.64853365*10^10; %conversion factor --> to amu
mass_un = mass*amu;
%% Corrected mass
mass_c = (2.*KEadd./(v.^2))*amu;
mass_c_t = [A(:,3),mass_c];
%% Run to check peak symmetry
countslight = 0;
countsheavy = 0;
for i2 = (1:length(mass_un));
    if (mass_un(i2) >= 80 && mass_un(i2) <= 120);
        countslight = countslight + 1;
    end
    if (mass_un(i2) >= 120 && mass_un(i2) <= 200);
        countsheavy = countsheavy + 1;
    end
end

countslight;
countsheavy;
%% Plotting the calibration fits for verification purposes.
fignum = 1;
figure(fignum);
fignum = fignum+1;
subplot(1,2,1)
scatter(x,y)
title('Ion Chamber Calibration')
xlabel('Channel #')
ylabel('Energy [keV]')
grid()
hold on
plot(x,yfit)
hold off

subplot(1,2,2)
scatter(x2,y2)
title('TOF Calibration')
xlabel('Channel #')
ylabel('Time [s]')
grid()
hold on
plot(x2, y2fit)
hold off
%% Plot calibrated data
figure(fignum)
fignum = fignum+1;
subplot(2,2,1)
hist(energy(:,2),2000)
title('KE Initial Calibration')
xlabel('Energy [keV]')
ylabel('Counts')
grid()
```

```
subplot(2,2,2)
hist(energy(:,2),75)
title('IC Calibrated (FF)')
xlim([40000,120000])
xlabel('Energy [keV]')
ylabel('Counts')
grid()

subplot(2,2,3)
hist(timing(:,4),2000)
title('TOF Calibrated')
xlabel('Time (s)')
ylabel('Counts')
grid()

subplot(2,2,4)
hist(timing(:,4),2000)
title('TOF Calibrated (FF)')
xlim([3.3e-8,6.5e-8])
xlabel('Time (s)')
ylabel('Counts')
grid()
%% Various "final" energy corrected plots (Mass, KE vs. TOF, Mass vs.
KE, ect...)
fignum = 15;
figure(fignum)
fignum = fignum+1;

% FF ROI
subplot (2,2,1)
edges = [0:.5:20000];
hist(mass_c,edges)
xlim([66,180])
xlabel('Mass (amu)')
ylabel('Counts')
title('Cf-252 spf E Corrected Mass Distribution')
grid()

%KE vs TOF
subplot(2,2,2)
scatter(KEadd(:),timing(:,4),1)
title('KE (corrected) vs. TOF')
xlabel('KE [keV]')
ylim([0,9e-8])
ylabel('TOF [s]')
grid()
hold on
syms x;
y = 2.577E-18*x.^2-9.770E-13*x + 1.113E-07;
ezplot(y,[5e4,12e4]);
title('KE (corrected) vs. TOF')
xlabel('KE [keV]')
xlim([4e4,12e4])

%Mass vs TOF
subplot(2,2,3)
```

```
scatter(mass_c(:),timing(:,4),1)
title('Mass (corrected) vs. TOF')
xlim([60,180])
xlabel('Mass [amu]')
ylim([2e-8,7e-8])
ylabel('TOF [s]')
grid()

%Mass vs KE
subplot(2,2,4)
scatter(mass_c(:),KEadd(:),1)
title('Mass (corrected) vs. KE (corrected)')
xlim([60,180])
ylim([4e4,12e4])
grid()
%% Starting Range calculations
%j = data_E_tof_delt(:,3); tof
%d = data_E_tof_delt(:,1); anode
%c = data_E_tof_delt(:,5); TPH

%[N,M] = size(ch1tmp);
% [S,T] = size(ch2tmp);
% [U,V] = size(ch0tmp);
% [W,X] = size(ch_ar_tmp);
%
% if (N>S)
%     ch2 = load('~/Desktop/IC Stuff/Active Cathode Cf and Pu
runs/Jun12016FF_fullmassrun_C3000_A600_iso_80torr_022_ls_2.dat');
%     ch2 = [ch1;zeros(N-S,T)];
%     ch1 = ch1tmp;
% else
%     ch1 = load('~/Desktop/IC Stuff/Active Cathode Cf and Pu
runs/Jun12016FF_fullmassrun_C3000_A600_iso_80torr_022_ls_1.dat');
%     ch1 = [ch1;zeros(S-N,T)];
%     ch2 = ch2tmp;
% end
%tph_temp = [data_E_tof_delt(:,5),data_E_tof_delt(:,6)];
%KE_temp = KEadd_t;



a = [IC_time(:,1),IC_time(:,2)];
b = KEadd_t;
f = mass_c_t;

[O,P]= size(a);
[Q,R]= size(b);
[B,D]= size(f);

if (O>Q)
    b1 = b;
     b1 = [b;zeros(O-Q,R)];
     a1 = a;
end

if (O>B)
    f1 = f;
```

```
    f1 = [f;zeros(O-B,D)];
    a2 = a;
end

IC_E = b1;
tph = a1;
mass = f1;


%%
tic
shape = 300

k3 = 0
C = []
z = length(tph);
for o = (1:z);
    k3 = k3+1;
    for e = (n:length(IC_E));
        tph_ICE = tph(o,1)-IC_E(e,1);
        if(abs(tph_ICE)<shape);
            sorteddata(o,:) = [tph(o,1),tph(o,2),IC_E(e,1),IC_E(e,2)];
            break
        end
    end
    if (k3 == 100)
        k3 = 0;
        (o/z)*100
    end
end

loc4 = find(sorteddata(:,1) == 0);
sorteddata(loc4,:) = [];

k4 = 0;
for o2 = (1:z);
    k4 = k4+1;
    for ee = (n:length(mass))
        tph_mass = tph(o2,1)-mass(ee,1);
        if(abs(tph_mass)<shape)
            sort_tph_mass(o2,:) =
[tph(o2,1),tph(o2,2),mass(ee,1),mass(ee,2)];
            break
        end
    end
end


loc5 = find(sort_tph_mass(:,1) == 0);
sort_tph_mass(loc5,:) = [];

toc
fprintf('Complete 2\n')

%%
peaks = sorteddata(:,4);
```

```
tph_time_energy = sorteddata(:,2); %nanoseconds
tph_time_mass = sort_tph_mass(:,2);
%countspeaks1 = length(peaks);
%countspeaks2 = length(timingdat);

%%
figure(1)
%Energy Plot
subplot(1,2,2)
hist(peaks(:),1000)
xlabel('Energy (keV)')
ylabel('Counts')
xlim([50000,130000])
grid()

subplot(1,2,1)
edges = [0:.25:16000];
hist(tph_time_mass(:),edges)
xlabel('\Deltat (ns)')
ylabel('Counts')
xlim([200,900])
grid()
%%
figure(2)
scatter(peaks(:),tph_time_energy(:),5)
ylabel('\Deltat (\mus)')
xlabel('Energy (keV)')
grid ()
xlim([50000,120000])
ylim([200,900])
%%
% Contour time vs. energy plot
figure(3)
a = [peaks(:),tph_time_energy(:)];
hist3(a,[150 150])
set(get(gca,
'child'),'FaceColor','interp','CDataMode','auto','LineStyle','none');vi
ew([0 90]);
ylabel('\Deltat (\mus)')
xlabel('Energy (keV)')
xlim([50000,120000])
ylim([200,900])
%%
L = 11.8; % distance in cm
Volt = input('Enter Cathod Voltage'); % Enter CATHODE voltage in
command window
Pressure = input('Enter Operating Pressure'); % Enter operating voltage
in command window
E = Volt/L; % electric field
E_P = E/Pressure;
mu_0_e = 10E4; %[cm^2/Vs]  from publication
mu_0_i = 1; %[cm^2/Vs]
v_dr = ((-.5203*(E_P)^2)+(3.3228*E_P)-.1261)*10^6 %drift velocity of
electrons [cm/s*torr]
D = tph_time_energy*(10^-9); %(sorteddata(:,1)-sorteddata(:,3))/100;
%[s]
R =  L-(D.*v_dr);  % range of ff [cm]
R_t = [R,tph_time_energy(:,1)];
```

```
%%
hist(R,1000)
xlim([5,11])
ylabel('Counts')
xlabel('Range (cm)')
%% TPH plots
%Mass and TPH
edges_mass = {(60:1:180),(0:25:1000)};
figure(12)
scatter(sort_tph_mass(:,4),tph_time_mass(:),5)
ylabel('\Deltat (\mus)')
xlabel('Mass (amu)')
grid ()
xlim([60,180])
ylim([200,900])

figure(13)
a = [sort_tph_mass(:,4),tph_time_mass(:)];
hist3(a,'Edges',edges_mass)
set(get(gca,
'child'),'FaceColor','interp','CDataMode','auto','LineStyle','none');vi
ew([0 90]);
ylabel('\Deltat (\mus)')
xlabel('Mass (amu)')
xlim([60,180])
ylim([200,900])
%%
%TPH and Energy
figure(14)
edges_energy = {(50000:1000:120000),(0:25:1000)};
scatter(sorteddata(:,4),tph_time_energy(:),5)
ylabel('\Deltat (\mus)')
xlabel('Energy (keV)')
grid ()
xlim([50000,120000])
ylim([200,900])

figure(15)
a = [sorteddata(:,4),tph_time_energy(:)];
hist3(a,'Edges',edges_energy)
set(get(gca,
'child'),'FaceColor','interp','CDataMode','auto','LineStyle','none');vi
ew([0 90]);
ylabel('\Deltat (\mus)')
xlabel('Energy (keV)')
xlim([50000,120000])
ylim([200,900])
%%
%Mass and Range
figure(16)
edges_range = {(60:1:180),(0:.1:11)};
scatter(sort_tph_mass(:,4),R,5)
ylabel('Range (cm)')
xlabel('Mass (amu)')
grid ()
xlim([60,200])
ylim([7.5,10.5])
```

```
figure(17)
a = [sort_tph_mass(:,4),R];
hist3(a,'Edges',edges_range)
set(get(gca,
'child'),'FaceColor','interp','CDataMode','auto','LineStyle','none');vi
ew([0 90]);
ylabel('Range (cm)')
xlabel('Mass (amu)')
xlim([60,180])
ylim([7.5, 10.5])
%% Z determination
Energy_IC = [sorteddata(:,4)]; % Energy in Joulse
Mass = [sort_tph_mass(:,4)];% mass in kg
Range = [R]; % Range in m
%Beta = 1*exp(-4);
Beta = .03534
Sqr_root_EM = (Energy_IC.*Mass).^(1/2);
Z = ((Beta.*Sqr_root_EM)./Range).^(3/2);

edges_z = [0:.1:100];
hist(Z,edges_z)
%xlim([10,25])
%%
figure(20)
subplot(2,2,1)
scatter(Z,Energy_IC,5)
ylabel('Energy (keV)')
xlabel('Z')
xlim([10,25])
ylim([50000,120000])
subplot(2,2,2)
scatter(Z,Mass,5)
ylabel('Mass (amu)')
xlabel('Z')
xlim([10,25])
ylim([60,200])
subplot(2,2,3)
scatter(Z,Range,5)
ylabel('Range (cm)')
xlabel('Z')
xlim([10,25])
ylim([7.5,10.5])



%%
tic
B = [];
b = [R_t(:,2)];
f = [mass_un(:,2)];
l = [KEadd_t(:,2)];
k2=0
for i2 = (1:length(l));
    k2=k2+1;
    for g = (n:length(f))
        if (abs(f(g)-b(i2))<300)
            B(i2,:)=[R_t(i2,1),R_t(i2,2),mass_un(g,1),mass_un(g,2)];
```

```
            break
        end
    end
    if (k2 == 100)
        k2 = 0;
        (i2/length(f))*100
    end
end
fprintf('Complete\n')
toc

loc = find(B(:,1)==0);
B(loc,:) = [];
%%
tic
F = [];
k4 = 0
for i3 = (1:length(l));
    k4 = k4+1;
    for q = (n:length(f))
        if (abs(f(q)-l(i3))<300)

F(i3,:)=[KEadd_t(i3,1),KEadd_t(i3,2),mass_c_t(q,1),mass_c_t(q,2)];
            break
        end
    end
    if (k4 == 100)
        k4=0;
        (i3/length(f))*100
    end
end
fprintf('Complete\n')
toc
loc2 = find(F(:,1)==0);
F(loc2,:) = [];
%%
F_tmp = F;
B_tmp = B;
[N1,M1] = size(B_tmp);
[S1,T1] = size(F_tmp);

if (N1>S1)
    F1 = F;
    F1 = [B1;zeros(N1-S1,T1)];
    B1 = B_tmp;
else
    B1 = B;
    B1 = [B1;zeros(S1-N1,T1)];
    F1 = F_tmp;
end
%%
E_mass_range = [F1,B1(:,1),B1(:,2)];
%%
fignum = 25;
figure(fignum)
fignum = fignum+1;
subplot(2,2,1)
scatter(E_mass_range(:,3),E_mass_range(:,1),1) % energy vs. mass
```

```
xlim([0,200])
xlabel('Mass (amu)')
ylabel('KE (keV)')
grid()
subplot(2,2,2)
scatter(E_mass_range(:,1),E_mass_range(:,5),1) % energy vs. range
%xlim([50000,130000])
ylim([7,9.5])
xlabel('KE (keV)')
ylabel('Range (cm)')
grid()
subplot(2,2,3)
scatter(E_mass_range(:,3),E_mass_range(:,5),1) % mass vs. range
ylim([7,9.5])
%xlim([0,200])
xlabel('Mass (amu)')
ylabel('Range (cm)')
grid()
%subplot(2,2,4)
%scatter(timingdat(:),E_mass_range(:,3),1)
%%
tic

%B = [];
%b = [R_t(:,2)];
%f = [mass_c_t(:,2)];
%l = [KEadd_t(:,2)];
%k2=0
%for i2 = (1:length(l));
    %k2=k2+1;
    %for g = (n:length(f))
        %if (abs(f(g)-b(i2))<300)
            %B(i2,:)=[R_t(i2,1),R_t(i2,2),mass_c_t(g,1),mass_c_t(g,2)];
            %break
        %end
    %end
    %if (k2 == 100)
        %k2 = 0;
        %(i2/length(f))*100
    %end
%end
%fprintf('Complete\n')
%toc

%loc = find(B(:,1)==0);
%B(loc,:) = [];
%%
Z_ucd = (98/252).*B1(:,3);
Zmean = mean(Z_ucd)
Zdata = Z_ucd-Zmean
scatter(B1(:,3),Zdata)
```

Appendix C

Electrical Breakdown

A major issue that was observed over the course of this experiment was electrical breakdown. Breakdown was an issue not previously encountered but arose due to the implementation of isobutane. As stated previously, isobutane allows for much higher reduced electric field within the chamber. To obtain these E/P conditions, 4500 volts needed to be applied to the cathode and approximately 4200 volts on the first guard ring. However, at these voltages and gas pressures breakdown was repeatedly observed. It was assumed breakdown occured at the high voltage feedthroughs, due to the closeness of the high voltage leads and grounded parts. Figure 58 is a schematic of the feedthroughs used for this project.

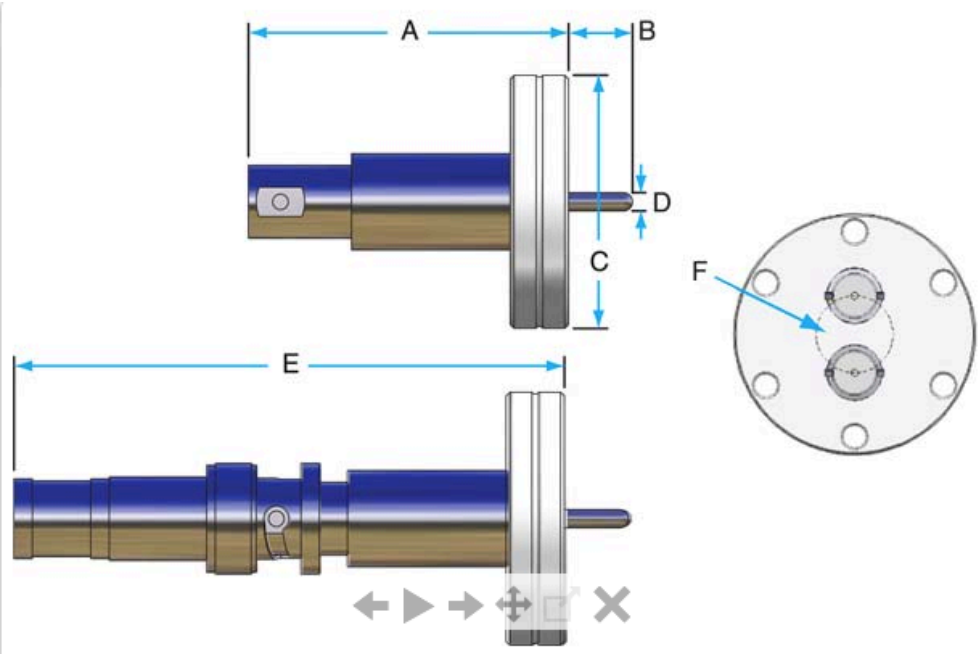

Figure 58 – High voltage feedthrough [Lesker 2016]

The issue was believed to reside on the pin side of the connector, where the distance from the pin to the metal surrounding it was about 2 mm. This proved to be a short enough distance for the voltage to arc causing breakdown within the system. This finding is consistent with Paschen's Law that states that the breakdown of a specific gap distance is a function of the gas pressure and gap length, as presented in Figure 59 for air. Note that air is more insulating than P-10 and isobutane, so breakdown issues occur at larger distances than would be extracted from this plot.

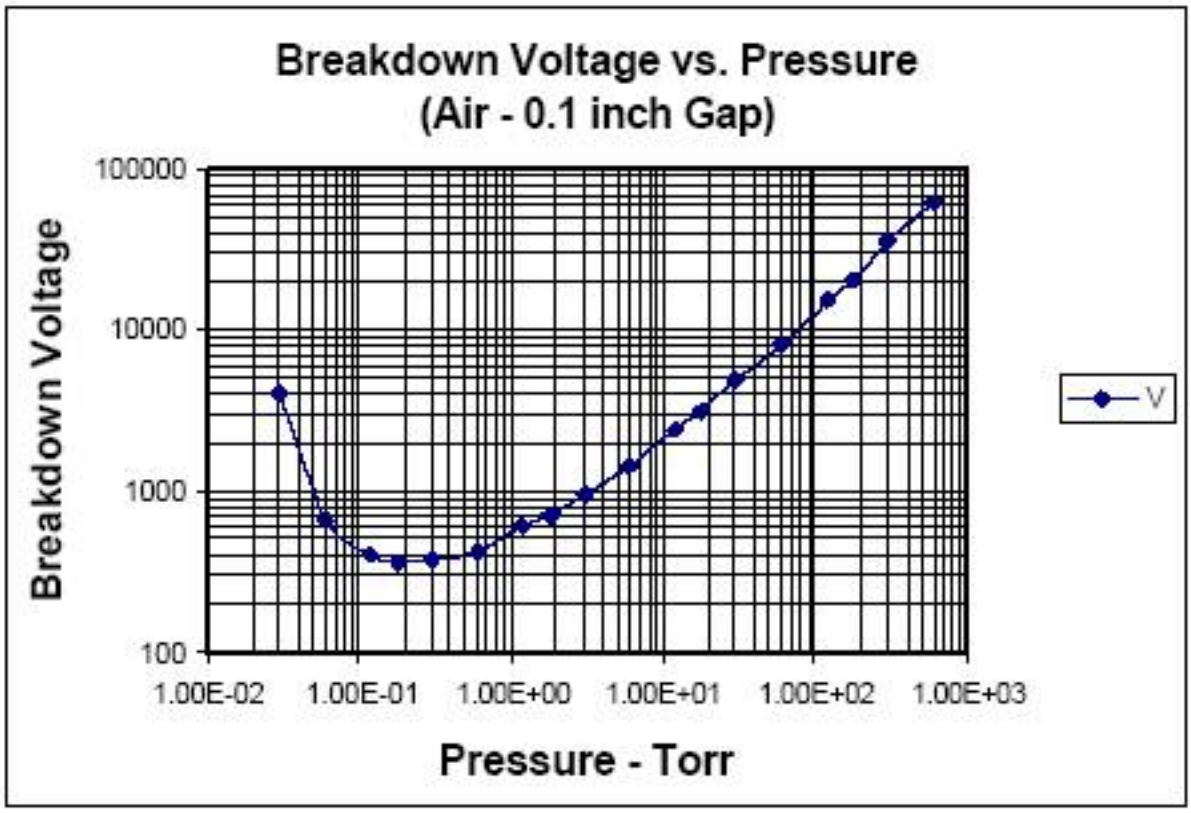

Figure 59 – Breakdown voltage vs. pressure [High Voltage Connection 2016]

Figure 59 shows that for a 0.1 inch (2.54 mm) gap, the approximate gap width from the pin to flange, and a pressure of 50 Torr the breakdown voltage is approximately 1000 V. This

issue is of major concern for our ionization chamber, especially with a more conducting gas than air. To ensure that the feedthroughs were the source of the problem, the entire ionization chamber was emptied and voltage was only applied to the feedthrough with no other connections inside. Breakdown was observed on all three feedthroughs at pressure and voltages consistent with this graph.

As an attempt to alleviate this issue, new custom-made flanges were designed using different SHV feedthrough connections. Figure 60 shows the SHV connections that were be attached to the flanges. The main difference of this connector is the large amount of insulation around the pin. Given its location on the low-pressure side of the detector, this should provide enough distance and insulating material to avoid breakdown.

Figure 60 – SHV feedthrough connection [Pasternack 2016]

After changing to these feedthroughs, breakdown was still observed, which led to an investigation of other parameters that could be contributing to this issue. It was found that the amount of Teflon, used to isolate the cathode and IC entrance window assembly from the grounded vacuum flange it rests on, was not thick enough. To fix this issue new isolation pieces, one made of Delrin and one of Teflon, were constructed with an additional 0.5 cm thickness to provide enough separation between the HV connections and the chamber walls. Teflon has excellent insulating properties but is very soft and has mechanical issues. Delrin is better mechanically, it is able to hold screw threads, but has slightly lower electrical resistivity.

The new isolation setup was first tested with the Delrin piece and led to more desirable conditions but breakdown still occurred at higher voltages. This issue was mitigated by the installation of the thicker Teflon piece.

References

Aprile, E.; Bolotnikov, A. E.; *et al*., 2006. *Noble Gas Detectors.* 1st ed. Weinheim: Wiley-VCH Verlag GmbH & Co.

Boucheneb, N.; Geltenbort, P.; *et al*., 1989. High Resolution Measurements of Mass, Energy, and Nuclear Charge Correlations for $^{229}Th(n_{th},f)$ with the Cosi Fan Tutte Spectrometer. *Nuclear Physics A,* Volume 502, pp. 261-270.

Buchriegler, J.; 2013. *Construction of a Multi-Anode Ionization Chamber for AMS at VERA*, M.Sc. Thesis, University of Vienna, Austria.

Döbeli, M.; Kottler, C.; *et al*., 2004. Gas ionization chambers with silicon nitride windows for the detection and identification of low energy ions. *Nuclear Instruments and Methods in Physics Research B*, Volume 219-220, pp. 415-419.

England, T. R.; Rider, B. F., 1994. Evaluation and Compilation of Fission Product Yields. LA-UR-94-3106, ENDF-349. Los Alamos National Laboratory, Los Alamos, New Mexico, USA.

Fulbright, H. W., 1979. Ionization Chambers. *Nuclear Instruments and Methods,* Volume 162, pp. 21-28.

Heffern, L., 2015. Personal connection

High Voltage Connection, 2016 [Online]. Available at: http://www.highvoltageconnection.com/articles/paschen-curve.html

Lesker, Kurt J, 2016 [Online]. Available at: http://www.lesker.com/

James, A. N.; Butler, P. A.; *et al*., 1982. The Response of an Isobutane Filled Ion Chamber to Heavy Ions. *Nuclear Instruments and Methods,* Volume 212, pp. 545-553.

Khryachkov, V. A.; Dunaeva, I. V.; *et al*., 2003. A Method for Rapid Measurements of Working-Gas Properties in a Pulse Ionization Chamber. *Instruments and Experimental Techniques,* Volume 46, No 6, pp. 804-813.

Knoll, G. F., 2010. *Radiation Detection and Measurement.* 4th ed. New Jersey: John Wiley & Sons.

Madland, D. G., 2006. Total prompt energy release in the neutron-induced fission of ^{235}U, ^{238}U, and ^{239}Pu. *Nuclear Physics A,* Volume 772, pp. 113-137.

Magee, 2001. [Online]. Available at: http://lablemminglounge.blogspot.com/2011/03/why-fuel-rods-are-radioactive.html.

National Nuclear Data Center, Brookhaven Nation Laboratory, 2012 [Online]. Available at: http://www.nndc.bnl.gov/

Oed, A.; Geltenbort, P.; *et al*., 1983. A Mass Spectrometer for Fission Fragments Based on Time-of-Fight and energy Measurements. *Nuclear Instruments and Methods in Physics Research,* Volume 219, pp. 569-574.

Pasternack, 2016 [Online]. Available at: https://www.pasternack.com.

Peisert, A.; Sauli, F., 1984. *CERN 84-08:* Drift and Diffusion of Electrons in Gases: A Compilation, Geneva: CERN.

Rochman, D., Faust, H.; *et al*., 2002. Isotopic yields from the reaction $^{245}Cm(n_{th},f)$ at the Lohengrin mass separator. *Nuclear Physics A*, Volume 710, pp. 3-28.

Sanami, T.; Hagiwara, M.; *et al*., 2006. *KEK Preprint2006-28*: Enhancement on energy dynamic range of Bragg curve counter with active cathode, Japan: High Energy Accelerator Research Organization.

Sanami, T.; Hagiwara, M.; *et al*., 2009. A Bragg curve counter with an internal production target for the measurement of the double-differential cross-section of fragment production induced by neutrons at energies of tens of MeV. *Nuclear Instruments and Methods in Physics Research A,* Volume 610, pp. 660-668.

Schmitt, H. W.; Neiler, J. H.; Walter, F. J., 1965. Energy Correlation Measurements for ^{252}Cf Spontaneous Fission and ^{235}U Thermal-Neutron Fission. *Physical Review,* Volume 141, Number 3, Oak Ridge National Laboratory, Oak Ridge, Tennessee.

Tsoulfanidis, N.; Landsberger, S., 2015. *Measurement & Detection of Radiation.* 4th ed. Florida: CRC Press.

Turner, J., 2007. *Atoms, Radiation, and Radiation Protection.* 3rd ed. Weinheim, Tennessee: Wiley-VCH.

Tyukavkin, A. N.; Pyatkov Yu. V.; *et al*., 2008. Measuring the Nuclear Charge of Fission Fragments Using a Large Ionization Chamber – Part of the Double-Arm Time-of-Flight Spectrometer. *Instruments and Experimental Techniques,* Volume 52, Number 4, pp. 508-518.

Vega, J.J, Reynoso, R., 2005. Application of neural networks to pulse-shape analysis of Bragg curves. *Nuclear Instruments and Methods in Physics Research B,* Volume 243, pp. 232-240.

Wagemans, C., 1991. *The Nuclear Fission Process.* 1st ed. Florida: CRC Press.

Ziegler, J.F., 2008. *Particle Interactions with Matter*. [Online]. Available at: www.SRIM.org.